ADAPTIVE SIDELOBE CANCELLATION FOR MUTUAL RADAR INTERFERENCE

A Thesis
Presented to
The Academic Faculty

By

Timothy Yang

In Partial Fulfillment
of the Requirements for the Degree
Master of Science in the
College of Engineering
School of Electrical and Computer Engineering

Georgia Institute of Technology

Aug 2021

ADAPTIVE SIDELOBE CANCELLATION FOR MUTUAL RADAR INTERFERENCE

Thesis committee:

Dr. Christopher Barnes
Electrical and Computer Engineering
Georgia Institute of Technology

Dr. Aaron Lanterman
Electrical and Computer Engineering
Georgia Institute of Technology

Dr. David Anderson
Electrical and Computer Engineering
Georgia Institute of Technology

Date approved: July 23, 2021

For my wife Kathryn

ACKNOWLEDGMENTS

I would like to thank the members of my thesis committee for their help in preparation of this work – Prof. Christopher Barnes, who helped to shed new light on many of my ideas and challenged me to explore new views, Prof. David Anderson, and Prof. Aaron Lanterman.

Special thanks are due to my advisors and colleagues at Raytheon Technologies. This work would not have been possible without the support and advisement of Rich Holden and Dan Marshall whose patience and knowledge have been invaluable.

The author gratefully acknowledges the support for this work offered by Raytheon Technologies and the Advanced Study Program.

TABLE OF CONTENTS

LIST OF TABLES

LIST OF FIGURES

LIST OF ACRONYMS

ADC analog-to-digital converter

AOA angle of arrival

C-SLC correlation with sidelobe cancellation

CNN convolutional neural network

CNR clutter-to-noise ratio

CPI coherent processing interval

DBF digital beamforming

DFT discrete Fourier transform

DOF degrees-of-freedom

FFT fast Fourier transform

FLOP floating point operations

FOV field of view

GSC generalized sidelobe cancellation

IC-SLC iterative correlation with sidelobe cancellation

IM-SLC iterative machine learning with sidelobe cancellation

INR interference-to-noise ratio

JNR jammer-to-noise ratio

KKT Karush-Kuhn-Tucker

LFM linear frequency modulation

M-SLC machine learning with sidelobe cancellation

MTI moving target indication

PRF pulse repetition frequency

PRI pulse repetition interval

RCS radar cross-section

RDM range-Doppler map

SINR signal to interference and noise ratio

SIR signal-to-interference ratio

SLC auxiliary sidelobe cancellation

SMI sample matrix inversion

SNR signal-to-noise ratio

TFI time-frequency image

ULA uniform linear array

SUMMARY

Radar-to-radar interference is an issue arising due to the increasing number of radar systems being deployed in close proximity. Co-located radars systems, operating using pulse-burst linear frequency modulation (LFM) waveforms, appear as temporally non-stationary interference to the victim radar. As a result, this interference can degrade the victim radar's ability to detect and track targets. Countermeasures can be applied, and phased array architectures allow for spatially adaptive methods to suppress interference. Auxiliary sidelobe cancellation (SLC) is an algorithm commonly employed by subarray phased array architectures to adaptively suppress interference by inducing a spatial notch in the direction of interference. This technique requires an accurate estimate of the interference covariance statistics across array sensors, which becomes more challenging when the interference results from non-stationary time sources such as co-located radar systems.

This thesis proposes several novel algorithms to improve the robustness of estimating the interference statistics. One proposed algorithm, C-SLC, applies existing concepts which measure the correlation between array sensors to identify interference samples. A second proposed algorithm, M-SLC, applies existing concepts which classify 1-D waveform signals through use of a time-frequency image (TFI) and a convolutional neural network (CNN) to identify interference samples. Additionally, this thesis proposes iterative algorithms, IC-SLC and IM-SLC, incorporating C-SLC and M-SLC to suppress interference in an environment containing multiple stationary and non-stationary time sources. Simulated results are provided which demonstrate the effectiveness of these proposed methods.

CHAPTER 1

INTRODUCTION

1.1 Background

Radar systems detect and track targets of interest by transmission and reception of electromagnetic signals [1]. Further signal processing is performed after reception to determine a target's range, velocity, and angle. In many situations, the target is in an environment containing electromagnetic interference from slow-moving clutter, hostile jamming, and activity from co-located radar systems [2]. These interference sources can mask the presence of the target making it more difficult to detect, and an example environment is shown in Figure 1.1.

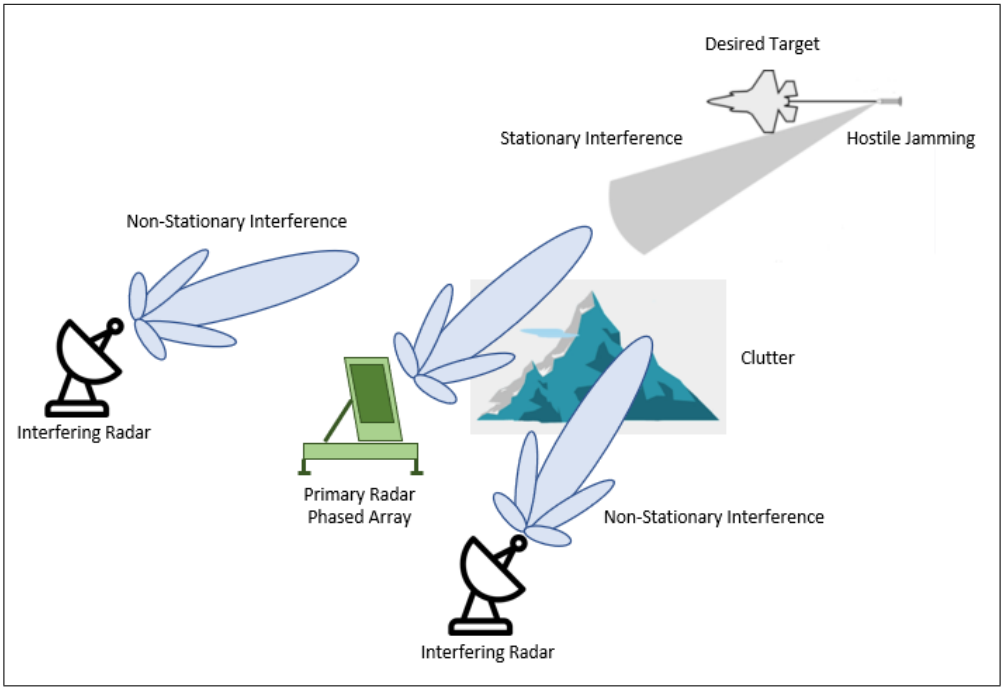

Figure 1.1: Primary radar is shown detecting and tracking a target in the presence of clutter and interference.

Many modern radars utilize a phased array which allows for electronic steering and spa-

tial adaptation [3]. Throughout this thesis, the primary radar, consisting of a phased array architecture, is defined as the victim radar seeking to detect and track a target in the presence of interference. Several algorithms exist to adaptively suppress interference, and SLC is an example of such an algorithm initially proposed in [4]. SLC is commonly employed by subarray architectures which uses an estimate of the interference covariance between array channels to spatially suppress the interference. Obtaining an accurate estimate of the interference statistics can be trivial for interference resulting from stationary time sources such as white noise jammers. However, this becomes more challenging when the interference results from non-stationary time sources such as co-located radar systems operating using pulsed frequency modulated waveforms. Therefore, for effective interference suppression within Figure 1.1, SLC must be robust to both stationary and non-stationary time interference.

1.2 Purpose

The purpose of this thesis is to investigate and propose adaptive algorithms for phased array radars to spatially suppress interference in an environment containing both stationary and non-stationary time sources. This is achieved by proposing novel algorithms which apply the concepts introduced in [5] involving sensor correlation and [6] involving waveform classification by CNNs. These proposed algorithms seek to improve the estimation of the interference covariance matrices implemented within constrained SLC.

The primary radar evaluated in this thesis is a phased array subarray architecture. The primary radar operates on a single coherent processing interval (CPI) at a time, and the signal processing steps required to generate a clutter-free range-Doppler map (RDM) are reviewed. This includes digital beamforming (DBF), moving target indication (MTI) filtering, Doppler processing, and pulse compression. The effects of white noise jamming and co-located radar interference are investigated, and literature review of interference suppression algorithms, including constrained SLC, is provided.

Throughout this thesis, SLC is the primary suppression algorithm evaluated, and methods are proposed to adaptively identify samples to estimate the interference covariance matrices. One proposed algorithm, defined as C-SLC, applies the concepts introduced in [5] to use auxiliary sensor correlation to identify interference samples. This thesis contributes analysis of the expected correlation between sensors for various signal to interference and noise ratio (SINR) scenarios to guide the selection of a correlation threshold. With additional assumptions of the mutual radar interference, this thesis also proposes a novel algorithm, defined as M-SLC, which applies the concepts introduced in [6] to perform waveform classification through use of TFIs and CNNs. Both algorithms seek to improve the robustness of estimating the interference covariance matrices.

Additional challenges are introduced when both stationary and non-stationary time interference sources are present. Stationary interference can mask the presence of non-stationary interference, and this thesis proposes novel iterative methods, defined as IC-SLC and IM-SLC, which incorporate C-SLC and M-SLC. Performance of these algorithms is evaluated and compared in a simulated environment.

1.3 Structure of Thesis

Chapter 2 provides the model of the primary phased array radar and the signal model of all components within the primary radar's environment. The constraints of the primary radar's operation are also provided which mostly pertain to the application of large scale phased array radars. This includes the application of subarray architectures to reduce monetary and computation costs and CPI block processing. Basic signal processing techniques such as MTI filtering to suppress clutter, Doppler processing to extract velocity resolution, and pulse compression to extract range resolution are reviewed. These techniques are used throughout this thesis to generate clutter-free RDMs that define a target's position, range, and velocity.

Chapter 3 provides an introduction and derivation of common interference suppression

algorithms such as sample matrix inversion (SMI) and SLC. The benefits of using SLC for subarray architectures is detailed and is the primary suppression algorithm evaluated throughout this thesis. Using the primary radar model, the algorithmic procedure to suppress stationary interference is provided along with simulated examples. The problem of target suppression with SLC is introduced, and this chapter details the application of a linear constraint to the least square SLC formulation as a solution to improve robustness of SLC by preventing target suppression [7].

Chapter 4 details the effects of non-stationary interference, such as co-located radar interference, on the performance of the primary radar by evaluating resulting RDMs. Specifically, the structure of interference within the RDM is analyzed. Additionally, this chapter details the challenges introduced by non-stationary interference for suppression when using SLC and other algorithms reviewed in literature.

Chapter 5 proposes the C-SLC algorithm which applies sensor correlation to adaptively identify interference samples for estimation and SLC suppression. Simulated examples and comparison to previously defined methods are provided for suppression of a single non-stationary interference source. Implementation of the C-SLC algorithm is first given in the time domain and then extended into the range and Doppler domain.

Chapter 6 proposes the M-SLC algorithm which applies spectrograms and CNNs as an application to adaptively identify interference samples for estimation and SLC suppression. The assumptions of the co-located radar interference required to implement this method are detailed, and simulated examples and comparison to previously defined methods are provided for suppression of a single non-stationary interference source.

Chapter 7 introduces the challenges of performance interference suppression in an environment containing both stationary and non-stationary interference. Iterative algorithms, IC-SLC and IM-SLC, are proposed which involve the use of the correlation and machine learning methods detailed in Chapter 5 and Chapter 6. Simulated examples and comparison to previously defined methods are provided for suppression of multiple stationary and non-

stationary sources. Additionally, consideration is provided to the benefits of a radar system which allows for incremental updates to the estimated interference covariance matrix.

Chapter 8 provides a conclusion along with future opportunities for research.

CHAPTER 2
RADAR AND SIGNAL MODEL

This chapter reviews the fundamentals of phased array architectures and details the trade-offs between fully adaptive and subarray architectures. The signal model and parameters for the primary radar waveform, target reflections, clutter reflections, and interference are also discussed. Additionally, review of basic signal processing techniques to generate clutter-suppressed RDMs is provided.

2.1 Phased Array Model

Phased array radars consist of an array of antenna elements to transmit or receive electromagnetic signals. This thesis focuses on the application of monostatic radars which use the same array of antenna elements to perform coordinated transmission and reception of electromagnetic signals [3]. Throughout this thesis, a uniform linear array (ULA) is modeled and evaluated, and the element pattern is assumed to be isotropic. Additionally, throughout this thesis, the far-field approximation is assumed so that wavefronts are evaluated as planar. This requires that

$$R > \frac{2D^2}{\lambda}, \tag{2.1}$$

where R is the distance between the antenna aperture and wavefront source, D is the antenna length, and λ is the wavefront wavelength [8]. For a 32-element array operating at $6\,\mathrm{GHz}$ with $\lambda/2 = 0.025\,\mathrm{m}$ element spacing and $D = 0.025(32-1) = 0.775\,\mathrm{m}$ array length, then $2D^2/\lambda = 24\,\mathrm{m}$, which is exceeded for many track and search operations such as the scenario given in Figure 1.1.

2.1.1 Phased Array Steering

Phased arrays allow for electrically steered antenna beams by incorporating a periodic phase shift or time delay across elements related to the steer angle and carrier frequency of the signal [3]. These phase shifts or time delays can be implement digitally or with analog hardware. An example N element ULA with a sinusoidal wavefront arriving at $\theta_0 = 30°$ angle of arrival (AOA) is shown in Figure 2.1.

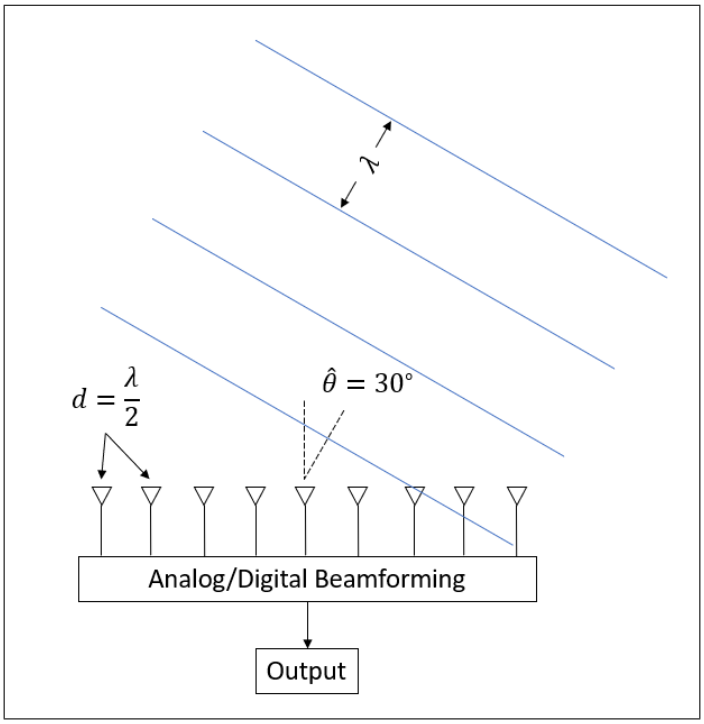

Figure 2.1: Phased array ULA with a wavefront arriving at $\theta_0 = 30°$ is shown. Spacing between elements is $d = \frac{\lambda}{2}$.

The sinusoidal waveform measured by a single coherent receiver without noise is modeled by

$$r(t) = A(t)e^{j[\Omega t + \phi(t)]}, \tag{2.2}$$

where $A(t)$ represents the amplitude modulation, Ω represents the frequency in radians,

and ϕ represents a phase offset. Down-conversion results in the signal model expression,

$$\begin{aligned} r_B(t) &= A(t)e^{j[\Omega t+\phi(t)]}e^{-j\Omega t} \\ &= A(t)e^{j\phi(t)}, \end{aligned} \tag{2.3}$$

where only the desired $\phi(t)$ phase term remains within the exponent. Accounting for noise at the receiver, the signal model is expressed as

$$r_B(t) = A(t)e^{j\phi(t)} + n(t), \tag{2.4}$$

where the noise component, $n(t)$, represents zero-mean Gaussian-distributed thermal noise with variance equal to noise power, $\sigma_n^2 = kTB$, where $k = 1.38 \times 10^{-23}$ J/K is the Boltzmann constant, T is temperature in Kelvin, and B is the receiver bandwidth in hertz [9]. Using this result, the down-converted sinusoidal waveform measured by the n^{th} element of the ULA is modeled by

$$r_B^{(n)}(t) = A(t)e^{j\phi(t)}e^{-jn\gamma_0} + n_n(t), \tag{2.5}$$

where $n_n(t)$ is the independent and uncorrelated noise measured on the n^{th} element and γ_0 is the periodic phase shift applied to each element,

$$\gamma_0 = \frac{2\pi d \sin\theta_0}{\lambda}. \tag{2.6}$$

The down-converted sinusoidal waveform measured by all N elements of the ULA is modeled by the following vector expression,

$$\boldsymbol{r}_B(t) = A(t)e^{j\phi(t)}\boldsymbol{a}(\theta_0) + \boldsymbol{n}(t), \tag{2.7}$$

where the noise is independent and uncorrelated across the sensors and $\boldsymbol{a}(\theta_0)$ is the direc-

tional wavefront vector,

$$\boldsymbol{a}(\theta_0) = \begin{bmatrix} 1 & e^{-j\gamma_0} & \dots & e^{-j\gamma_0(N-1)} \end{bmatrix}^T. \tag{2.8}$$

Beamforming to the direction of the wavefront, θ_0, can be performed by taking the inner product between $\boldsymbol{r}_B(t)$ and a steering vector defined as the conjugate of the directional wavefront vector, $\langle \boldsymbol{r}_B(t), \boldsymbol{a}^\star(\theta_0) \rangle$. This steering vector represents the weights applied to each of the N elements. Therefore, the output of the N element ULA steered towards θ_0 is

$$\begin{aligned} y_\theta(t) &= \langle \boldsymbol{r}_B(t), \boldsymbol{a}^\star(\theta_0) \rangle \\ &= \langle A(t)e^{j\phi(t)}\boldsymbol{a}(\theta_0) + \boldsymbol{n}(t), \boldsymbol{a}^\star(\theta_0) \rangle \\ &= NA(t)e^{j\phi(t)} + \langle \boldsymbol{n}(t), \boldsymbol{a}^\star(\theta_0) \rangle. \end{aligned} \tag{2.9}$$

This specific steering vector, $\boldsymbol{a}^\star(\theta_0)$, is uniform in magnitude weighting, and a taper weighting can be applied to lower sidelobes at the cost of widening the main beam [10]. The normalized antenna pattern evaluated at M discrete angles can be represented by the $1 \times M$ vector $\boldsymbol{p}$. For an N element ULA with element weights, $\boldsymbol{a}^\star(\theta_0)$, $\boldsymbol{p}$ is found by computing

$$\boldsymbol{p} = \frac{1}{N}\boldsymbol{a}^\star(\theta_0)^T\boldsymbol{A}, \tag{2.10}$$

where $\boldsymbol{A}$ is an $N \times M$ matrix containing the directional wavefront vectors for M angles,

$$\boldsymbol{A} = \begin{bmatrix} \boldsymbol{a}(\theta_1) & \dots & \boldsymbol{a}(\theta_M) \end{bmatrix}. \tag{2.11}$$

Additionally, the vector $\boldsymbol{p}$ can be expressed as

$$\boldsymbol{p} = \frac{1}{N}\begin{bmatrix} p(\hat{\theta}, \theta_1) & \dots & p(\hat{\theta}, \theta_M) \end{bmatrix}, \tag{2.12}$$

where $p(\theta_0, \theta_m) = \boldsymbol{a}^\star(\theta_0)^T\boldsymbol{a}(\theta_m)$. Note that this is equivalent to a discrete Fourier trans-

form (DFT) where the frequency term is $\frac{d \sin \theta_0}{\lambda}$. An example antenna pattern for a 32-element ULA steered to $\theta_0 = 30°$ is shown in Figure 2.2.

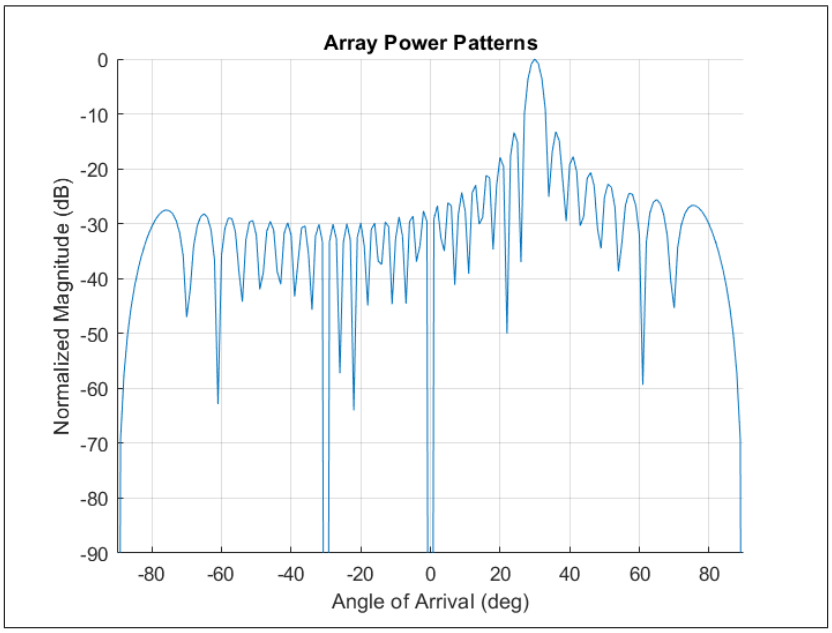

Figure 2.2: Example antenna pattern of a 32-element ULA with $d = \frac{\lambda}{2}$ and $\theta_0 = 30°$.

As observed in Figure 2.2, the first sidelobes are approximately 13 dB below the peak of the main beam.

2.1.2 Array Gain

Phased arrays result in signal-to-noise ratio (SNR) gain versus a single element. Given the received signal model of a single element expressed by Equation 2.4, the single element SNR is determined as $SNR_e = \frac{A^2}{\sigma_n^2}$ [11].

$$\begin{aligned} SNR_e &= \frac{\mathbf{E}\{|A(t)e^{j\phi(t)}|^2\}}{E\{|n(t)|^2\}} \\ &= \frac{A^2}{\sigma_n^2} \end{aligned} \tag{2.13}$$

When the noise across sensors is independent and uncorrelated, $\mathbf{E}\{n_i(t)n_j(t)\} = 0$ when $i \neq j$, the SNR of the received signal, expressed by Equation 2.9, of an N element ULA

steered to the direction of the wavefront is

$$\begin{aligned} SNR_a &= \frac{\mathbf{E}\{|NA(t)e^{j\phi(t)}|\}}{\mathbf{E}\{|\langle \boldsymbol{n}(t), \boldsymbol{a}^{\star}(\theta_0)\rangle|^2\}} \\ &= \frac{N^2A^2}{\mathbf{E}\{|\sum_{i=1}^{N} n_i(t)a_i^{\star}(\theta_0)|^2\}} \\ &= \frac{N^2A^2}{\mathbf{E}\{\sum_{i=1}^{N}\sum_{j=1}^{N} n_i(t)n_j(t)a_i^{\star}(\theta_0)a_j(\theta_0)\}} \\ &= \frac{N^2A^2}{\mathbf{E}\{\sum_{i=n}^{N} (n_i(t))^2\}} \\ &= \frac{N^2A^2}{N\sigma_n^2} \\ &= \frac{NA^2}{\sigma_n^2}. \end{aligned} \tag{2.14}$$

Therefore, the SNR gain for an N element ULA with uniform magnitude weighting is N.

$$\begin{aligned} G_{Array} &= \frac{SNR_a}{SNR_e} \\ &= \frac{NA^2\sigma_n^2}{A^2\sigma_n^2} \\ &= N \end{aligned} \tag{2.15}$$

2.1.3 Spatial Aliasing

To perform beamforming, a phased array effectively samples a wavefront in space. If the wavefront is approaching from the edge of the array's field of view (FOV), or endfire, as shown in Figure 2.3, then Nyquist's theorem requires that the array elements must be spaced less than $\lambda/2$ to prevent spatial aliasing [12]. This is analogous to sampling a sinusoidal signal in time.

As the element spacing increases beyond $\lambda/2$, spatial aliasing occurs which result in grating lobes at specific angles within the antenna pattern [10]. The location of grating lobes within the antenna pattern are determined as a function of the steer angle and element spacing. Recall that the periodic phase shift γ_0 given in Equation 2.6 is applied to each

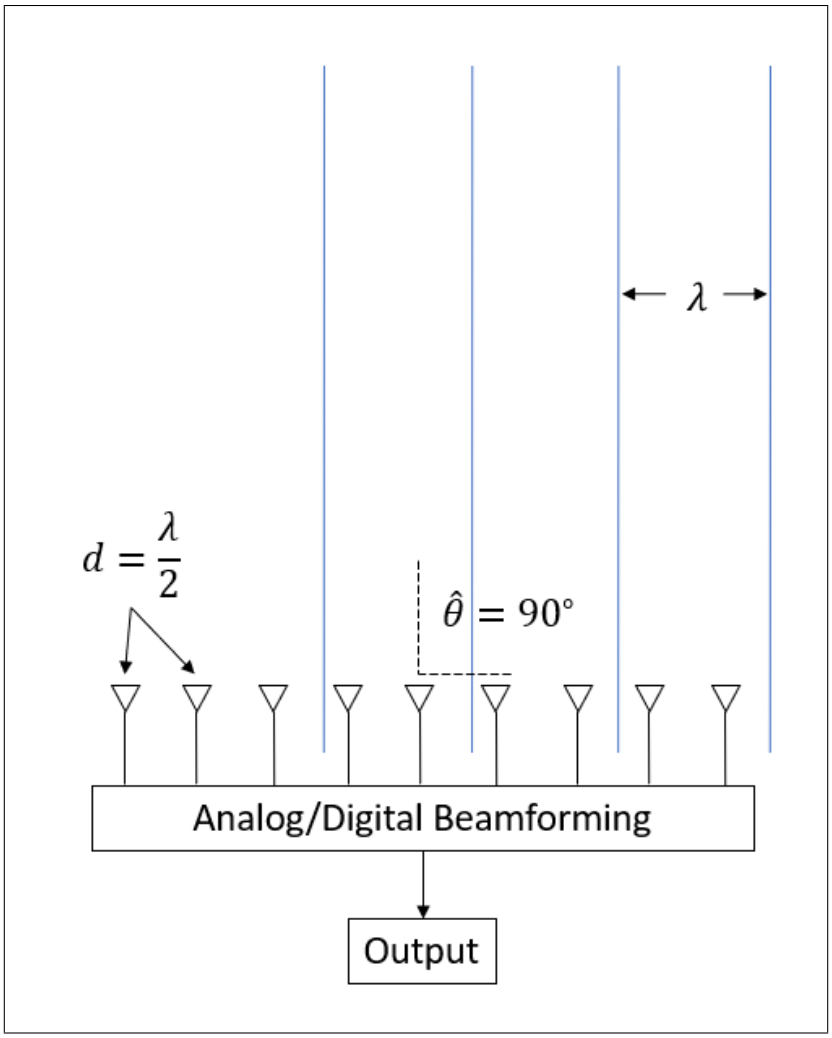

Figure 2.3: A wavefront is approaching the ULA from endfire direction, $\theta_0 = 90°$. Phased array elements spatially sample the incoming wavefront analogous to time sampling a sinusoidal signal.

element to steer the array towards a certain θ_0. When applying this phase shift to each element within the ULA, the array is beamformed to all directions for which the following expression is real,

$$\begin{aligned} \theta &= \arcsin\left(\frac{\lambda}{d}\left[\frac{2\pi m + \gamma_0}{2\pi}\right]\right) \\ &= \arcsin\left(\frac{m\lambda}{d} + \sin\theta_0\right), \quad m = 0, \pm 1, \pm 2, \ldots \end{aligned} \tag{2.16}$$

The expression given in Equation 2.16 is only real when the magnitude of the $\arcsin$ argu-

ment is no greater than 1. Therefore, if $d \leq \frac{\lambda}{2}$, then there is only one real solution which occurs when $m = 0$ given any $\theta_0 \in [-90°, 90°]$. If $d \geq \frac{\lambda}{2}$, then for certain θ_0, grating lobes appear at specific directions in the antenna pattern as given by,

$$\theta_{GL}(d, \theta_0) = \{\theta : |\frac{m\lambda}{d} + \sin\theta_0| > 1\}, \quad m = \pm 1, \pm 2, \ldots \tag{2.17}$$

An example of an antenna pattern with grating lobes is shown in Figure 2.4. In this example, $d = \lambda$ and the array is steered to $\hat{\theta} = 40°$ which results in a grating lobe at $\theta_{GL} = -21°$. The consequence of this effect is that sources located at either $\theta_0 = 40°$ or $\theta_0 = -21°$ are spatially indistinguishable.

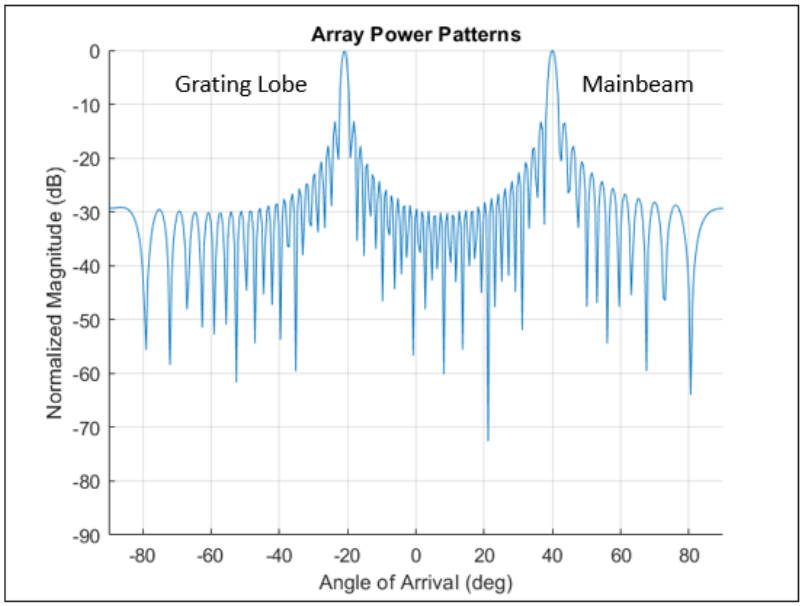

Figure 2.4: Example pattern of a 32-element ULA steered to $\hat{\theta} = 40°$ with $d = \lambda$ resulting in a grating lobe at $\theta_{GL} = -21°$.

2.1.4 Subarray Architectures

A phased array with many elements comes with the advantage of increased SNR as shown in subsection 2.1.2. Additionally, the size of the array is inversely proportional to the beamwidth of the array, so a larger array also comes with the advantage of improved angular resolution [8]. However, digitally adapting a large array with many elements requires

having an analog-to-digital converter (ADC) at each element. This becomes computationally and monetarily costly for phased arrays that contain many elements. Therefore in practice, large phased arrays are often split into subarrays to provide a trade-off between cost and performance [10]. Throughout this thesis, the primary radar performance is limited to that of a subarray architecture.

A subarray phased array architecture groups elements into a smaller number of subarrays with an ADC only at each subarray. Subarrays can either be overlapping or non-overlapping [13], and an example non-overlapped architecture is shown in Figure 2.5.

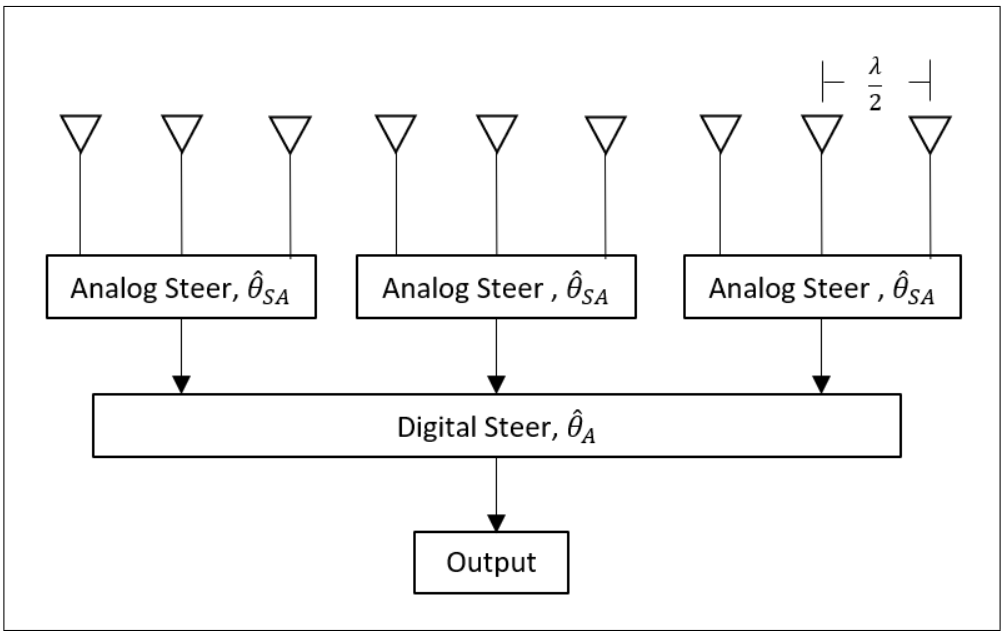

Figure 2.5: Example architecture of phased array with subarrays is shown.

This still requires that the elements within each subarray are analog steered to a fixed direction $\hat{\theta}_{SA}$, but digital steering can occur at the subarray level to a specific direction $\hat{\theta}_A$. As a result, two performance effects are discussed - subarray pattern filtering and grating notches.

The digitally steered pattern across subarrays, $p_A(\hat{\theta}_A, \theta)$, is spatially filtered by the analog subarray pattern, $p_{SA}(\hat{\theta}_{SA}, \theta)$. Therefore, the effective pattern, $p_{eff}(\theta)$, is constrained

to the subarray pattern [11],

$$p_{eff}(\theta) = p_A(\hat{\theta}_A, \theta) p_{SA}(\hat{\theta}_{SA}, \theta). \tag{2.18}$$

An example of this is shown in Figure 2.6.

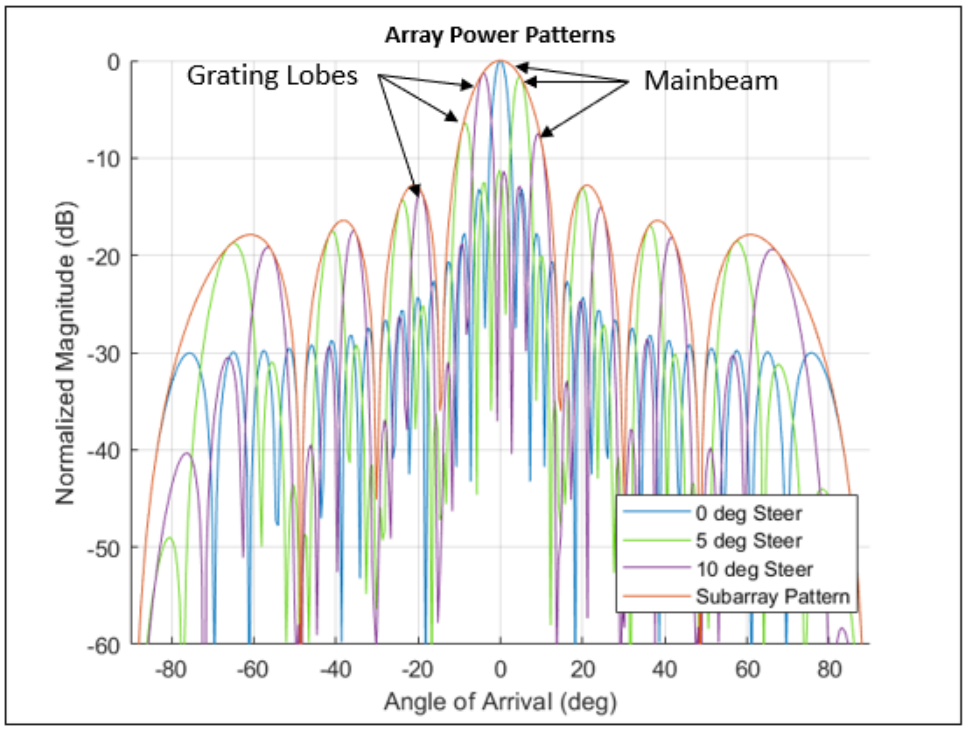

Figure 2.6: The subarray pattern spatially filters the array pattern so that the effective pattern cannot be digitally steered outside subarray pattern. In this figure, $\hat{\theta}_{SA} = 0°$ and $\hat{\theta}_A = [0, 5, 10]°$. Additionally, grating lobes occur since the subarray spacing is greater than $\lambda/2$.

As observed in Figure 2.6, the main beam of the effective pattern is constrained by the main beam of the subarray pattern. Additionally, grating lobes appear since the physical spacing between ADCs at each subarray is greater than $\lambda/2$.

A second limitation to subarray architectures for adaptive array processing is grating notches [14]. Typically, the spacing between subarray channels is much greater than $\lambda/2$ since many element are contained within each subarray. As a consequence, the Nyquist theorem is violated for spatial sampling. The result is that the effective pattern contains

grating lobes as observed in Figure 2.6. When the array is digitally steered to the same direction as each individual subarrays, $\hat{\theta}_A = \hat{\theta}_{SA}$, then the grating lobes are suppressed by the subarray pattern filtering. However, the effect of spatial aliasing still exists, and interference located in a grating lobe is spatially indistinguishable from the target in the main beam. Therefore, if an adaptive algorithm such as SMI is used to suppress interference in a grating lobe, then target suppression also occurs. This is discussed in further detail in Chapter 3 to give the motivation for focusing on the SLC algorithm.

2.2 Signal Model

Within this section, a signal model is developed for each of the components in Figure 1.1. This includes the primary radar waveform, reflections from target and clutter, interference, and noise.

2.2.1 Waveform Model

Throughout this thesis, the primary radar transmits and receives a LFM pulse-burst waveform. An LFM waveform is used to increase time-bandwidth product and improve range resolution versus a simple pulse through matched filtering [15]. The model for the down-converted LFM waveform with bandwidth, β, and pulse width, τ, is

$$x(t) = a(t)e^{\frac{j\pi\beta t^2}{\tau}}, \tag{2.19}$$

where $a(t)$ is the amplitude modulation and for simple pulsed modulation,

$$a(t) = \begin{cases} 1 & t \in [0, \tau] \\ 0 & \text{otherwise} \end{cases}. \tag{2.20}$$

An example LFM waveform pulse with $\beta = 5\,\mathrm{MHz}$ and $\tau = 5\,\mu\mathrm{s}$ is shown in Figure 2.7. Throughout this thesis, only narrow-band waveforms are modeled to prevent beam squint

[16].

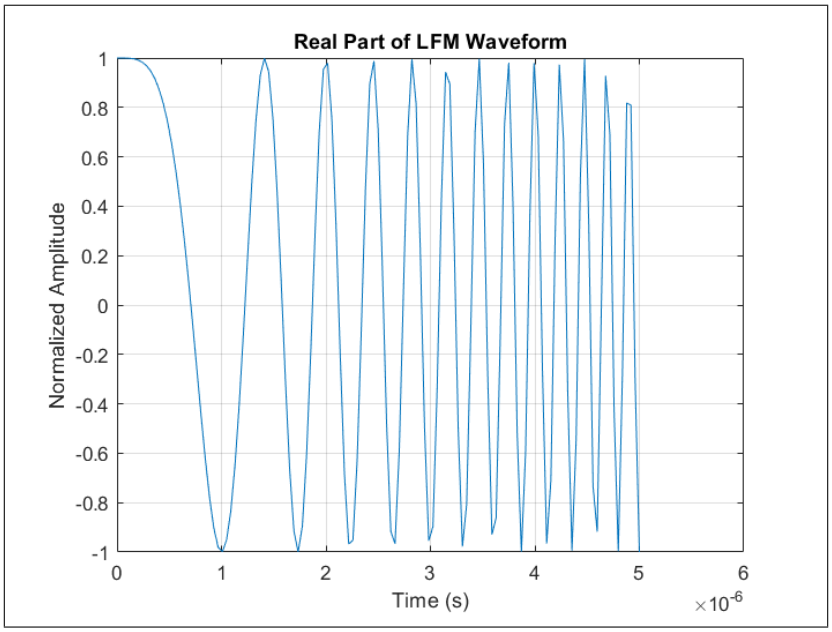

Figure 2.7: The real part of an example LFM pulse with $\beta = 5\,\mathrm{MHz}$ and $\tau = 5\,\mu\mathrm{s}$ is shown.

Using multiple pulses allows for Doppler processing to provide velocity resolution. The model for an LFM pulse-burst waveform with M pulses and pulse repetition interval (PRI) of T is

$$x_{burst}(t) = \sum_{m=0}^{M-1} x(t - mT). \tag{2.21}$$

2.2.2 Complete Receive Model

Noise Model

Noise is modeled as a stationary zero-mean, $\mathbf{E}\{n(t)\} = 0$ Gaussian distributed process with noise power equal to variance, $\mathbf{E}\{n(t)^2\} = \sigma_n^2 = kTB$, as described in subsection 2.1.1. The noise is spatially independent and uncorrelated between elements within a phased array, $\mathbf{E}\{n_i(t), n_j(t)\} = 0$ when $i \neq j$.

Target Return Model

The target is modeled as a discrete scatterer with specific range R_{tgt}, velocity component in the direction of the radar v_{tgt}, and AOA θ_{tgt}. The voltage of the target return at the receiver, A_{tgt}, is modeled relative to the noise voltage for a specific SNR. When SNR is expressed as a ratio of powers, then $A_{tgt} = \sqrt{\sigma_n^2(SNR)}$. The target model at the receivers of an N element ULA after down-conversion is

$$\boldsymbol{t}_B(t) = \left[A_{tgt} e^{\frac{j4\pi v_{tgt}}{\lambda} t} \sum_{m=0}^{M-1} x\left(t - mT - \frac{2R_{tgt}}{c}\right) \right] \boldsymbol{a}(\theta_{tgt}), \tag{2.22}$$

where $c = 3 \times 10^8 \,\mathrm{m/s}$ is the speed of electromagnetic propagation. In practice, the target return power is often well below the noise power due to low radar cross-section (RCS).

2.2.3 Clutter Return Model

Clutter is modeled as discrete scatterers with specific range R_{clt} and zero velocity. Throughout this thesis, clutter is modeled only in the direction of the target, θ_{tgt}. The voltage magnitude of the clutter return at the receiver, $|A_{clt} e^{j\phi_{clt}}| = A_{clt}$, is modeled relative to the noise voltage for a specific clutter-to-noise ratio (CNR) while maintaining that the magnitude is proportional to R^{-3}. Clutter magnitude is modeled proportional to R^{-3} to account for antenna beam spread [2]. The voltage of the clutter return is also modeled as complex and random over time with Gaussian distributed magnitude and uniformly distributed phase. However, clutter return is spatially correlated between elements within a phased array. The clutter model at the receivers of an N element ULA after down-conversion for K discrete clutter scatterers is

$$\boldsymbol{c}_B(t) = \left[\sum_{k=1}^{K} A_{clt}^{(k)} e^{j\phi_{clt}^{(k)}} \sum_{m=0}^{M-1} x\left(t - mT - \frac{2R_{clt}^{(k)}}{c}\right) \right] \boldsymbol{a}(\theta_{tgt}). \tag{2.23}$$

In practice, CNR is often much greater than target SNR due to high clutter RCS.

2.2.4 Interference Model

Interference is either modeled as a white noise jammer or as an interfering LFM pulse-burst waveform with a specific AOA, θ_{ifr}. The power of white noise jammers at the receiver, A_{jmr}^2, is modeled as a stationary zero-mean Gaussian distributed process with variance relative to the noise power for a specific jammer-to-noise ratio (JNR). The jammer model at the receivers of an N element ULA after down-conversion for a single jammer is

$$\boldsymbol{j}_B(t) = A_{jmr}(t)\boldsymbol{a}(\theta_{ifr}). \tag{2.24}$$

Interfering LFM bursts are modeled with a specific pulse count M_{ifr}, pulse width τ_{ifr}, PRI T_{ifr}, bandwidth β_{ifr}, and random time offset t_{ifr}. The interference voltage, A_{ifr}, is modeled relative to the noise voltage for a specific interference-to-noise ratio (INR). The interfering LFM pulse-burst model at the receivers of an N element ULA after down-conversion for a single interfering LFM is

$$\boldsymbol{i}_B(t) = \left(A_{ifr} \sum_{m=0}^{M_{ifr}-1} i_{lfm}(t - mT_{ifr} - t_{ifr}) \right) \boldsymbol{a}(\theta_{ifr}), \tag{2.25}$$

where $i_{lfm}(t) = e^{\frac{j\pi\beta_{ifr}}{\tau_{ifr}}t^2}$. The interference model for all white noise jammers and interfering LFMs at the receivers of an N element ULA is

$$\boldsymbol{i}_B(t) = \sum_{i=1}^{I} i_i(t)\boldsymbol{a}_i(\theta_i). \tag{2.26}$$

In practice, JNR and INR are often much greater than target SNR due to the one-way travel of interference proportional to R^{-2} versus the two way travel of target returns proportional to R^{-4} [2].

Complete Model

Combining the above models into a single expression to represent the output CPI, or receive window, for all receivers of an N element ULA,

$$\boldsymbol{r}(t) = \left[A_{tgt} e^{\frac{4\pi v_{tgt}}{\lambda} t} \sum_{m=0}^{M-1} x\left(t - mT - \frac{2R_{tgt}}{c}\right) + \sum_{k=1}^{K} A_{clt}^{(k)} e^{j\phi_{clt}^{(k)}} \sum_{m=0}^{M-1} x\left(t - mT - \frac{2R_{clt}^{(k)}}{c}\right) \right] \boldsymbol{a}(\theta_{tgt}) + \sum_{i=1}^{I} i_i(t)\boldsymbol{a}_i(\theta_i) + \boldsymbol{n}(t). \tag{2.27}$$

2.3 Radar Processing

This section reviews the basic signal processing steps to generate RDMs from the received data for an N element ULA. An example is provided for a 32-element ULA with $\lambda/2$ spacing seeking a target with 10 dB SNR at the receiver arriving at $\theta_{tgt} = -25°$ with a radial velocity of $v_{tgt} = 180\,\mathrm{m/sec}$ and range of $R_{tgt} = 10\,\mathrm{km}$. A higher SNR target is used to better demonstrate the processing steps. The primary radar transmits and receives an LFM pulse-burst waveform with center frequency $f_c = 6\,\mathrm{GHz}$, $\beta = 5\,\mathrm{MHz}$, $\tau = 5\,\mu\mathrm{s}$, $T = 125\,\mu\mathrm{s}$, and $M = 81$. The time-domain sample rate is set to $f_s = 5\beta$. No clutter or interference is modeled in this example.

2.3.1 Beamforming

The received data for an N element ULA as expressed by Equation 2.27 is beamformed to a specific direction which is typically selected as the hypothesized target direction, $\hat{\theta} = \theta_{tgt}$. Therefore, as described in subsection 2.1.1, the output of the array after beamforming is

$$y_{\hat{\theta}}(t) = \langle \boldsymbol{r}_B(t), \boldsymbol{a}^{\star}(\hat{\theta}) \rangle. \tag{2.28}$$

Using the example radar model parameters, the peak normalized magnitude of the dis-

cretized output CPI, $r_B[t]$, is shown in Figure 2.8 for a single element. The output CPI, or receive window, is defined as the received data obtained from the transmission of a single pulse-burst.

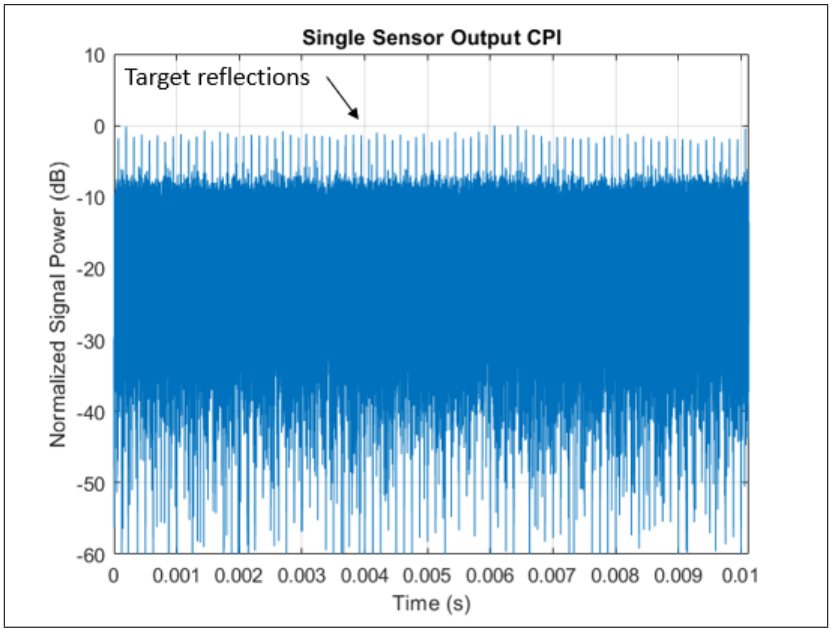

Figure 2.8: The output CPI for a single element is shown. Target reflections of approximately 10 dB SNR are observed.

After beamforming, the magnitude of the output CPI for the entire array, $y_{\hat{\theta}}[t]$, is shown in Figure 2.9. Note that the target SNR after beamforming has increased by a factor of $N = 32$ or approximately 15 dB as expected per subsection 2.1.2.

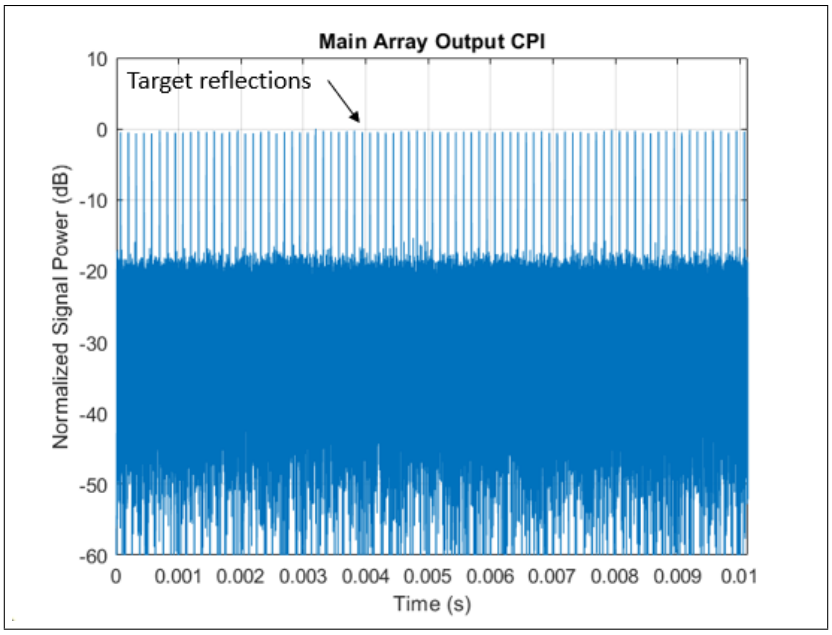

Figure 2.9: The output CPI for the array after beamforming is shown. Target SNR has increased approximately 15 dB from that of Figure 2.8.

2.3.2 Doppler Processing

When $y_{\hat{\theta}}(t)$ is sampled in time with sampling frequency $f_s > 2\beta$ to satisfy Nyquist theorem, then it can also be represented as a vector $\boldsymbol{y}$ of size $f_s TM \times 1$,

$$\boldsymbol{y} = y_{\hat{\theta}} \left(\left[0 : \frac{1}{f_s} : MT \right]^T \right), \tag{2.29}$$

where the colon operator represents a vector with values, $[start : interval : end]$. This vector $\boldsymbol{y}$ is wrapped to form an $f_s T \times M$ matrix $\boldsymbol{Y}$ so that each column represents the received data for a single PRI and each row represents the received data for a single time offset from the beginning of a PRI,

$$\boldsymbol{Y} = \begin{bmatrix} \dots & \boldsymbol{y}_m & \dots \end{bmatrix} \tag{2.30}$$

where

$$\boldsymbol{y}_m = \boldsymbol{y} \left[f_s mT : 1 : f_s (m+1)T - 1 \right]. \tag{2.31}$$

Doppler processing is performed to transform the data from the pulse domain to the Doppler frequency domain [15]. Doppler frequency is a function of velocity, $f_D = \frac{2v}{\lambda}$, so that Doppler processing provides velocity resolution of targets within the primary radar's scene. The resulting velocity resolution is $\frac{\lambda}{2TM}$, so that longer waveforms result in higher resolution. Doppler processing is equivalent to a DFT across the columns of $\boldsymbol{Y}$, where D is the number of Doppler frequencies and the resulting matrix, $\boldsymbol{Y}_{DP}$, is size $f_s T \times D$,

$$\boldsymbol{Y}_{DP} = \begin{bmatrix} \dots & \boldsymbol{y}_{DP}^{(f_D)} & \dots \end{bmatrix} \tag{2.32}$$

where

$$\boldsymbol{y}_{DP}^{(f_D)}[k] = \sum_{m=0}^{M-1} \boldsymbol{y}_m[k] e^{-jm2\pi f_D T}. \tag{2.33}$$

Doppler frequencies are only unambiguous for a single interval of pulse repetition frequency (PRF) [15]. If the DFT is evaluated from $[-PRF/2, +PRF/2]$, then any targets traveling with a Doppler frequency outside this interval is aliased back into the interval $[-PRF/2, +PRF/2]$. To provide simplicity in analysis throughout this thesis. the target is modeled with only positive approaching velocities and no negative receding velocities. Therefore, in this thesis, Doppler processing is evaluated only for the interval $[0, +PRF]$. No scatterers are modeled with a velocity that results in a Doppler frequency outside the interval $[0, +PRF]$.

Similar to the gain achieved after beamforming described in subsection 2.1.2, the target SNR increases by a factor of M after Doppler processing [15].

Continuing the example from Figure 2.9 which shows the magnitude of $\boldsymbol{y}$, the magnitude and real part of the reshaped data matrix $\boldsymbol{Y}$ is shown in Figure 2.10. The time scale is changed to a range scale by $R = \frac{ct}{2}$. Note that the eclipsed range corresponds to the time that the primary radar is transmitting a pulse, so no signal reception occurs during that time.

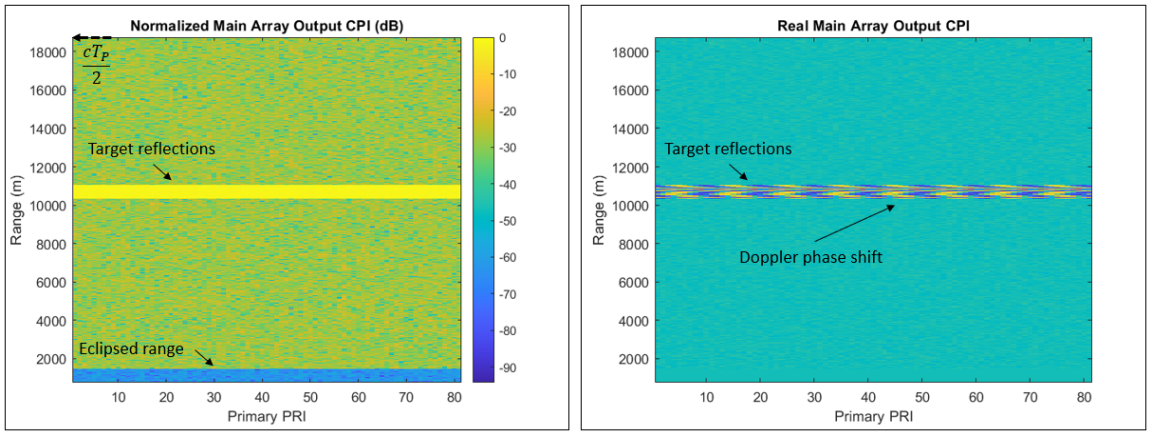

Figure 2.10: The magnitude (left) and real part (right) of the reshaped output CPI is shown.

The target velocity is limited so that there is no range cell migration over the duration of the CPI. The velocity of the target induces a periodic phase shift across the output CPI as observed in Figure 2.10. After Doppler processing, the resulting matrix $\boldsymbol{Y}_{DP}$ is shown in Figure 2.11. Note that the target SNR after Doppler processing has increased by a factor of $M = 81$ or approximately 19 dB, and the target velocity is now clearly $180\,\mathrm{m/sec}$.

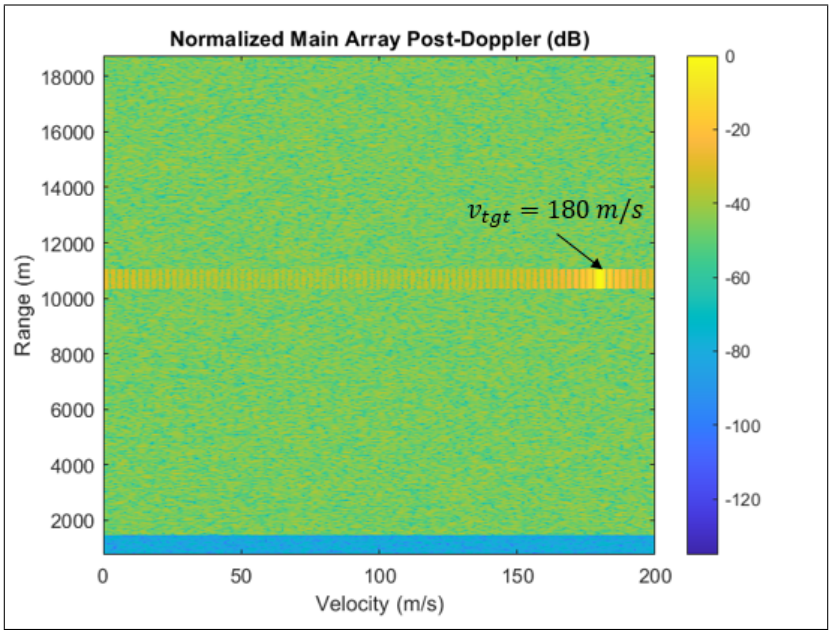

Figure 2.11: The resulting matrix after Doppler processing is shown. Target SNR has increased approximately 19 dB from that of Figure 2.10.

2.3.3 Pulse Compression

Pulse compression is a form of matched filtering between the output CPI of the primary radar and the replica of the primary radar waveform to achieve higher range resolution [15]. Range resolution achieved for an LFM waveform with bandwidth β is $\Delta R = \frac{c}{2\beta}$. Throughout this thesis, pulse compression is performed after Doppler processing for each column of $\boldsymbol{Y}_{DP}$. The resulting matrix, $\boldsymbol{Y}_{PC}$, is size $f_s T \times D$. Performing pulse compression is equivalent to the convolution between the time reversed receive window and the conjugate of the replica. The discretized waveform sampled at a rate of f_s is represented by the vector $\boldsymbol{x}$ with size $N_\tau \times 1$. Therefore, $\boldsymbol{Y}_{PC}$ is equivalent to

$$\boldsymbol{Y}_{PC} = \begin{bmatrix} \dots & \boldsymbol{y}_{PC}^{(f_D)} & \dots \end{bmatrix} \tag{2.34}$$

where

$$\boldsymbol{y}_{PC}^{(f_D)}[k] = \sum_{n=0}^{N_\tau - 1} \boldsymbol{x}^\star[n] \boldsymbol{y}_{DP}^{(f_D)}[k+n]. \tag{2.35}$$

Similar to the gain achieved after beamforming and Doppler processing, the target SNR increases by a factor of N_τ after pulse compression [15].

Continuing the example from Figure 2.11 which shows the magnitude of $\boldsymbol{Y}_{DP}$, the magnitude of $\boldsymbol{Y}_{PC}$ resulting from pulse compression is shown in Figure 2.12. The eclipsed range is not shown, and note that the target SNR after Doppler processing has increased by a factor of $N_\tau = 125$ or approximately 21 dB, and the target range is now clearly $10\,\mathrm{km}$.

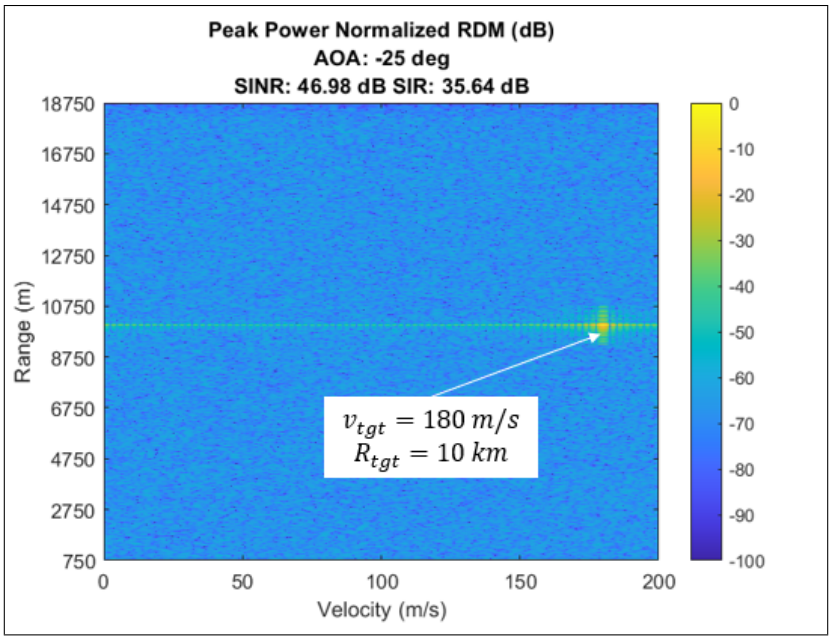

Figure 2.12: The resulting matrix after pulse compression is shown. Target SNR has increased approximately 21 dB from that of Figure 2.10.

2.3.4 Range-Doppler Map

The resulting matrix $\boldsymbol{Y}_{PC}$ shown in Figure 2.12 is defined as the RDM. Each pixel within the RDM represents the received power after signal processing for a specific range, velocity, and AOA. In this case, the target is clearly distinguishable. As a metric to evaluate performance, the the RDM SINR and signal-to-interference ratio (SIR) are computed. SINR is computed as the ratio between the target power and the power average in the remainder of the RDM, and SIR is computed as the ratio between the target power and the peak power outside the target signal and its sidelobes. In Figure 2.12, the SINR is $46.98\,\mathrm{dB}$ and the SIR is $35.64\,\mathrm{dB}$.

2.3.5 MTI Processing

The same target environment and radar model as the example provided in this section is simulated except that clutter is also included. The resulting RDM is shown in Figure 2.13. As observed, clutter is the primary component within the RDM making it difficult to iden-

tify the target. In the case shown in Figure 2.13, the SINR is $9.48\,\mathrm{dB}$.

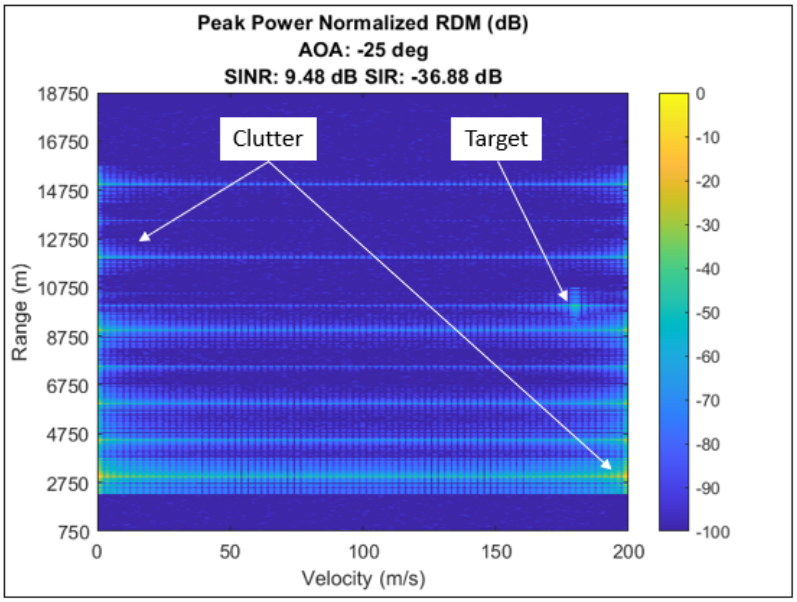

Figure 2.13: Example RDM with clutter is shown.

A simple method to suppress clutter is MTI filtering [15]. MTI filtering is performed by subtracting the received data for each PRI from the received data in the preceding PRI,

$$\boldsymbol{y}_{MTI}^{(m)} = \boldsymbol{y}_m - \boldsymbol{y}_{m+1}. \tag{2.36}$$

Any components within the receive window that are unvarying from pulse to pulse, such as zero velocity clutter, are filtered out. Throughout this thesis, MTI filtering is performed after beamforming but before Doppler processing to perform clutter suppression as shown in Figure 2.14.

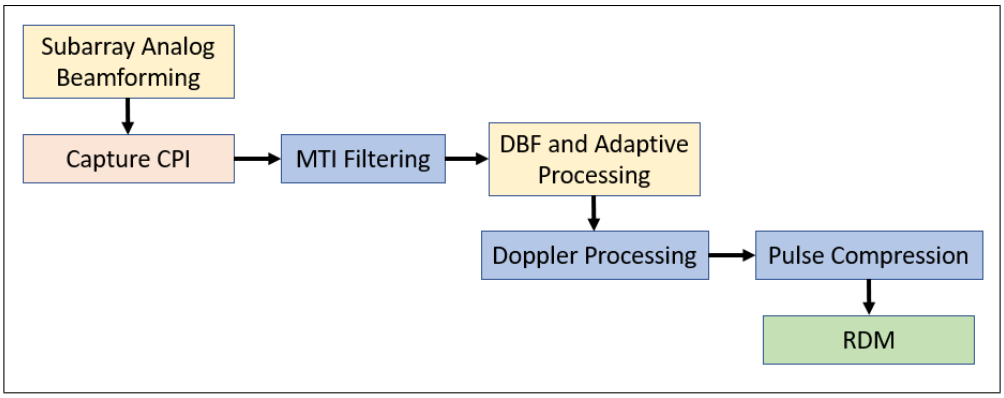

Figure 2.14: The flow of basic radar signal processing used within this thesis is shown.

This allows for clutter suppression to occur in the time domain which comes with the advantage of allowing further adaptive processing in the time domain. Re-processing the output CPI from Figure 2.13 to obtain a new RDM with MTI processing included is shown in Figure 2.15.

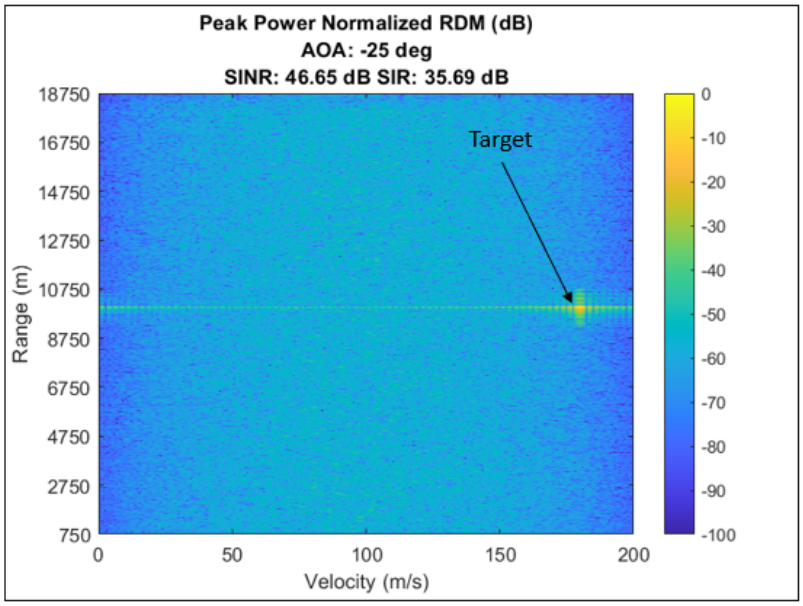

Figure 2.15: Example RDM after MTI processing is shown.

In this RDM, the SINR has been improved to $46.65\,\mathrm{dB}$. A disadvantage of MTI filtering is the resulting transfer function. As observed in Figure 2.15, MTI processing results in a non-uniform transfer function across Doppler frequency equivalent to the following

expression [15],

$$H(f_D) = 2je^{-2\pi f_D/2} \sin\left(\frac{2\pi f}{2}\right). \tag{2.37}$$

This disadvantage can be mitigated by varying the PRF from burst to burst, but this is not discussed in this thesis [17].

CHAPTER 3

ADAPTIVE INTERFERENCE SUPPRESSION

Electromagnetic interference can severely degrade a radar's ability to detect and track targets. Chapter 3 begins by introducing the effects that stationary time interference can cause on resulting RDMs. Stationary time interference sources, such as white noise jammers, can severely degrade a radar's ability to detect and track targets by using amplified noise to mask the presence of targets. However, phased array radars have the capability to spatially adapt and suppress the interference. Adaptive interference suppression algorithms discussed in this chapter include SMI and SLC.

3.1 Interference Effects

A 32-element ULA is modeled to evaluate the effects of stationary interference. The radar and waveform model is identical to the models detailed in section 2.3. The ULA is steered towards a target with -10 dB SNR at the receiver arriving at $\hat{\theta} = \theta_{tgt} = -25^{\circ}$ with a radial velocity of $v_{tgt} = 180\,\mathrm{m/s}$ and range of $R_{tgt} = 10\,\mathrm{km}$. A white noise jammer with 30 dB JNR is located in the first sidelobe of the ULA's antenna pattern. This scenario is shown in Figure 3.1.

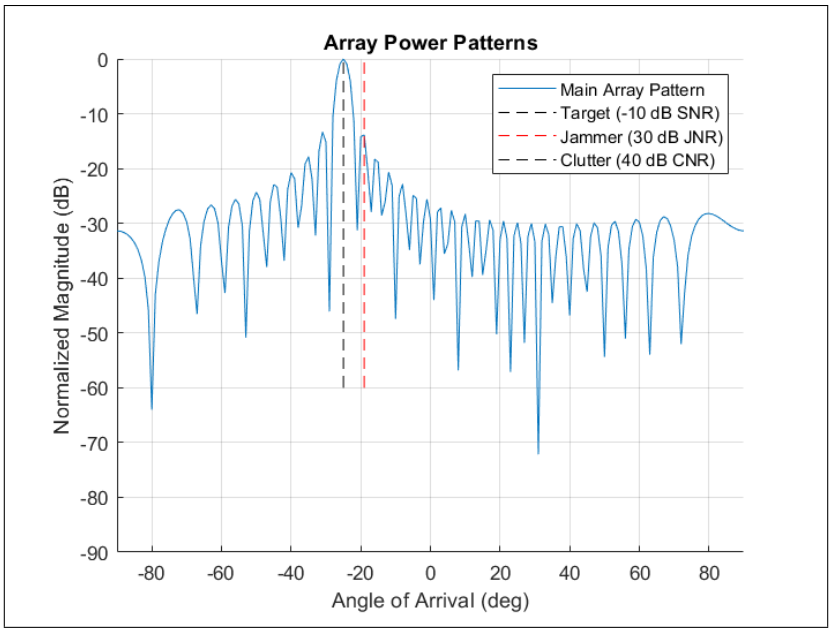

Figure 3.1: ULA is steered to $\hat{\theta} = 25°$. A white noise jammer is located in the first sidelobe of the antenna pattern.

The resulting RDM following the signal processing steps detailed in Figure 2.14 is shown in Figure 3.2. No adaptive suppression algorithm is implemented.

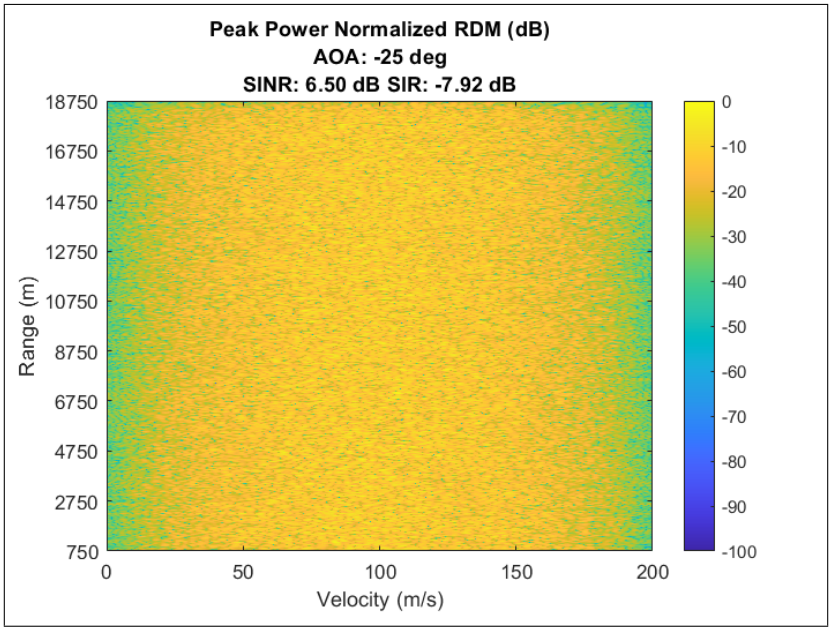

Figure 3.2: Resulting RDM is shown with white noise jammer located in first sidelobe of the antenna pattern. Amplified white noise is the dominant signal in the RDM and the target is not visible.

As observed, the target signal is masked by the white noise jammer resulting in low target SINR. The radar's ability to perform target detection and tracking is severely degraded. However, adaptive processing techniques, such as SMI and SLC, allows adaptive filtering of the interference to recover target SINR.

3.2 Adaptive Algorithms

Phased array systems have the capability to spatially filter interference by adaptively weighting antenna elements. Typically, this requires an estimate of the interference statistics across the array of antenna elements. Two suppression algorithms that use the spatial statistics of interference are discussed in this section - SMI and SLC. Note that the radar architecture addressed throughout this thesis operates by CPI block processing. The primary radar first collects an entire CPI, and then uses the data within this CPI to generate adaptive element weights. These weights are used suppress interference only within that specific CPI, and this process is repeated for each CPI so that each CPI generates new adaptive weights.

3.3 Sample Matrix Inversion

Consider a fully adaptive N-element ULA. If the spatial statistics of the interference across elements are known, then digital element weights can be computed as

$$\boldsymbol{w} = \boldsymbol{R}_I^{-1}\boldsymbol{a}^{\star}(\hat{\theta}), \tag{3.1}$$

where $\boldsymbol{R}_I$ is the $N \times N$ interference covariance matrix between the array antenna elements and $\boldsymbol{a}^{\star}(\hat{\theta})$ is the $N \times 1$ weight vector used to steer the ULA towards $\hat{\theta}$ as described in subsection 2.1.1. This method is known as SMI [18]. The adaptive element weights place a notch at the location of the jammer in the resulting antenna pattern as shown in Figure 3.3.

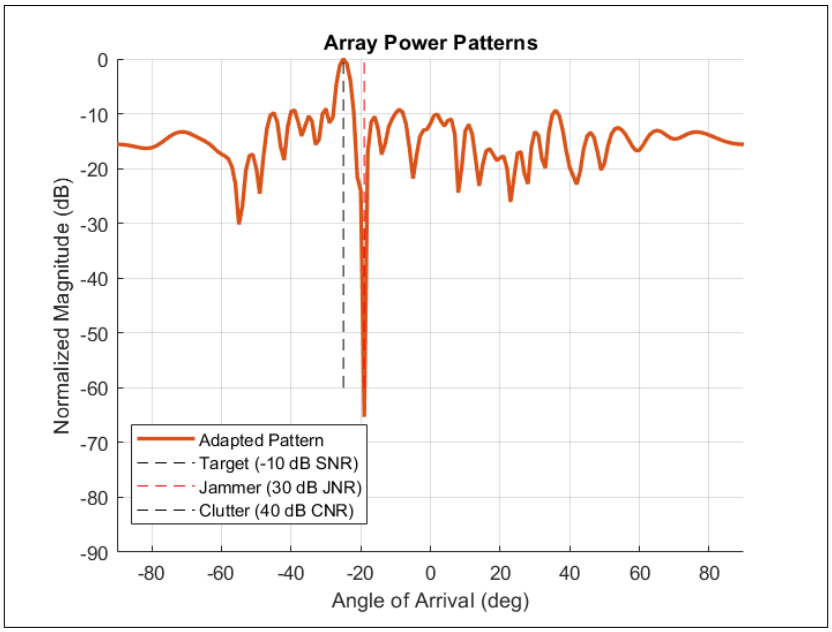

Figure 3.3: Resulting antenna pattern is shown for ULA steered to $\hat{\theta} = -25°$ with adaptive weights derived from SMI. Notch is placed at the location of the jammer.

3.3.1 SMI Derivation

The derivation of SMI follows by maximizing the SIR. Suppose at a single time sample, target reflection and interference is captured across an N-element array represented by the $N \times 1$ vector $\boldsymbol{r}_B = \boldsymbol{t}_B + \boldsymbol{i}_B$. The single sample output after beamforming is therefore $y = \boldsymbol{w}^T \boldsymbol{r}_B$ where $\boldsymbol{w}$ is an N-element vector representing the digital beamforming weights. The power in the output sample is

$$\begin{aligned} |y|^2 &= y^\star y^T \\ &= \boldsymbol{w}^H \boldsymbol{r}_B^\star \boldsymbol{r}_B^T \boldsymbol{w}. \end{aligned} \tag{3.2}$$

The interference covariance matrix is equivalent to

$$\boldsymbol{R}_I = \mathbf{E}\{\boldsymbol{i}_B^\star \boldsymbol{i}_B^T\} \tag{3.3}$$

so that the SIR after beamforming is equivalent to

$$SIR = \frac{\boldsymbol{w}^H \boldsymbol{t}_B^\star \boldsymbol{t}_B^T \boldsymbol{w}}{\boldsymbol{w}^H \boldsymbol{R}_I \boldsymbol{w}} \tag{3.4}$$

Maximizing SIR follows by utilizing Cauchy-Schwarz inequality, which states the following for arbitrary vectors $\boldsymbol{p}$ and $\boldsymbol{q}$,

$$|\boldsymbol{p}^H \boldsymbol{q}|^2 \leq \|\boldsymbol{p}\|_2^2 \|\boldsymbol{q}\|_2^2, \tag{3.5}$$

and equality is achieved only when $\boldsymbol{p}$ is co-linear with $\boldsymbol{q}$, $\boldsymbol{p} = k\boldsymbol{q}$. Taking $\boldsymbol{R}_I = \boldsymbol{A}^H \boldsymbol{A}$ with $\boldsymbol{p} = \boldsymbol{A}\boldsymbol{w}$ and $\boldsymbol{q} = \left(\boldsymbol{A}^H\right)^{-1} \boldsymbol{t}_B^\star$, then Cauchy-Schwarz gives

$$\begin{aligned} |\boldsymbol{w}^H \boldsymbol{A}^H \left(\boldsymbol{A}^H\right)^{-1} \boldsymbol{t}_B^\star|^2 &\leq \|\boldsymbol{A}\boldsymbol{w}\|_2^2 \|\left(\boldsymbol{A}^H\right)^{-1} \boldsymbol{t}_B^\star\|_2^2 \\ \boldsymbol{w}^H \boldsymbol{t}_B^\star \boldsymbol{t}_B^T \boldsymbol{w} &\leq \left(\boldsymbol{w}^H \boldsymbol{R}_I \boldsymbol{w}\right) \left(\boldsymbol{t}_B^T \boldsymbol{R}_I^{-1} \boldsymbol{t}_B^\star\right) \\ SIR &\leq \boldsymbol{t}_B^T \boldsymbol{R}_I \boldsymbol{t}_B^\star \end{aligned} \tag{3.6}$$

with equality only when $\boldsymbol{A}\boldsymbol{w} = k\left(\boldsymbol{A}^H\right)^{-1} \boldsymbol{t}_B^\star$. Therefore, the optimal weight vector is

$$\begin{aligned} \boldsymbol{A}\boldsymbol{w}_{\text{opt}} &= k\left(\boldsymbol{A}^H\right)^{-1} \boldsymbol{t}_B^\star \\ \boldsymbol{w}_{\text{opt}} &= k\boldsymbol{R}_I^{-1} \boldsymbol{t}_B^\star. \end{aligned} \tag{3.7}$$

When $k = 1$, this is equivalent to the expression provided in Equation 3.1.

3.3.2 Covariance Estimate

In practice, the true interference covariance matrix may not be known, so an estimate of the interference covariance matrix, $\hat{\boldsymbol{R}}_I$ is used. The maximum likelihood estimator of the interference covariance matrix which achieves the Cramer-Rao lower bound is [19]

$$\hat{\boldsymbol{R}}_I = \frac{1}{L} \sum_{l=1}^{L} \boldsymbol{R}_I^{(l)}. \tag{3.8}$$

In Equation 3.8, L is the number of samples that the interference is measured across the N-element ULA. As the number of samples L decreases, the estimate of interference degrades and the resulting SINR after adaptive processing decreases [20].

3.3.3 SMI Application

The scenario given in Figure 3.1 is simulated where a target is in an environment containing clutter and a single white noise jammer. The resulting output CPI for a single antenna element after MTI processing is shown in Figure 3.4.

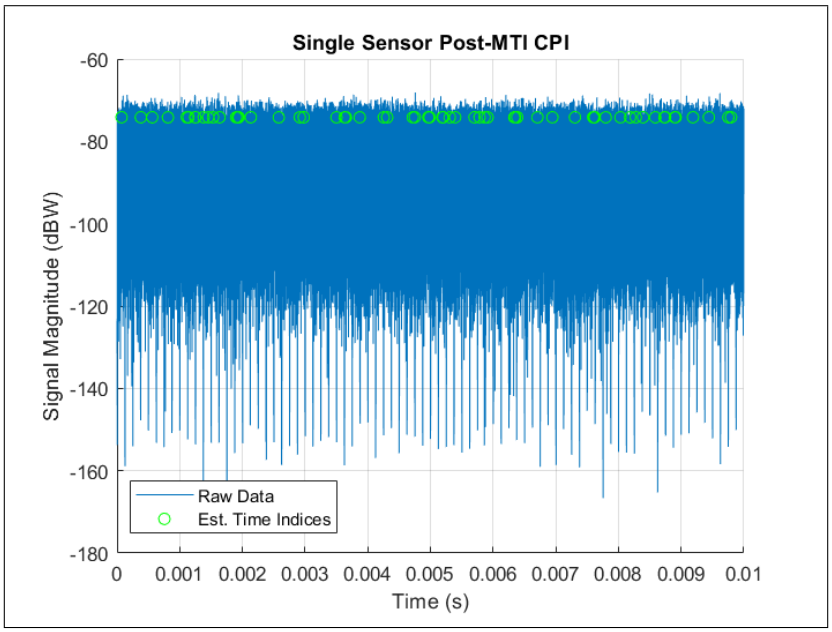

Figure 3.4: Post-MTI output CPI for a single antenna element. White noise jamming is the dominant signal. Green circles represent the random time samples selected to estimate the interference statistics.

Amplified noise from the white noise jammer is the dominant component within the received signal. However, since the white noise jammer is stationary over time, the estimate of the interference covariance matrix can be formed by using a number, such as $L = 60$, random time samples within the CPI,

$$\hat{\boldsymbol{R}}_I = \frac{1}{L}\sum_{l=1}^{L} \boldsymbol{r}_B^{(l)} \left(\boldsymbol{r}_B^{(l)}\right)^H. \tag{3.9}$$

The selection of these random time samples are represented by the green circles in Figure 3.4. The same time indices are used to select samples from the output CPI of all elements. Using the SMI-derived weights given in Equation 3.1, the adaptive element weights are computed as $\hat{\boldsymbol{w}} = \hat{\boldsymbol{R}}_I^{-1}\boldsymbol{a}^{\star}(\hat{\theta})$. The resulting RDM after Doppler processing and pulse compression is shown in Figure 3.5.

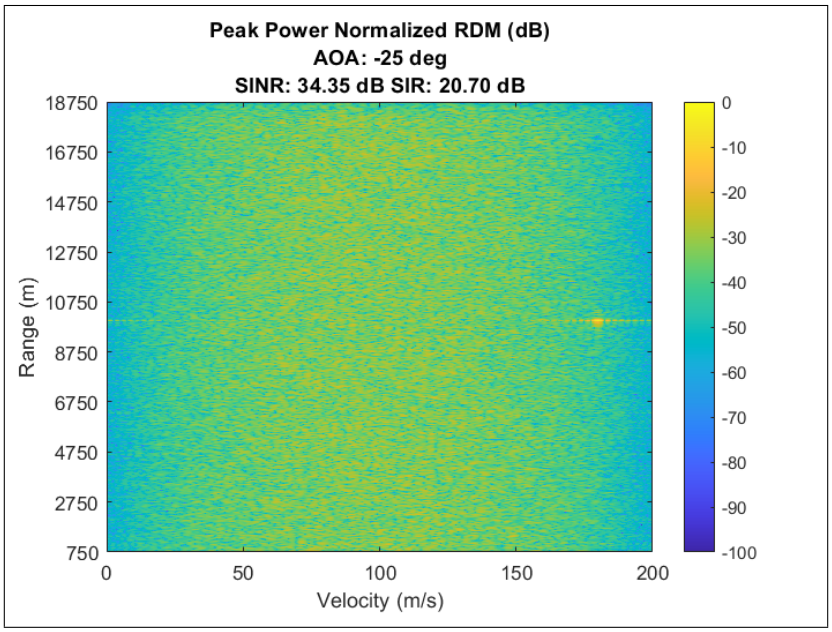

Figure 3.5: Post-SMI RDM for a scenario with a single white noise jammer. The white noise jammer is suppressed, and the target SINR is recovered.

As observed, the effects of the white noise jammer are suppressed and the target is clearly visible. Comparing to the RDM before SMI processing in Figure 3.2, the SINR is significantly improved.

3.3.4 SMI with Subarrays

The previous example of SMI application is for a fully adaptive ULA with $d = \frac{\lambda}{2}$ sensor spacing. When SMI is implemented with a subarray architecture where spacing between digital channels is greater than $\frac{\lambda}{2}$, performance is degraded when the interference is located in a grating lobe. If an interference source is located in a grating lobe as shown in Figure 3.6, then the interference spatially aliases into the main beam as detailed in subsection

2.1.3.

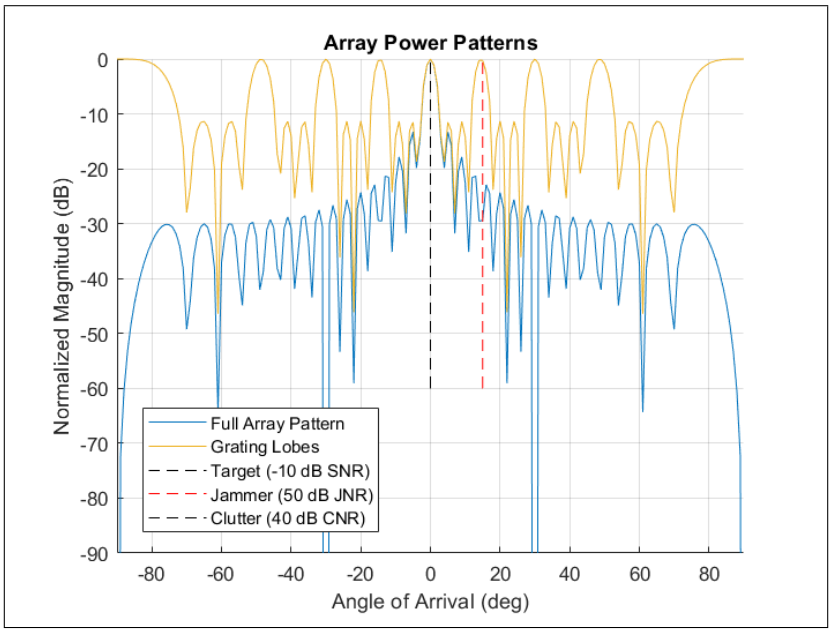

Figure 3.6: Full array antenna pattern (blue) is shown with interference located in a grating lobe. Location of grating lobes is indicated by the yellow trace.

Since the interference is spatially indistinguishable from a target in the main beam, spatial suppression of the interference distorts the main beam and degrades target SNR. This effect is defined as a grating notch [14]. The post-SMI adapted antenna pattern for a subarray architecture with interference located in a grating lobe is shown in Figure 3.7.

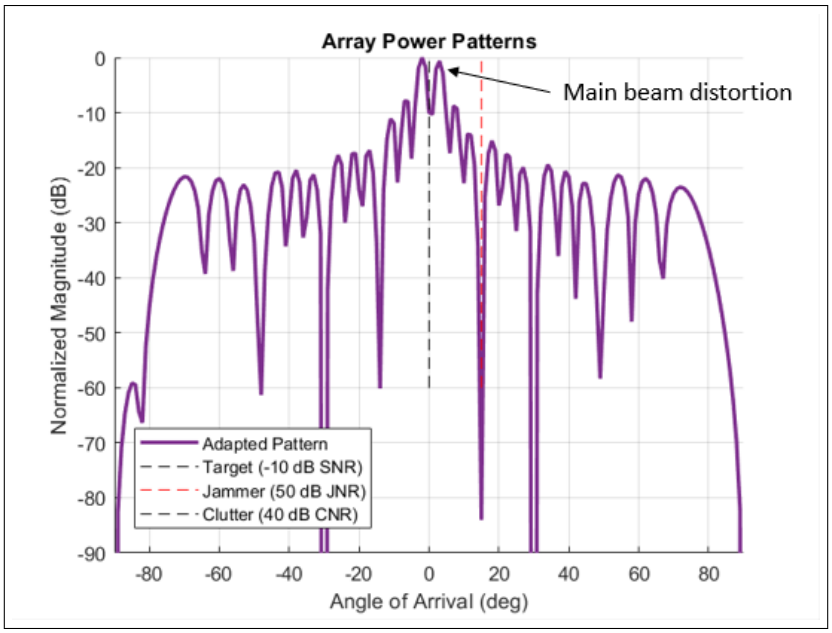

Figure 3.7: Post-SMI antenna pattern with interference located in a grating lobe. Main beam distortion is observed which results in degraded SNR.

As observed, the main beam is distorted which leads to reduced target SNR. A solution to this problem is the SLC algorithm, which is discussed in the next section.

3.4 Sidelobe Cancellation

SLC is a partially adaptive method where the main array is non-adaptive and steered to a fixed direction [4]. A subarray architecture can be treated as a fixed array where each antenna element is analog-steered and the digital subarray weights are fixed so that grating lobes are avoided. Since the main array is fixed, additional adaptive auxiliary antenna elements are required. An example architecture with SLC capability is shown in Figure 3.8

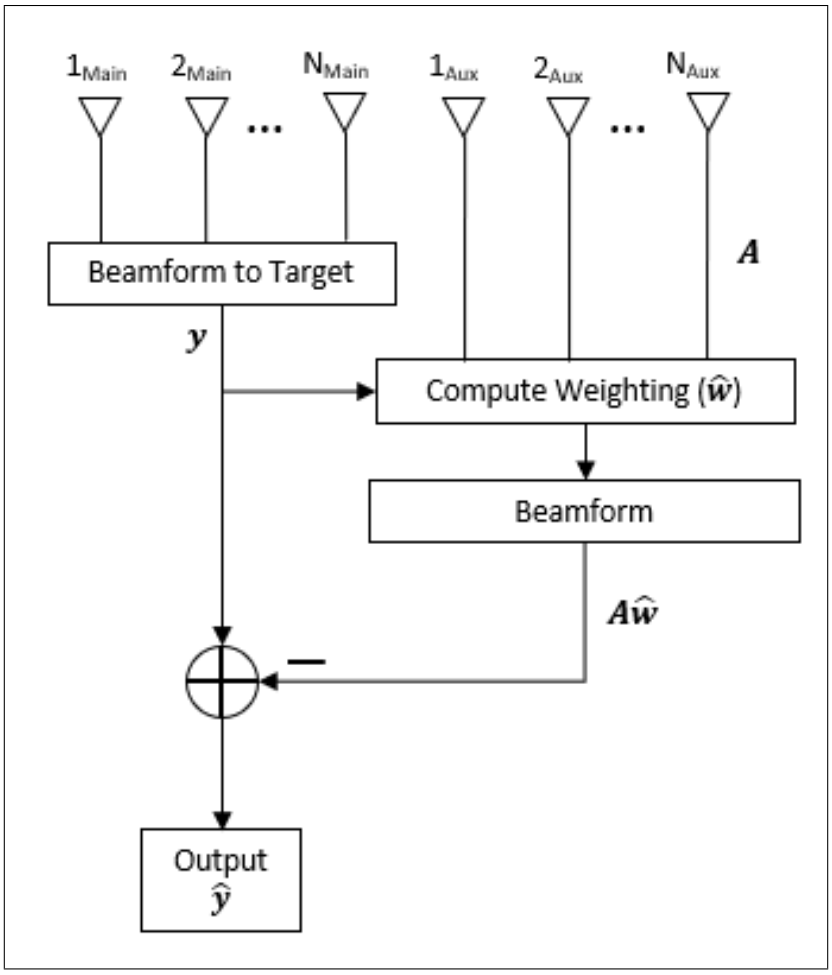

Figure 3.8: Example array architecture with SLC capability.

In Figure 3.8, the main array is steered to a fixed direction with a single channel output for each time sample represented by the vector $\boldsymbol{y}$. For N_S time samples, $\boldsymbol{y}$ has dimensions $N_S \times 1$. The output of each auxiliary antenna element is directly observable and is represented by the matrix $\boldsymbol{A}$ with dimensions $N_S \times N_{Aux}$.

The output of each auxiliary element is digitally adaptive, and interference suppression is achieved by adaptively weighting the auxiliary elements and subtracting its output from the output of the fixed main array. Intuitively, if the auxiliary array is steered to focus on interference, then interference can be minimized by subtracting the output of the auxiliary array from the output of the main array.

3.4.1 SLC Derivation

The derivation of SLC follows from a least squares convex optimization formulation and solution. SLC finds the auxiliary element weights that minimize the square error between the output of the fixed main array and the output of the adaptively weighted auxiliary array [21]. Mathematically, this is represented as

$$\boldsymbol{w}_{opt} = \underset{\boldsymbol{w}}{\operatorname{argmin}} \frac{1}{2}\|\boldsymbol{y} - \boldsymbol{A}\boldsymbol{w}\|_2^2. \tag{3.10}$$

For this least squares formulation, a closed form solution exists and is obtained by taking the gradient with respect to $\boldsymbol{w}$,

$$\begin{aligned} \nabla_{\boldsymbol{w}} \left(\frac{1}{2}\|\boldsymbol{y} - \boldsymbol{A}\boldsymbol{w}\|_2^2 \right) &= \boldsymbol{0} \\ \boldsymbol{A}^H \left(\boldsymbol{y} - \boldsymbol{A}\boldsymbol{w}_{opt}\right) &= \boldsymbol{0} \\ \boldsymbol{w}_{opt} &= \left(\boldsymbol{A}^H \boldsymbol{A}\right)^{-1} \boldsymbol{A}^H \boldsymbol{y}. \end{aligned} \tag{3.11}$$

As observed in Equation 3.11, the adaptive auxiliary weights are a function of the estimated covariance across auxiliary elements, $\hat{\boldsymbol{R}}_{Aux} = \boldsymbol{A}^H \boldsymbol{A}$, and the estimated covariance between auxiliary elements and main array, $\hat{\boldsymbol{R}}_{Ay} = \boldsymbol{A}^H \boldsymbol{y}$. The output of SLC, $\hat{\boldsymbol{y}}$, is the residual difference given by

$$\hat{\boldsymbol{y}} = \boldsymbol{y} - \boldsymbol{A}\boldsymbol{w}_{opt}. \tag{3.12}$$

Note that this formulation assumes the interference power, as sensed by the auxiliary elements, is dominant while the power of target reflections is ideally below the noise floor prior to pulse compression and Doppler processing. These assumptions are often practical since target reflections must travel two-way in range and many interference sources travel one-way in range as depicted in Figure 1.1. Therefore, the power of target reflections is proportional to $\frac{1}{R^4}$ while the power of direct interference is proportional to $\frac{1}{R^2}$ [2].

The number of spatially distinct interference sources that can be suppressed is limited

by the degrees-of-freedom (DOF), which is equivalent to the number distinct eigenvalues of the interference covariance matrix $\boldsymbol{R}_I$ [22]. Therefore with SLC, the theoretical maximum number of interference sources that can be suppressed is N_{Aux}.

3.4.2 SLC Application

A 32-element ULA main array with 6 auxiliary elements is modeled as shown in Figure 3.9.

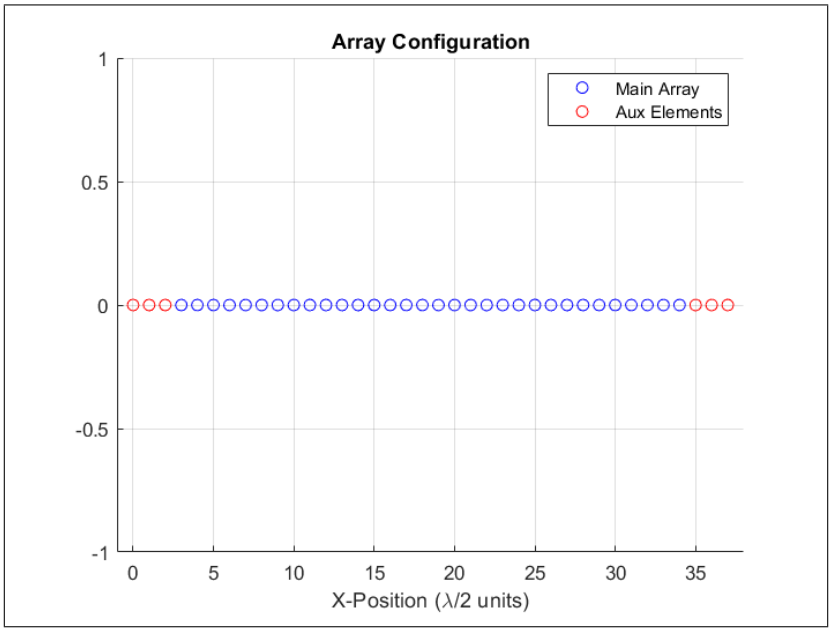

Figure 3.9: Model ULA with SLC capability is shown. The main array elements are non-adaptive and steered to a fixed direction. The auxiliary antenna elements are adaptive and located on each side of the main array.

The auxiliary antenna elements are split on each side of the main array. This lengthens the effective aperture of the auxiliary array resulting in higher resolution to improve suppression of interference close to the target. The waveform model is identical to that described in section 2.3. The scenario shown in Figure 3.1 is repeated so that a white noise jammer is located in the first sidelobe of the main array's antenna pattern. The main array is steered towards the target, and the post-MTI output CPIs of the main array and each of the auxiliary elements are shown in Figure 3.10.

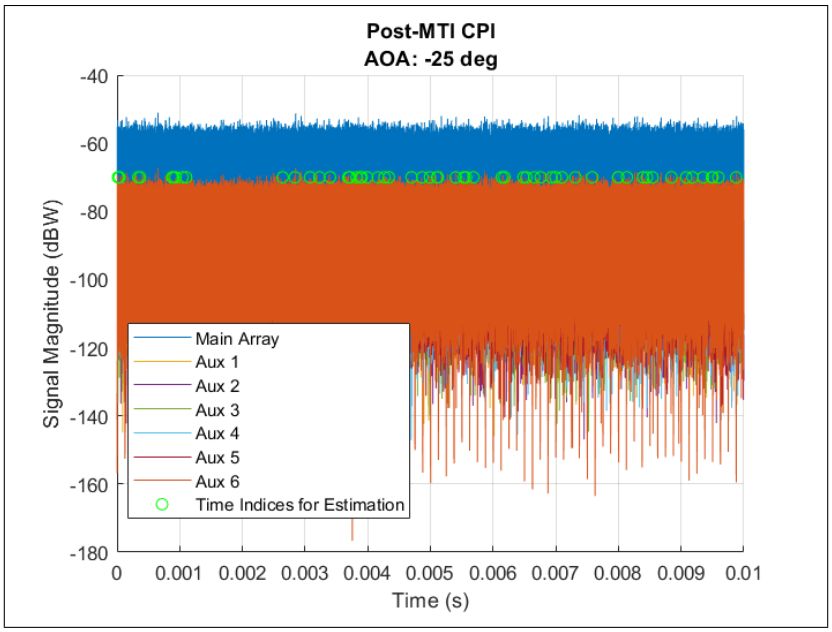

Figure 3.10: Post-MTI output CPIs for the main array and each auxiliary element in an environment containing a white noise jammer. Green circles represent the random time samples selected to estimate the interference statistics.

Similar to the SMI application, $L = 60$ random time samples are selected to estimate the interference covariance matrix between auxiliary elements, $\hat{\boldsymbol{R}}_{Aux}$, and between the main array and auxiliary array, $\hat{\boldsymbol{R}}_{Ay}$. The adaptive auxiliary weights are computed according to Equation 3.11, and the output of SLC processing is computed according to Equation 3.12. Comparison between the SLC output and the output CPI prior to SLC is shown in Figure 3.11.

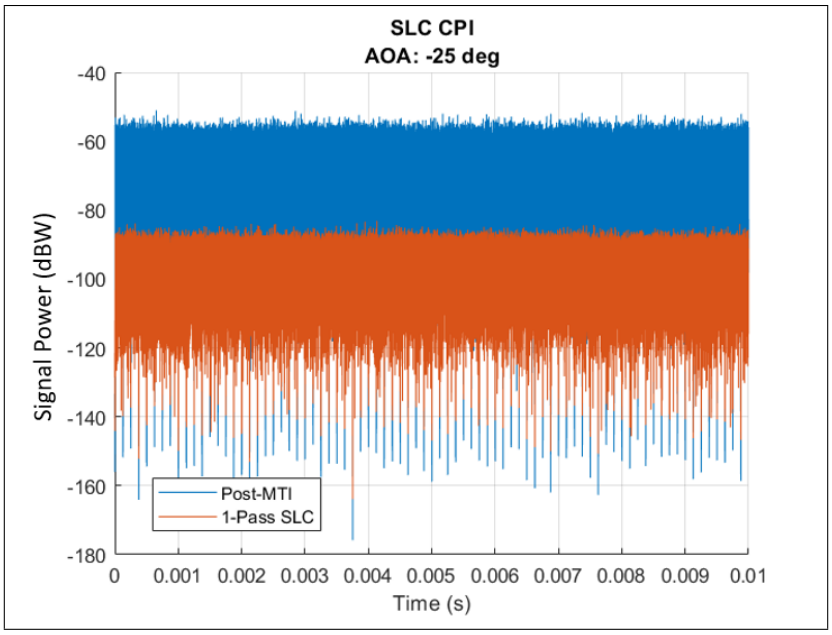

Figure 3.11: Comparison of the output CPIs before and after SLC is shown. As observed, the power of the white noise jammer is reduced.

As observed in Figure 3.11, the power of the white noise jammer is reduced after SLC processing. However, the power of target reflections is still below the noise floor since the modeled target SNR is -10 dB. After Doppler processing and pulse compression, the target is distinguishable and the resulting RDM is shown in Figure 3.12.

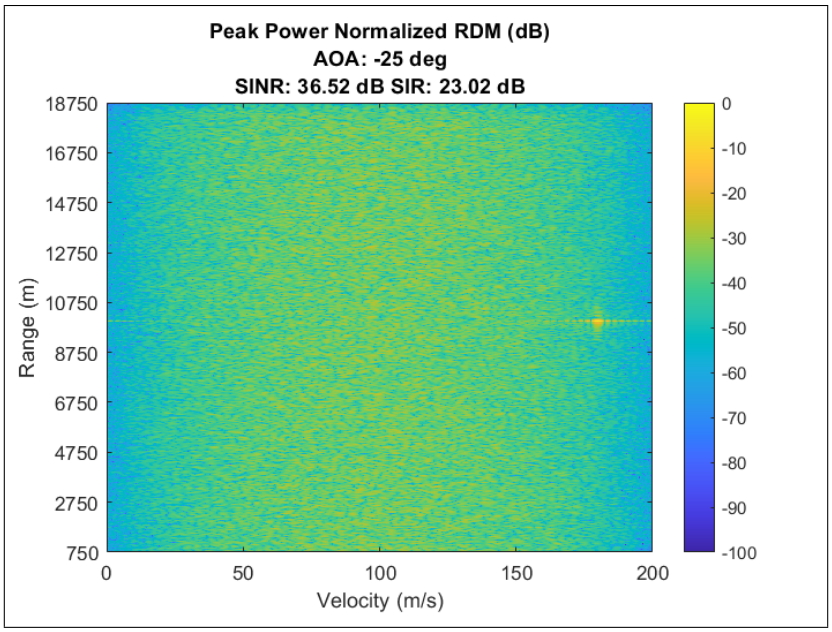

Figure 3.12: RDM post-SLC processing for a scenario with a single white noise jammer. The white noise jammer is suppressed, and the target SINR is recovered.

The resulting antenna patterns are shown in Figure 3.13.

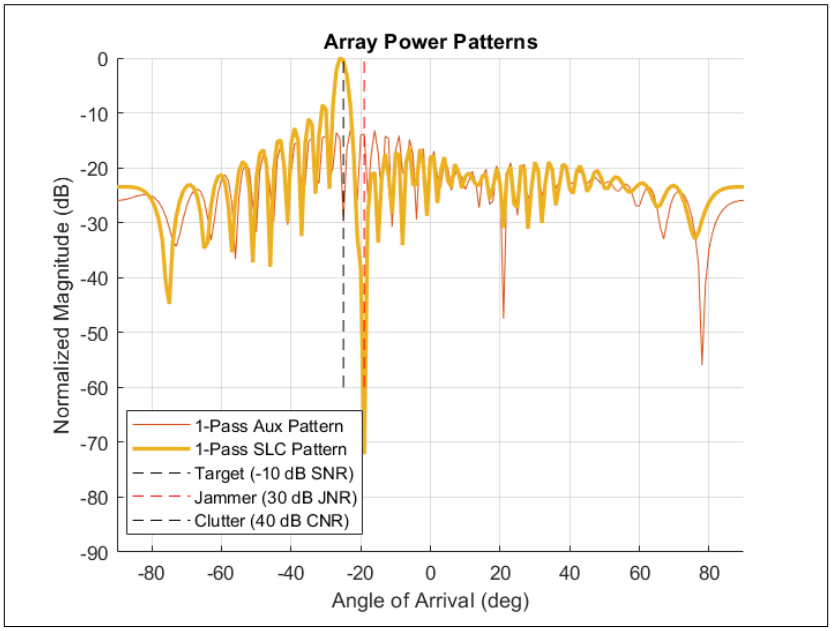

Figure 3.13: The adapted effective pattern (yellow trace) and auxiliary array pattern (pattern) is shown. Notch is placed at the location of the jammer.

The adapted effective pattern is equivalent to the complex difference between the main

array pattern and the adapted auxiliary pattern. As observed in Figure 3.13, a notch is placed at the location of the jammer. Since the spacing between auxiliary elements is greater than $\frac{\lambda}{2}$, grating lobes appear in the resulting auxiliary array pattern. However, the effect of grating lobes in the auxiliary array pattern can be reduced by methods described in [23].

3.4.3 Constrained SLC

As discussed in this section, SLC performance is dependent on low target SNR at the receiver of the auxiliary elements. The formulation of SLC is to minimize the square difference between the output of the main array and the output of the auxiliary array with no intelligence to the difference between target and interference. As target SNR increases above the noise floor, then SLC begins suppressing the target signal resulting in reduced target SNR. This effect is also observed by evaluating the effective adapted antenna pattern. The post-SLC adapted antenna pattern for a scenario with target SNR increased to 18 dB is shown in Figure 3.14.

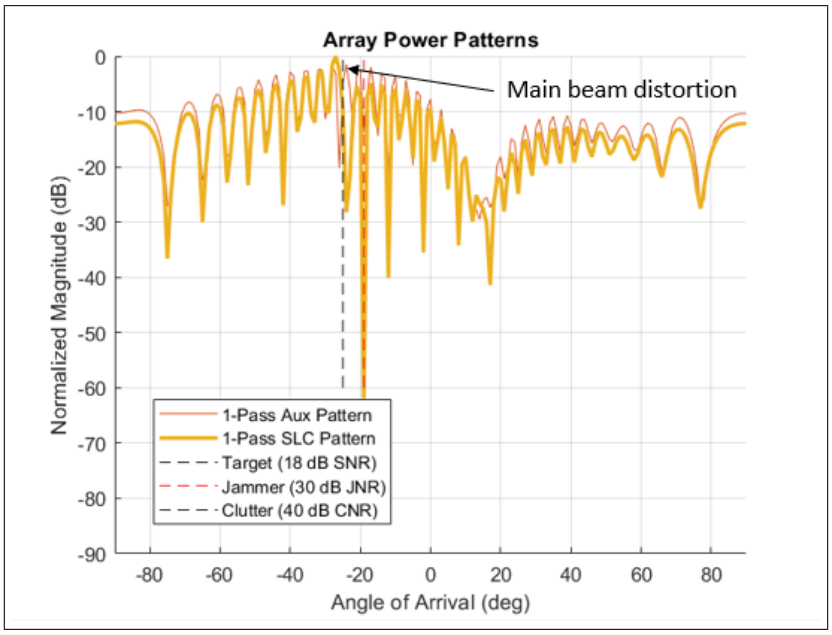

Figure 3.14: Post-SLC adapted antenna pattern for a scenario with target SNR increased 18 dB is shown. Target suppression occurs resulting main beam distortion and reduced target gain.

This effect can be mitigated by adding a linear constraint to the original least squares formulation as follows [7]

$$\boldsymbol{w}_{opt} = \underset{\boldsymbol{w}}{\operatorname{argmin}} \|\boldsymbol{y} - \boldsymbol{A}\boldsymbol{w}_{opt}\|_2^2 \quad \text{subject to} \quad \boldsymbol{C}\boldsymbol{w} = 0, \tag{3.13}$$

where $\boldsymbol{C}$ is an $N_D \times N_{Aux}$ matrix with N_D equal to the number of desired constraint directions. This achieves a similar effect to that of the generalized sidelobe cancellation (GSC) algorithm for fully adaptive arrays detailed in [24]. When the hypothesized target direction is the only desired constraint, then $\boldsymbol{C} = \boldsymbol{c}$ is a $1 \times N_{Aux}$ vector equivalent to $\boldsymbol{a}(\hat{\theta})$. A closed form solution to Equation 3.13 can be found by forming the Lagrangian and using the Karush-Kuhn-Tucker (KKT) stationary condition,

$$\begin{bmatrix} \boldsymbol{w}_{opt} \\ \boldsymbol{\lambda} \end{bmatrix} = \frac{1}{2} \begin{bmatrix} 2\boldsymbol{A}^H\boldsymbol{A} & \boldsymbol{C}^H \\ \boldsymbol{C} & \boldsymbol{0} \end{bmatrix}^{-1} \begin{bmatrix} 2\boldsymbol{A}^H\boldsymbol{y} \\ \boldsymbol{0} \end{bmatrix}, \tag{3.14}$$

where $\boldsymbol{\lambda}$ is the $N_D \times 1$ vector of Lagrange multipliers. Note that each constraint consumes a DOF so the number of interferers that can be suppressed is reduced by N_D.

Following the constrained least squares formulation given in Equation 3.14, the resulting adapted pattern is shown in Figure 3.15.

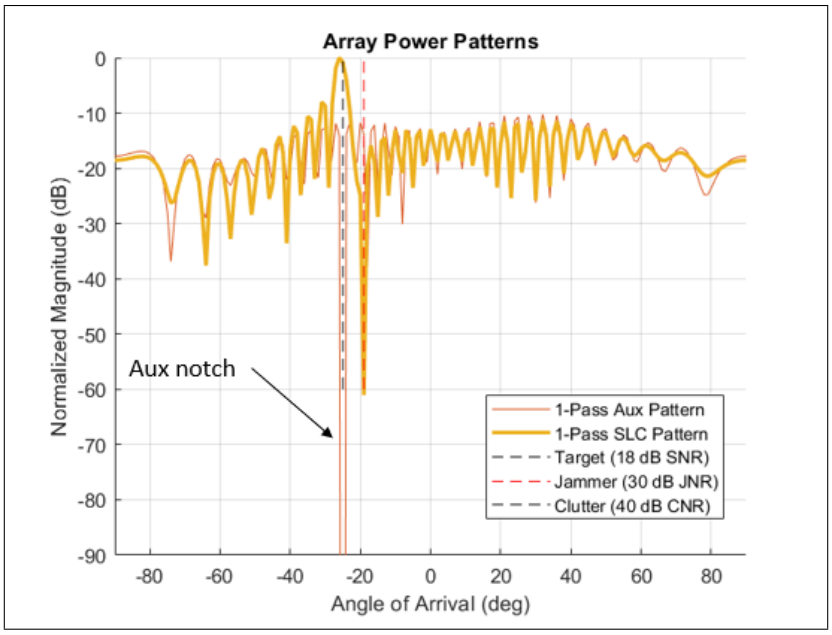

Figure 3.15: Post-SLC adapted antenna pattern (yellow trace) is shown. A constraint on the auxiliary pattern (red trace) is added to prevent target suppression resulting in a notch in the target direction.

As observed in Figure 3.15, the auxiliary array pattern is notched in the direction of the target. Therefore, the complex difference between the main array pattern and the auxiliary pattern does not result in main beam distortion. Unless otherwise stated, SLC is performed with a target direction constraint throughout the remainder of this thesis.

CHAPTER 4

NON-STATIONARY INTERFERENCE

Chapter 4 details the effects that non-stationary time interference can cause on resulting RDMs. Similar to stationary interference, non-stationary interference can reduce the SINR resulting in degraded target detection and tracking performance. Non-stationary interference also introduces additional challenges to SLC suppression which is discussed in this chapter, and an overview of investigated suppression techniques is given.

4.1 Non-Stationary Interference Effects

Possible sources of non-stationary time interference include co-located radar systems. Consider the scenario in Figure 4.1. Multiple radar systems may be deployed in close proximity, and many radar systems operate using LFM pulse-burst waveforms. Therefore, the activity of these co-located radar systems appears as non-stationary interference to the primary radar.

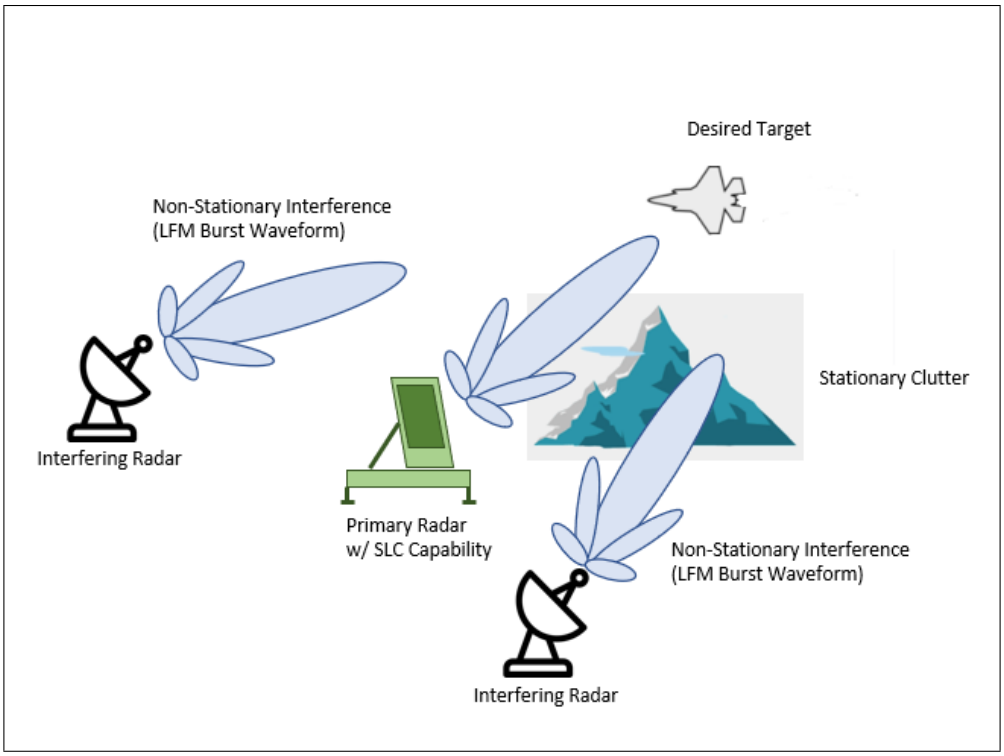

Figure 4.1: Primary radar environment is shown including the presence of non-stationary interference such as co-located radars systems.

4.1.1 Co-Located Radar Interference Model

Interference from co-located radar systems is modeled as an LFM pulse-burst waveform with a different PRI T_I, pulse width τ_I, bandwidth β_I, pulse countM_I, and carrier frequency f_{ci} than the primary radar's waveform. Note that if the interference waveform is identical to the primary radar waveform, then the interference appears as clutter, which can be mitigated by clutter filtering techniques such as MTI filtering. Since many radar systems implement an analog bandpass filter centered around the carrier frequency, interference effects are typically only significant when near the primary radar's carrier frequency [2]. Therefore, this thesis models interference with carrier frequencies only within a few tens of MHz of the primary radar's carrier frequency. Additionally, the interference waveform burst is introduced at a random time sample within the primary radar's CPI. Consider the scenario shown in Figure 4.2 where a single interfering co-located radar is located in a sidelobe of

the main array antenna pattern.

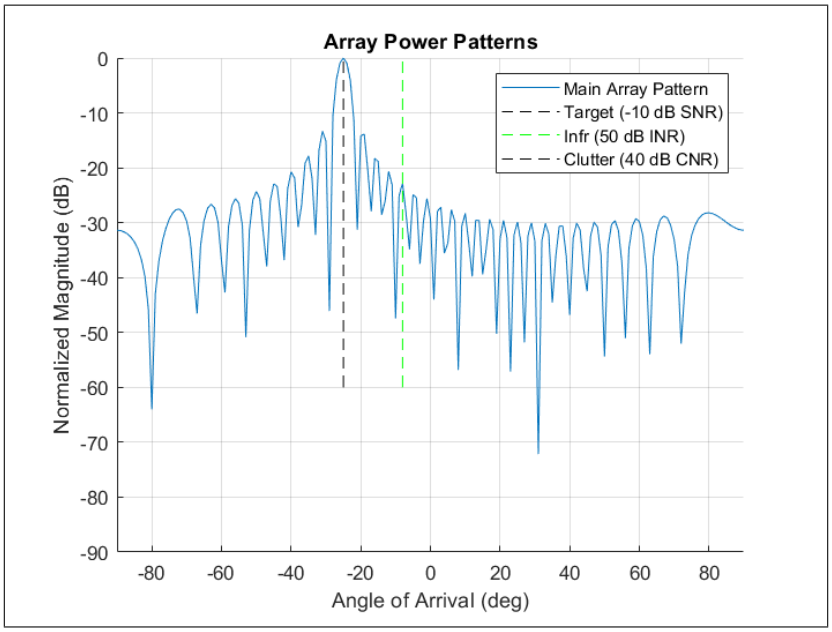

Figure 4.2: The main array is steered to $\hat{\theta} = -25°$. Interference from a co-located radar is located in a sidelobe of the antenna pattern.

Using the radar and waveform model detailed in subsection 3.4.2, a simulated post-MTI output CPI for the primary radar main array is shown in Figure 4.3.

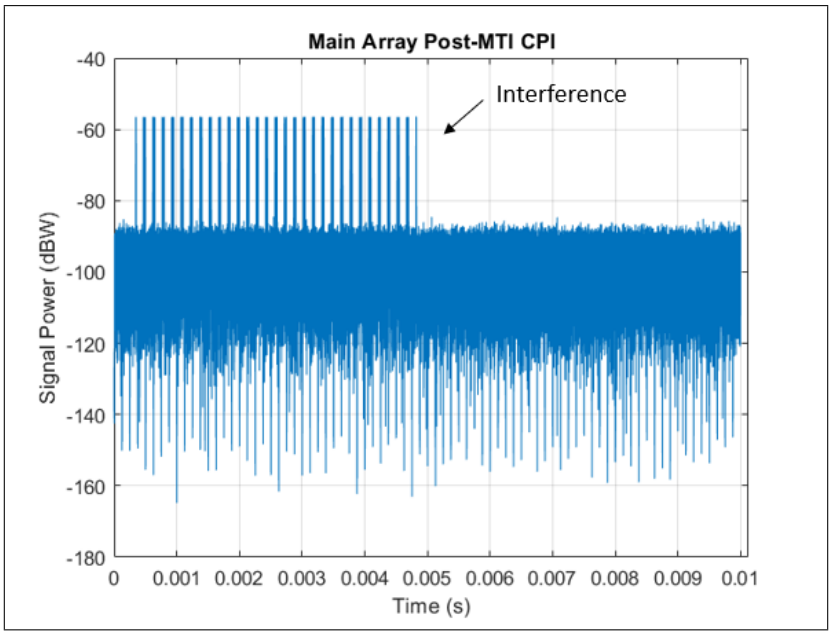

Figure 4.3: Post-MTI output CPI for the main array is shown with non-stationary interference from a co-located radar.

The modeled SNR is -10 dB and the modeled INR is 50 dB. In this scenario, the interference waveform parameters are center frequency $f_c i = 6\,\text{GHz}$, bandwidth $\beta_I = 5\,\text{MHz}$, pulse width $\tau_I = 10\,\mu\text{s}$, PRI $T_I = 150\,\mu\text{s}$, and pulse count $M_I = 30$. As observed, the target power is below the noise level and the interference power is much greater than both the target and the noise power. These power ratios are realistic in many scenarios since target reflections travel two-way in range while interference only travels one-way in range.

4.1.2 Interference Range Aliasing

From Figure 4.4, the CPI is formatted into a 2-D matrix $\boldsymbol{Y}$ separated into columns defined by the primary radar PRI. The time scale is converted to a range scale.

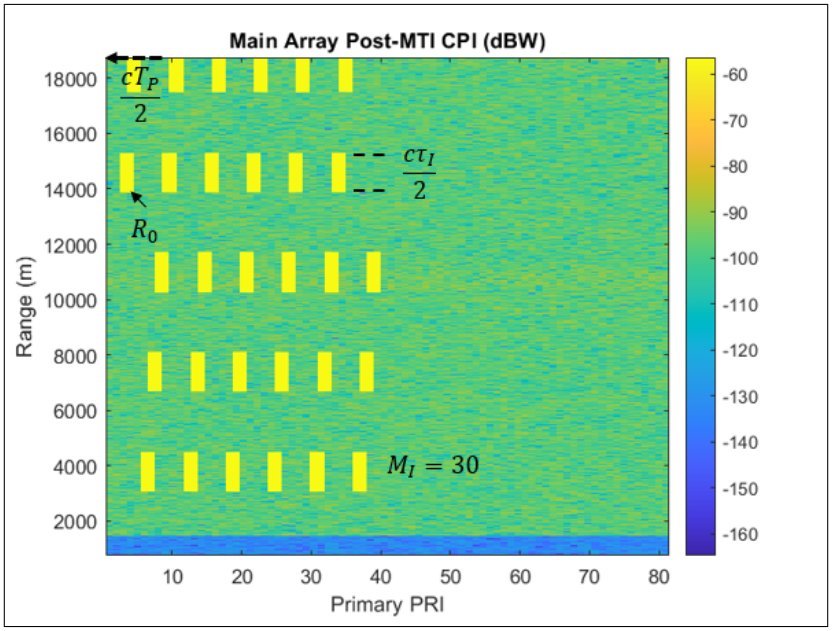

Figure 4.4: The reshaped output CPI for the main array is shown. Non-stationary interference from a co-located radar is present.

The interference pulses are present, and it is observed that the interference PRI T_I is longer than the primary radar PRI T_P. Therefore, the interfering pulses occur at varying ranges which is defined as range aliasing within this thesis. The specific ranges where the

interference pulses occur can be analytically derived as follows

$$R_m = \frac{c\text{mod}\left(t_0 + mT_I, T_P\right)}{2}, \quad m = 0, ..., M_I - 1, \tag{4.1}$$

where t_0 is the start time within the PRI of the first interfering pulse. If t_I is the start time of the interference pulse-burst within the primary radar CPI, then t_0 is equivalent to $t_0 = \text{mod}\left(t_I, T_P\right)$. As observed in Figure 4.4, all R_m are not necessarily unique, and the interference begins repeating at the same ranges when $t_m = t_0$ for $m > 0$. This occurs when $\text{mod}\left(mT_I, T_P\right) = 0$. Therefore, the number of unique R_m is

$$N_{Alias} = \text{lcm}\left(T_I, T_P\right)/T_I. \tag{4.2}$$

In Figure 4.4, $T_I = 125\,\mu\text{s}$ and $T_P = 150\,\mu\text{s}$ so $N_{Alias} = 5$ which aligns with what is observed in Figure 4.4. Note that N_{Alias} is maximum for a given T_I and T_P when T_I and T_P are co-prime. For an example when $T_I = 120\,\mu\text{s}$, then $N_{Alias} = 25$. The reshaped output CPI for a scenario with $T_I = 120\,\mu\text{s}$ is shown in Figure 4.5.

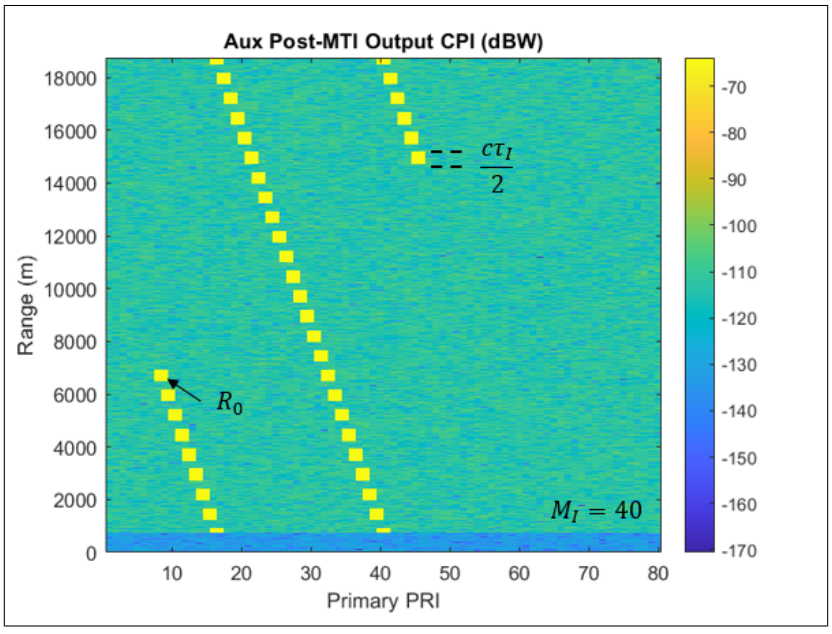

Figure 4.5: The reshaped output CPI for the main array is shown. Non-stationary interference from a co-located radar resulting in greater range aliasing is present.

4.1.3 Interference Doppler Pattern

Doppler processing on the data in Figure 4.4 is performed as detailed in subsection 2.3.2. This is equivalent to a column DFT on the data in Figure 4.4. The resulting matrix $\boldsymbol{Y}_{DP}$ is shown in Figure 4.6.

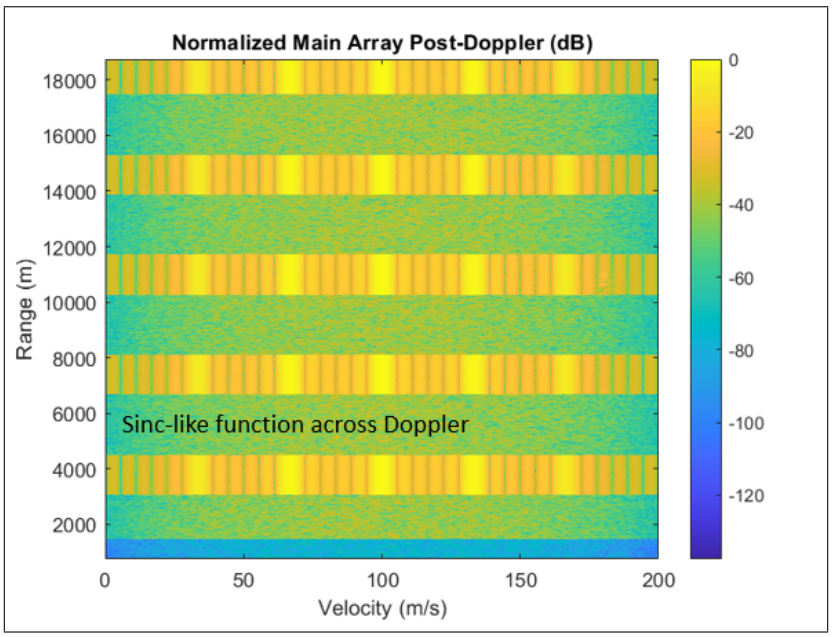

Figure 4.6: The resulting matrix after Doppler processing is shown. The effects of non-stationary interference from a co-located radar is present.

As observed in Figure 4.6, a sinc pattern results at each unique R_m previously defined in Equation 4.1.

The sinc pattern at each R_m is more easily analyzed in a simple case where only two interference pulses occur across all PRIs. The DFT to perform Doppler processing at the R_m range index for a specific Doppler frequency, f_D, is represented by

$$Y_{DP}[f_D, R_m] = \sum_{m=0}^{M} Y[m, R_m] e^{-j2\pi f_D m}. \tag{4.3}$$

Take m_1 as the PRI where the first interference pulse occurs and m_2 as the PRI where the second interference pulse occurs. The nulls in the pattern at that R_m occur when

$Y_{DP}[f_D, R_m] = 0$. When there are only two interfering pulses, the nulls occur when

$$
\begin{aligned}
e^{-j2\pi f_D m_1} &= -e^{-j2\pi f_D m_2} \\
2\pi f_D m_2 &= 2\pi f_D m_1 \pm (2k+1)\pi, \quad k = 0, ..., \infty \\
f_D &= \frac{2k \pm 1}{2(m_2 - m_1)}, \quad k = 0, ..., \infty.
\end{aligned} \tag{4.4}
$$

Therefore, the sinc pattern at each R_m after Doppler processing is dependent on the number of PRIs between successive interference pulses appearing at the same range.

4.1.4 Interference RDM Effects

After pulse compression is performed as detailed in subsection 2.3.3, the resulting RDM is shown in Figure 4.7.

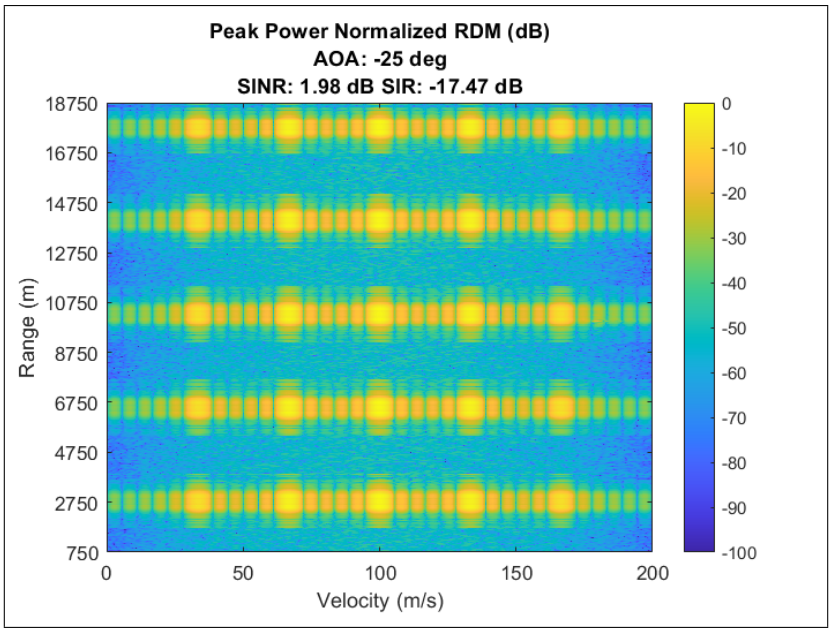

Figure 4.7: RDM is shown with non-stationary interference from a co-located radar.

As observed, the interference is the primary component within the RDM masking the target signal and degrading the resulting SINR. The analysis of the interference structure within the RDM is predictable when the interference parameters are known as detailed in subsection 4.1.2 and subsection 4.1.3.

4.1.5 SLC Challenges with Non-Stationary Interference

SLC is performed by using an estimate of the spatial interference statistics across the array, specifically the covariance between auxiliary elements $\hat{\boldsymbol{R}}_{Aux}$ and the covariance between auxiliary elements and the main array $\hat{\boldsymbol{R}}_{Ay}$. From subsection 3.4.2 and Figure 3.10, the estimate of a stationary interference source such a white noise jammer is formed by randomly selecting $L = 60$ samples within the output CPI. This is possible since the statistics of interference do not change with time. Using the same method for non-stationary interference source such as a co-located radar, $L = 60$ samples are selected to estimate the interference statistics as shown in Figure 4.8.

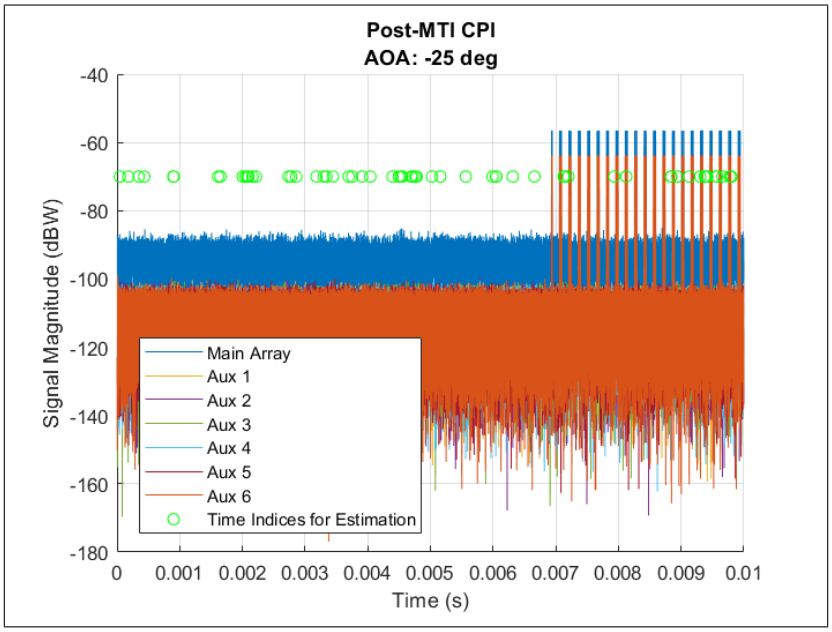

Figure 4.8: Post-MTI output CPI is shown for the main array and each auxiliary element. Non-stationary interference from a co-located radar is present. Green circles represent random time samples selected to estimate the interference statistics.

As observed in Figure 4.8, very few of the $L = 60$ samples contain interference. From subsection 3.3.2 and [20], recall that the estimate of interference degrades as the number of samples used to estimate the interference decreases. Therefore, suppression performance is also degraded. The effective antenna pattern is shown in Figure 4.9 and the resulting RDM is shown in Figure 4.10.

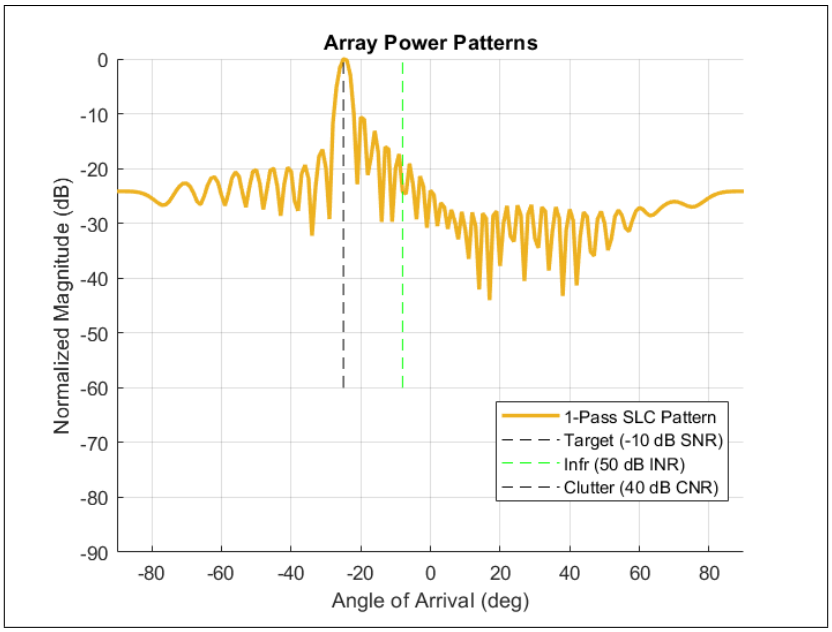

Figure 4.9: Post-SLC antenna pattern does not form an effective notch in the direction of the interference due to poor estimation of the interference statistics.

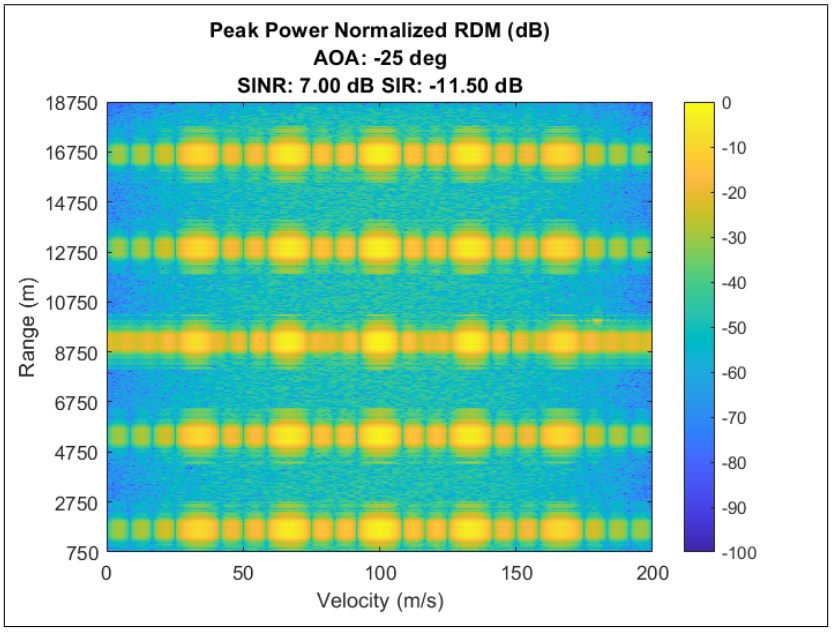

Figure 4.10: Post-SLC RDM is shown. The SINR remains degraded after SLC processing due to poor estimation of the interference statistics.

As observed, no notch is formed in the direction of the interference which results in poor SINR within the RDM. Simulating the scenario shown in Figure 4.2 using the radar and waveform model given in this section, the performance of SLC with random selection

over 30 simulations with random variations in noise and interference location within the CPI is shown in Table 4.1. The floating point operations (FLOP)s are only measured for the computation required to generate the estimated covariance matrices $\hat{\boldsymbol{R}}_{Aux}$ and $\hat{\boldsymbol{R}}_{Ay}$.

Table 4.1: The performance and computation costs are shown for SLC with random selection. Performance is measured over 30 simulations.

Method	Mean SINR (dB)	Min SINR (dB)	Var SINR (dB)	FLOP
Random Selection (L=60)	36.17	10.28	41.44	5 k

As indicated by the minimum SINR and variance of the SINR, more robust methods are required to estimate non-stationary interference to improve the performance of SLC. These methods are proposed in the following chapters.

4.2 Non-Stationary Interference Suppression

4.2.1 SLC with Entire CPI

One method to improve the interference estimation is to use all samples within the CPI to generate the estimated covariance matrices. This ensures that all samples containing interference are used to generate its estimate. However, since the radar evaluated in this thesis operates by CPI block processing as described in section 3.2, this becomes computationally expensive as the number of samples within the CPI N_S or the number of auxiliary elements N_{Aux} increases. The required FLOP to generate just $\hat{\boldsymbol{R}}_{Aux}$ is $2N_{Aux}^2 N_S$. Using the entire CPI also ensures that the target signal is included in the interference estimate. As the target SNR increases and without accurate directional constraints, this results in target suppression as discussed in subsection 3.4.3. Therefore, SLC with accurate target constraint is required. The performance of this method is shown in Table 4.2 when evaluated for the scenario depicted in Figure 4.2 over 30 simulations.

Table 4.2: The performance and computation costs are shown for SLC with random selection and entire CPI.

Method	Mean SINR (dB)	Min SINR (dB)	Var SINR (dB)	FLOP
Random Selection (L=60)	36.17	10.28	41.44	5 k
Entire CPI	37.19	37.11	0.00	21 M

As observed, SLC performance is improved when using the entire CPI at the cost of higher computation.

4.2.2 Additional Algorithms Reviewed

Alternate algorithms to suppress mutual radar interference were also reviewed. The effects of mutual radar interference, particularly to the application of vehicle sensors, is presented in [25]. Many spatial suppression techniques are dependent on the adaptability of every antenna element which is too costly for many large tactical phased arrays. Therefore, this thesis focuses on techniques that can be incorporated with subarray architectures. Certain commercial radar systems, which are expected to operate within close proximity, transmit and receive orthogonal waveforms to mitigate the effects of mutual radar interference [26], [27]. However, this method has the limitation that waveform design between radar systems must be coordinated before deployment. Another algorithm proposed to mitigate mutual radar interference is the recursive implementation of a minimum mean-square error formulation for adaptive pulse compression proposed in [28], [29]. This algorithm has the limitation that it requires at least a single matrix inversion of size $N_\tau \times N_\tau$ for each range cell where N_τ is the length of the sampled primary radar waveform pulse. This becomes increasingly costly when the number of searched range cells is large, which is the case for many ground-based radar applications. An algorithm is also proposed in [30] where the interference samples are directly removed in the time domain. However, this algorithm has the limitation that all interference samples must be identified to eliminate interference artifacts within the RDM. Other time domain suppression algorithms are also proposed in [31], [32]. In contrast, SLC only requires an estimate of the interference statistics from a

subset of interference samples to spatially suppress the interference. Additionally, open-loop methods such as non-adaptively notching the antenna pattern was reviewed. This can be performed by phase-weighting the main array elements where the weights are identified through an iterative semidefinite convex optimization problem [33]. However, this method requires that the locations of the co-located radars are known a-priori, and iterative programming can become computationally costly.

Instead, the next chapters propose algorithms to adaptively estimate the spatial statistics of interference from co-located radars for suppression through SLC.

CHAPTER 5

ADAPTIVE CORRELATION ESTIMATION

As demonstrated in this thesis, SLC performance is dependent on effective estimation of the interference statistics across the array elements. With stationary interference sources, or sources whose statistics do not change over time, estimation is trivial and can be performed by random sampling the CPI. However, random sampling the CPI to suppress non-stationary interference results in high variance in the resulting SINR. This chapter discusses the first proposed method to increase robustness when estimating non-stationary interference, such as co-located radar interference, for SLC suppression.

5.1 Correlation Estimation Method

The effective estimation of interference is dependent upon selecting samples within the CPI that contain interference. One proposed method to adaptively select such samples is to take the samples resulting in high correlation when computed between the outputs of two sensors [5]. The Pearson correlation coefficient, $\rho_{X,Y}$, is the measure of correlation that is used for this method,

$$\rho_{X,Y} = \frac{\mathbf{E}\{(X - \mu_X)(Y - \mu_Y)\}}{\sigma_X \sigma_Y}. \tag{5.1}$$

In discrete form, the Pearson correlation coefficient is computed as

$$\rho_{X,Y} = \frac{\sum (x_i - \bar{x})(y_i - \bar{y})}{\sqrt{\sum (x_i - \bar{x})^2}\sqrt{\sum (y_i - \bar{y})^2}}. \tag{5.2}$$

5.1.1 Correlation Analysis

This subsection provides analysis of the method proposed in [5] to show how correlation can be used to identify interference samples. As detailed in earlier chapters, interfer-

ence typically has high INR due to its one-way signal travel. Conversely, target reflections typically have low SNR due to small RCS and their two-way signal travel. Additionally, individual auxiliary elements have low directivity in comparison to the beamformed main array, which reduces their gain in any specific direction. Therefore, in most practical scenarios, the target SNR in the output CPI of an individual element is below 0 dB and much less than the interference INR. An example output CPI for two individual auxiliary elements with co-located radar interference is shown in Figure 5.1.

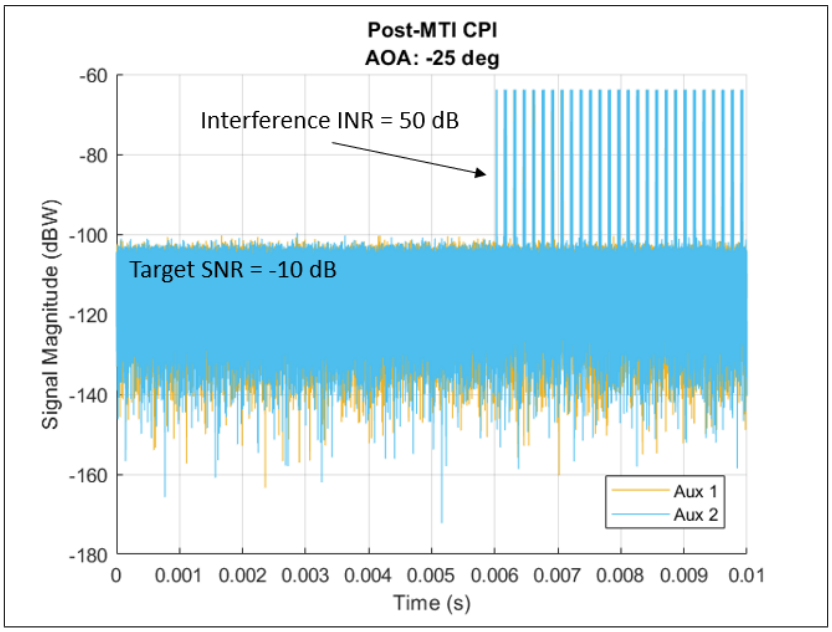

Figure 5.1: The post-MTI output CPIs are shown for two individual auxiliary elements. Co-located radar interference is observable, and target reflections are below the noise level.

The modeled target SNR is -10 dB and the modeled INR is 50 dB. Only the interference is observable above the noise floor, and random noise is the dominant signal at all time instances where the interference is not located.

Represent the measured noise in the output CPI for two different auxiliary elements as $n_1(t)$ and $n_2(t)$ where $\mathbf{E}\{n_1^2(t)\} = \mathbf{E}\{n_2^2(t)\} = \sigma_n^2$. Noise is random and uncorrelated from element to element so that $\mathbf{E}\{n_1(t)n_2(t)\} = 0$. Therefore, the expected correlation

between noise measurements on two different auxiliary elements is zero,

$$\begin{aligned}\rho_{n_1,n_2} &= \frac{\mathbf{E}\{(n_1(t)-\mu_{n_1})(n_2(t)-\mu_{n_2})\}}{\sigma_{n_1}\sigma_{n_{A2}}} \\ &= \frac{\mathbf{E}\{n_1(t)n_2(t)\}}{\sigma_n^2} \\ &= 0.\end{aligned} \tag{5.3}$$

Denote $s_1(t)$ and $s_2(t)$ as the measured target signal plus noise in the output CPI for two different auxiliary elements where the signal and noise are uncorrelated and $\mathbf{E}\{s_1^2(t)\} = \mathbf{E}\{(A_{tgt}+\sigma_{n_1})^2\} = A_{tgt}^2 + \sigma_n^2$. In samples where both the target and noise is present, the expected correlation between two auxiliary elements is

$$\begin{aligned}\rho_{s_1,s_2} &= \frac{\mathbf{E}\{(s_1(t)-\mu_{s_1})(s_2(t)-\mu_{s_2})\}}{\sigma_{s_1}\sigma_{s_2}} \\ &= \frac{\mathbf{E}\{(A_{tgt}+n_1)(A_{tgt}+n_2)\}}{A_{tgt}^2+\sigma_n^2} \\ &= \frac{\mathbf{E}\{A_{tgt}^2 + A_{tgt}(n_1+n_2)+n_1n_2\}}{A_{tgt}^2+\sigma_n^2} \\ &= \frac{A_{tgt}^2}{A_{tgt}^2+\sigma_n^2} \\ &= \frac{SNR}{1+SNR}, \quad SNR = \frac{A_{tgt}^2}{\sigma_n^2}.\end{aligned} \tag{5.4}$$

As shown in Equation 5.4, the expected correlation for samples containing both target and noise can be expressed as a function of the linear SNR. When the target SNR is -10 dB, then the expected correlation is $\rho_{s_1,s_2} = 0.09$.

Denote $i_1(t)$ and $i_2(t)$ as the measured interference plus noise in the output CPI for two different auxiliary elements where the interference and noise are uncorrelated and $\mathbf{E}\{i_1^2(t)\} = \mathbf{E}\{(A_{ifr}+\sigma_{n_1})^2\} = A_{ifr}^2 + \sigma_{n_1}^2$. Following a similar analysis, in samples where both the interference and noise is present, the expected correlation between two auxiliary elements is

$$\rho_{i_1,i_2} = \frac{INR}{1+INR}, \quad INR = \frac{A_{ifr}^2}{\sigma_n^2}. \tag{5.5}$$

When the interference INR is 50 dB, then the expected correlation is computed as $\rho_{i_1,i_2} = 1$. Taking the results from Equation 5.4 and Equation 5.5, the correlation between elements versus the SNR of a signal in the presence of Gaussian noise is shown in Figure 5.2.

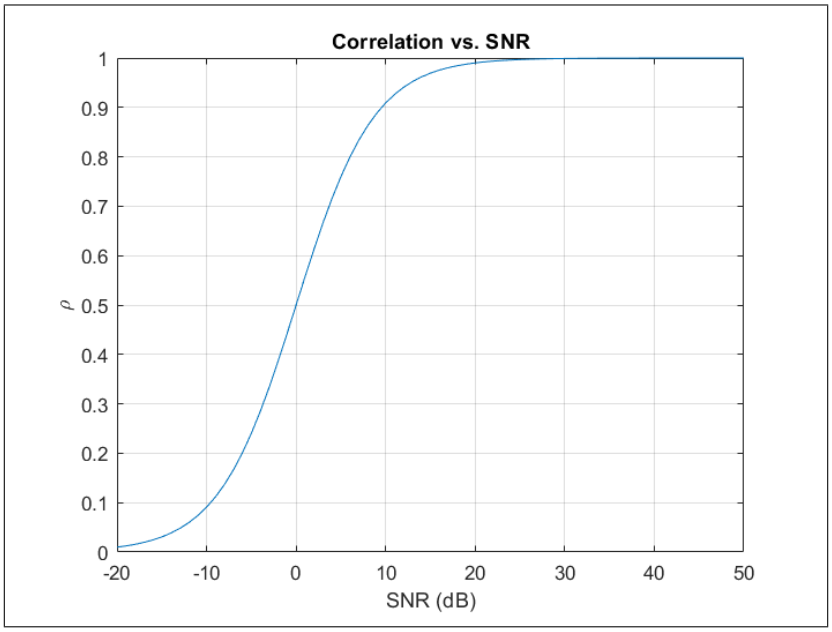

Figure 5.2: The expected correlation between elements versus the SNR of a signal in the presence of Gaussian noise.

This analysis shows that for scenarios with low target SNR and high interference INR, high correlation only occurs for samples containing interference. Noise dominant samples and target samples result in low correlation. Therefore, correlation can be used as a method to adaptively identify samples containing strong interference. Additionally, this thesis proposes that correlation is measured between two auxiliary elements instead of the main array to reduce sensitivity to the target, since the target SNR is higher in the main array output. This helps to prevent including target samples within the interference estimate. A detailed approach and example is given in the following section.

5.1.2 C-SLC Application Steps

The proposed steps to perform correlation with sidelobe cancellation (C-SLC) are as follows:

1. Split post-MTI output CPI for two auxiliary elements into smaller windows of time
    - Selection of window size is discussed in subsection 5.1.3
2. Compute correlation between the two auxiliary elements for each window per Equation 5.2
3. Randomly select L samples from windows that exceed a specified correlation threshold, ρ_{thresh}
    - If no correlation exceeds ρ_{thresh}, perform no SLC
4. Perform SLC as detailed in section 3.4 using the L samples identified in step 3

Note that the decision to perform SLC and selecting interference samples does not require knowledge of absolute amplitude levels within the CPI. Only a measure of correlation, ranging from 0 to 1, is evaluated to identify samples. This is beneficial since absolute amplitudes are difficult to analyze and predict in certain radar systems.

The correlation threshold, ρ_{thresh}, in step 3 can be intelligently selected for an expected target and interference scenario. The expected correlation is a function of target SNR and interference INR as defined in Equation 5.4 and Equation 5.5. If the target SNR is expected to be less than 0 dB while the interference INR is expected to be much greater than 0 dB, then specifying $\rho_{thresh} > 0.5$ helps to prevent selection of target samples while concentrating samples on interference.

5.1.3 C-SLC Application Example

Consider the scenario in Figure 4.2 where interference from a co-located radar is in a sidelobe of the primary radar's main array pattern. The modeled target SNR is -10 dB and the modeled interference INR is -50 dB. Performing C-SLC begins by splitting the output CPI for two auxiliary elements into smaller windows of time as shown in Figure 5.3.

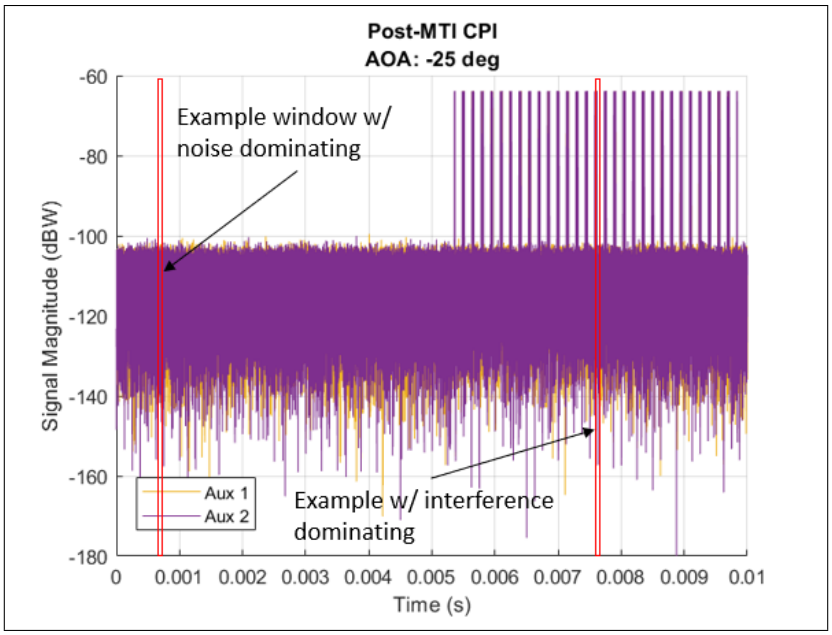

Figure 5.3: The output CPI for two auxiliary elements is split into smaller windows. Two example windows are shown - one with noise as the dominant signal and another with interference as the dominant signal.

In this specific example, the output CPI is split into 1000 windows. For each window, the correlation is computed between the two auxiliary elements per Equation 5.2. The resulting correlation for each window is shown in Figure 5.4.

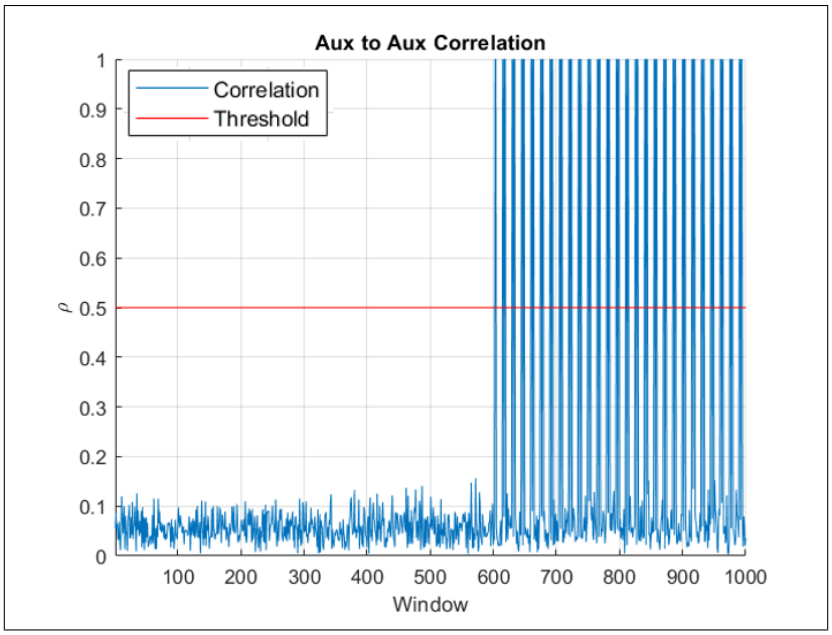

Figure 5.4: The computed correlation for each window is shown with $\rho_{thresh} = 0.5$. Note that high correlation occurs only for windows containing interference.

Comparing the computed correlation in Figure 5.4 to the output CPI in Figure 5.3, it is observed that high correlation occurs only for windows containing interference. In this example, the correlation threshold is defined to be $\rho_{thresh} = 0.5$. $L = 60$ samples are randomly selected from the windows whose correlation exceed ρ_{thresh}. These samples are shown overlaid on the output CPI in Figure 5.5.

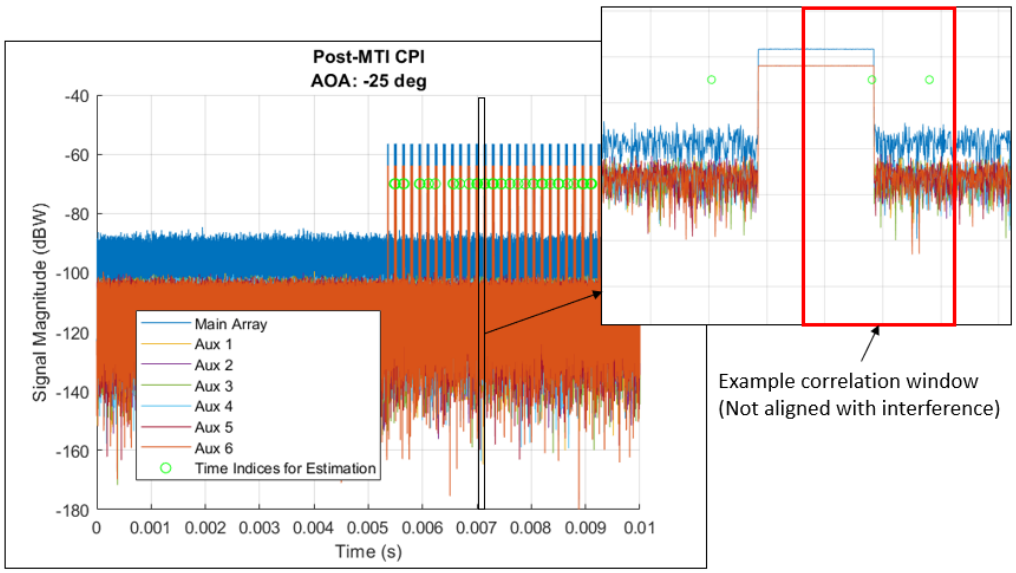

Figure 5.5: The output CPI is shown for the main array and each auxiliary element. Co-located radar interference is observable, and the samples selected via C-SLC are indicated by the green circles.

As observed in Figure 5.5, all selected samples are localized near the interference waveform. However, not all samples are guaranteed to contain interference. This is because the time windows used to compute correlation may not perfectly align with the interference pulse. Specifying smaller windows lead to more localized sampling, but less averaging of noisy data. For all cases tested, using correlation to sample the CPI improves upon random sampling. Since a majority of the $L = 60$ samples in Figure 5.5 contain interference, the interference statistics are better estimated.

SLC is performed as detailed in section 3.4 using the $L = 60$ samples identified in Figure 5.5. As detailed in section 3.4, this involves solving the constrained least squares problem minimizing the square difference between the output of the main array and the adaptively weighted auxiliary array when evaluated at the $L = 60$ samples. The resulting effective antenna pattern is shown in Figure 5.6.

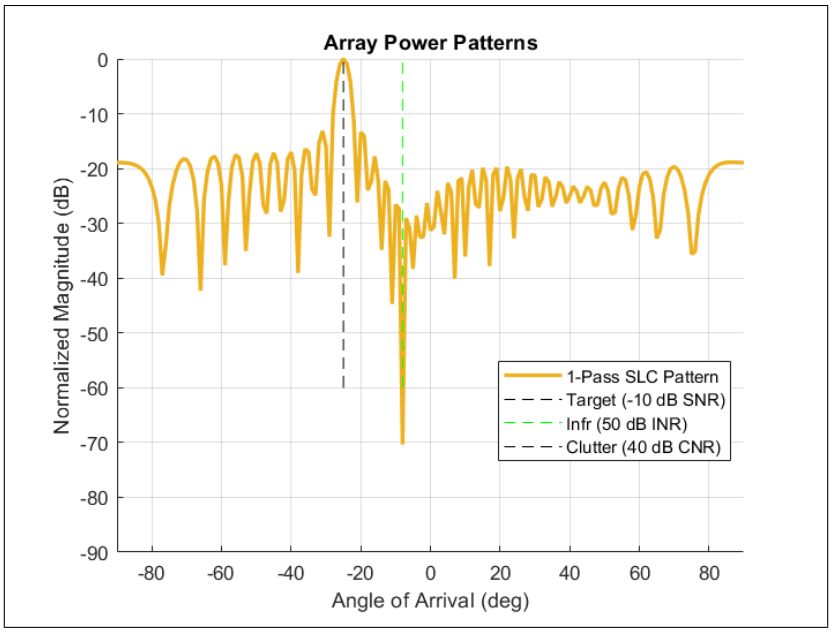

Figure 5.6: Post C-SLC antenna pattern is shown. A notch is formed in the direction of the interference.

As observed in Figure 5.6, a notch is formed in the direction of the interference. The resulting RDM is shown in Figure 5.7.

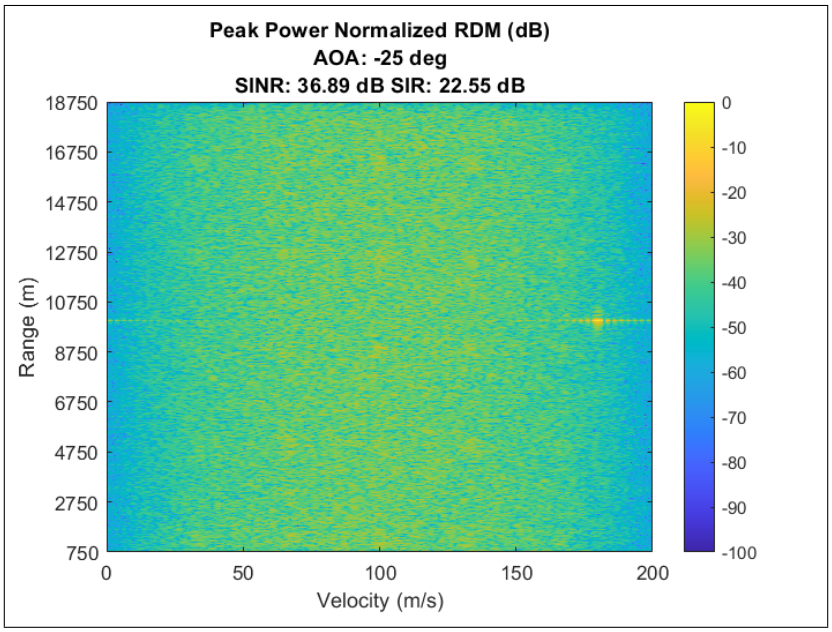

Figure 5.7: Post C-SLC RDM is shown. The SINR is recovered and the target is clearly observable.

As observed in Figure 5.7, the resulting SINR is recovered and the target is clearly observable. Comparison of C-SLC to methods discussed earlier in this thesis is shown in Table 5.1. For each method, 30 simulations are performed with random variations in noise and interference location within the CPI.

Table 5.1: The performance and computation costs are compared for the correlation method. Performance is measured over 30 simulations.

Method	Mean SINR (dB)	Min SINR (dB)	Var SINR (dB)	FLOP
Random Selection (L=60)	36.17	10.28	41.44	5 k
Entire CPI	37.19	37.11	0.00	21 M
C-SLC (L=60)	36.89	36.68	0.02	2.5 M

As expected, the correlation method achieves much better performance than that of random selection with much lower computation costs than that of using the entire CPI. This is clear by comparing the variance and FLOP for each of the methods. Note that SLC and C-SLC can also be performed by selecting samples to estimate interference after Doppler processing. This is discussed in the Appendix.

When limiting the number of samples L used to estimate interference, improvement over the correlation method is still possible. As shown in Figure 5.5, not all L samples are guaranteed to capture interference. Additionally, C-SLC does not differentiate between strong target samples and strong interference samples, since both result in high correlation between auxiliary elements. Therefore, a method involving machine learning is proposed in the next chapter.

CHAPTER 6

MACHINE LEARNING DRIVEN METHODS

As detailed in subsection 3.3.2, SLC performance improves when more interference samples are used to estimate its statistics in the presence of noise. If the number of samples used to estimate interference is constrained to L, then suppression performance improves as more of the L samples contain interference. This chapter proposes a method which incorporates machine learning with SLC to increase the proportion of allotted samples containing interference. Additionally, the proposed algorithm provides discrimination of interference from strong target samples which is not possible with C-SLC. Application of this machine learning method requires additional assumptions of the co-located radar interference which are detailed in this chapter.

6.1 Radar Environment Assumptions

Consider the scenario in Figure 6.1.

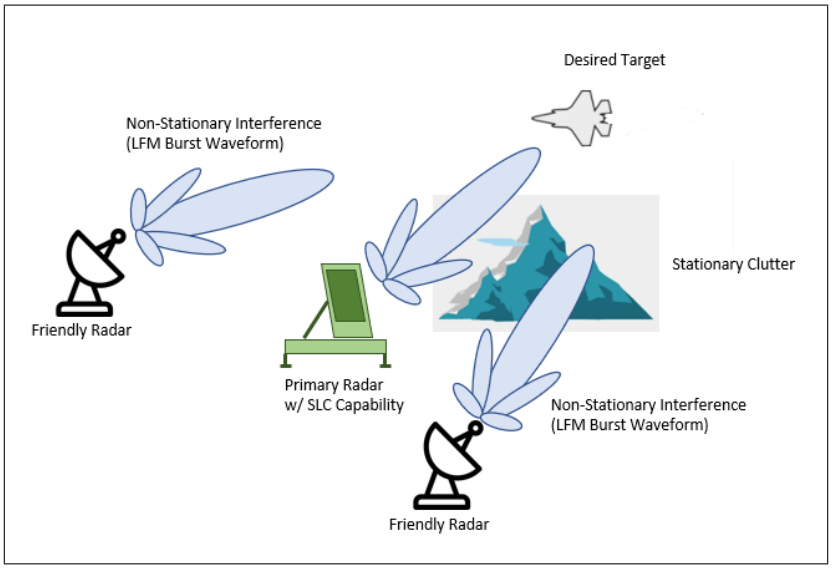

Figure 6.1: Primary radar environment is shown including the presence of friendly co-located radar radar systems.

Similar to Figure 4.1, there are non-stationary interference sources in the form of co-located radars. However, in Figure 6.1, these co-located radars are friendly systems for which the primary radar has prior knowledge. Specifically, the primary radar knows the set of all waveform pulses that the co-located radars may transmit. No other information is known, including the pulse count, PRF, or physical location. Practically, this could be the scenario where friendly radar systems are in close proximity to the primary radar, but no synchronized communication between the radar systems exists and the specific location of the co-located radars may not be known. These radars may also operate using a variety of known pulse-burst waveforms. This scenario allows for the application of machine learning with SLC. This applies the concepts introduced in [6] which classifies audio data through the use of spectrograms and CNNs. Similar techniques for classification of electromagnetic signals, including jamming, has been proposed in [34], [35], [36].

An overview of the proposed steps to incorporate machine learning with SLC are as follows:

1. Compute TFIs of 1-D signals for classification by a CNN.
2. Generate a replica of the identified interference pulse
3. Perform matched filtering with the replica and the output CPI to identify interference samples
4. Perform SLC evaluated at the samples identified in the previous step

These steps are detailed along with an example in the following sections.

6.2 Machine Learning Tools

Two significant steps involved with any machine learning application are feature extraction and model training [6]. Feature extraction involves pre-processing the data to generate

better distinguishers between classes, and model training involves using the extracted features to train a model for future data classification. The machine learning model for the SLC application must be time-invariant since the interference waveform can be located anywhere anywhere within the CPI. The method proposed in [6] performs waveform classification by converting the signal's time domain into a TFI and training a CNN to learn the data and make predictions. Each of these steps are detailed in the following subsections.

6.2.1 Feature Extraction

The feature extraction method used for this application is to convert each PRI of the CPI into a TFI. The TFI for the m^{th} PRI is computed using the spectrogram. Taking $r_m(t)$ to be the m^{th} PRI at the output of a single receiver, then its spectrogram is computed as

$$\text{spect}\{r_m(t)\}(\tau,\omega) = |R_m(\tau,\omega)|^2 = |\int_{-\infty}^{\infty} r_m(t)w(t-\tau)e^{-j\omega t}dt|^2, \tag{6.1}$$

where $w(\tau)$ is a windowing function such as the Hamming window. The spectrograms are shown as single layer images in Figure 6.2.

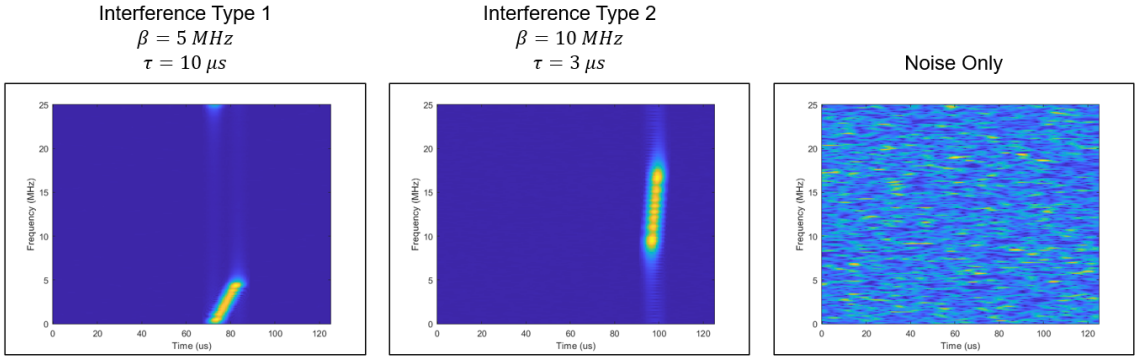

Figure 6.2: Example spectrograms for specific waveforms are shown.

These spectrograms are computed using a 256 sample fast Fourier transform (FFT), a 256 sample Hamming window equivalent to $10.24\,\mu s$ at the modeled sample rate defined in section 2.3, and an overlap of 250 samples. Window lengths are chosen to optimize the trade-off between temporal resolution and frequency resolution. Longer windows provide

higher frequency resolution but less time resolution, while shorter windows provide higher time resolution but less frequency resolution [37]. Increasing the overlap maintains higher time resolution with longer windows (and therefore frequency resolution), but this is at the cost of more computations. The resulting TFIs in Figure 6.2 are used to train a CNN model. In this thesis, an example scenario containing 5 distinct interference pulses is modeled. For a scenario involving 5 interference pulses, 7 total classes are learned - the 5 interference pulses, the primary radar pulse, and noise. These waveforms are detailed in Table 6.1.

Table 6.1: Waveform parameters for the 7 classes modeled in this thesis are provided.

Waveform Label	Center Frequency (GHz)	Bandwidth (MHz)	Pulse Width (μs)	PRI (μs)	Pulse Count
Primary Radar	6.000	5	5	125	81
Interference 1	6.000	5	10	150	30
Interference 2	6.008	10	3	120	40
Interference 3	6.020	2	15	145	20
Interference 4	6.000	30	1	100	50
Interference 5	6.005	15	10	175	15
Noise	-	-	-	-	-

6.2.2 CNN Model

CNNs are spatially invariant machine learning models typically used to classify images [38]. When 1-D signals are converted to TFIs as in subsection 6.2.1, then CNNs can provide classification of the 1-D signals which are invariant to time and frequency offset. CNNs primarily consist of 2D-convolution layers and a linear classifier layer, and the convolution kernel values are the primary parameters solved for during training.

Radar applications typically require real-time processing to react to the continually evolving environment. This motivates the use of a CNN model which requires fewer computations and memory. SqueezeNet is a CNN model which achieves similar performance to that of larger CNN models such as AlexNet but with less computation and memory costs [39]. The architecture of SqueezeNet is shown in Figure 6.3.

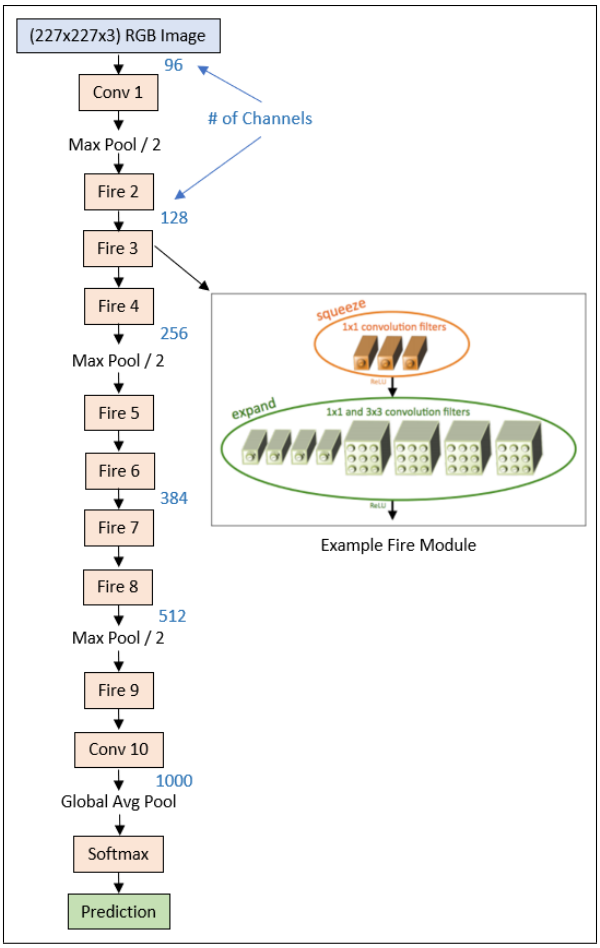

Figure 6.3: SqueezeNet architecture is shown along with detail of an example Fire module [39]

The primary building blocks of SqueezeNet are Fire modules which minimize the number of parameters required to be solved during training [39]. The implementation costs of SqueezeNet is approximately 5 MB for parameter storage and approximately 360 MFLOP per prediction. In this thesis, a CNN model is developed by modifying the SqueezeNet model and removing additional convolutional layers to further reduce its computation costs. Grayscale spectrograms are used in place of RGB images, and the number of output channels is reduced to the number of classes. Layers are removed until the resulting model achieves a training accuracy greater than 90% for the set of 7 classes detailed in Table 6.1. The resulting CNN model architecture is shown in Figure 6.4.

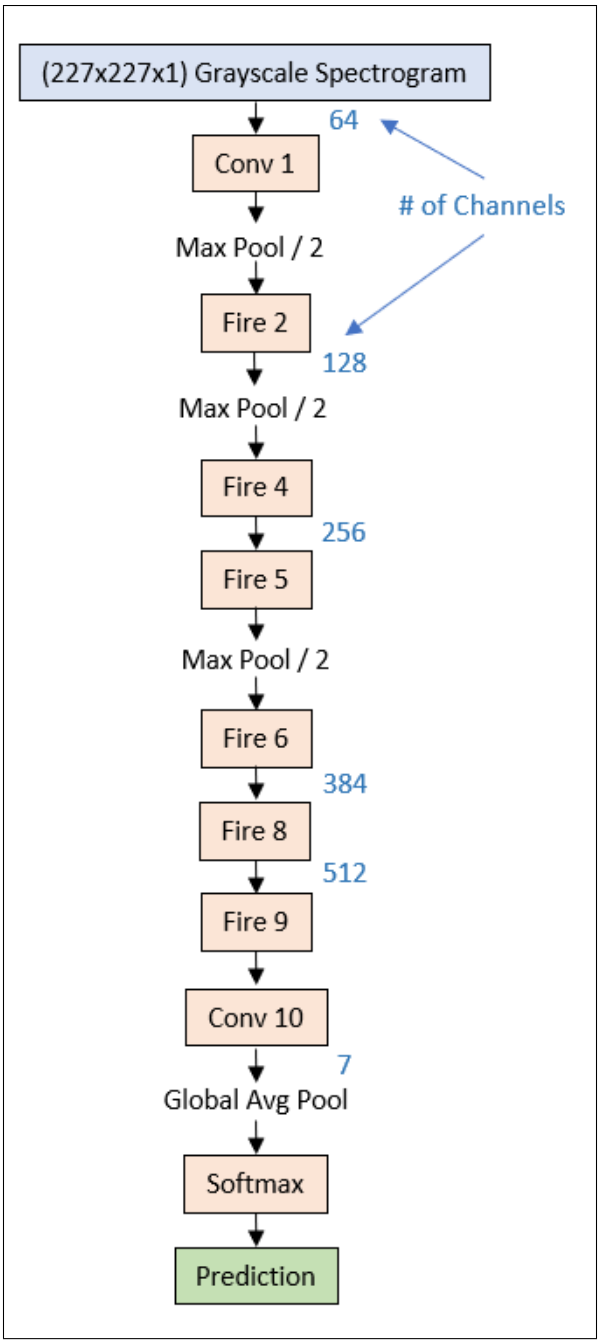

Figure 6.4: A custom CNN architecture is derived from SqueezeNet to further reduce computation costs while achieving high accuracy for this specific application.

The resulting architecture requires approximately 2.3 MB of parameter storage and approximately 280 MFLOP per prediction. This is a reduction of approximately 80 MFLOP per prediction.

6.2.3 CNN Model Training

A total of 2835 TFIs were generated, 405 TFIs per class, to train and test the CNN model. To increase the CNN model's robustness, the pulse SNR was varied following a Gaussian distribution with 30 dB mean and 10 dB variance, and the pulse location within the PRI was varied following a uniform distribution. Of the 2835 TFI's, 80% was used as the training set, 10% was used as the test set, and 10% was used as the verification set. Stochastic gradient descent with momentum was used to train the CNN with an initial learning rate of 0.001, batch size of 128, 5 epochs, and a 60% dropout. The resulting confusion matrix, which details the accuracy of the trained CNN model, is shown in Figure 6.5.

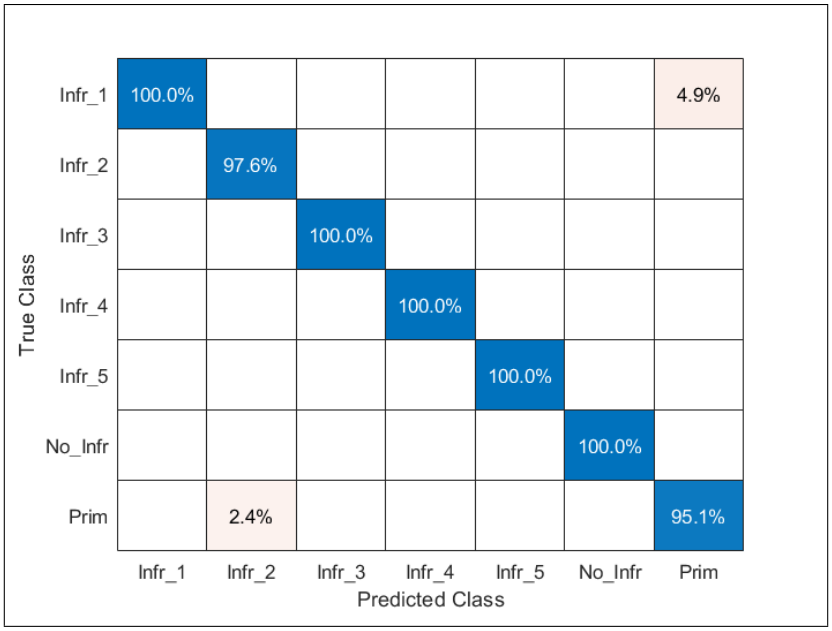

Figure 6.5: Confusion matrix for the trained custom CNN is shown.

As observed in Figure 6.5, the overall accuracy is 99% and the greatest confusion occurs between the primary waveform and the interference type 1. The accuracy of the CNN model is expected to decrease as the SNR of the pulse decreases. This effect is investigated in [40] and [35], but is not discussed within this thesis. As a result, this algorithm is only evaluated for interference with INR greater than 30 dB within this thesis.

6.3 M-SLC

The following subsections provide a detailed approach and example for incorporating spectrograms and CNNs with SLC.

6.3.1 M-SLC Application Steps

Once a CNN model is trained, the proposed steps to perform machine learning with sidelobe cancellation (M-SLC) are as follows:

1. Compute the spectrogram for each PRI in the post-MTI output CPI of a single auxiliary element, $\boldsymbol{a}_1$
    - Spectrogram parameters must be equivalent to those used to train the CNN
    - Target SNR on auxiliary element is lower than than on the main array
2. Use the trained CNN to obtain a prediction for each spectrogram. Denote N_I as the number of unique interference classes predicted over all spectrograms.
3. For each of the N_I interference classes identified in step 2:
    (a) Generate a replica of the interference pulse, $\boldsymbol{i}_B$, with length denoted by N_{τ_I}
    (b) Perform matched filtering between $\boldsymbol{i}_B$ and $\boldsymbol{a}_1$ to obtain $\mathbf{out}_{mf}$,
        - $\mathbf{out}_{mf}[k] = \sum_{n=0}^{N_{\tau_I}-1} \boldsymbol{i}_B^{\star}[n]\boldsymbol{a}_1[k+n]$
    (c) Compute a threshold as $thresh = \max_k \left(\mathbf{out}_{mf}[k]\right) - \epsilon$
    (d) Denote $\boldsymbol{p}$ as the $N_p \times 1$ vector containing all indices within $\mathbf{out}_{mf}$ that exceed $thresh$,
        - $\boldsymbol{p}[i] = \{p : \ \mathbf{out}_{mf}[p] > thresh\}$
        - $\boldsymbol{p}$ contains indices corresponding to the leading edge of interfering pulses within $\boldsymbol{a}_1$

(e) Identify the set of samples containing interference, $\boldsymbol{s}$, as

- $\boldsymbol{s}[i] = \{s : \ s \in \boldsymbol{a}_1[p_i : p_i + N_{\tau_I} - 1], \quad \text{for } i = 0, \ldots, N_p - 1\}$

(f) Randomly select $\frac{L}{N_I}$ samples from $\boldsymbol{s}$ to estimate interference

4. Perform SLC as detailed in section 3.4 using the L samples identified in step 3

Selection of ϵ

Selecting ϵ when computing $thresh = \max_k(\mathbf{out}_m f[k]) - \epsilon$ can allow precise estimation of interference while avoiding undesired signal samples (i.e. target samples) under certain conditions. Denote the cross-correlation between two waveforms, $x_1(t)$ and $x_2(t)$ as

$$R_{x_1,x_2}(m) = \mathbf{E}\{x_1(t+m)x_2^{\star}(t)\}. \tag{6.2}$$

Consider the following two conditions:

1. No overlap in time between distinct waveforms
2. Maximum cross-correlation between any pair of distinct waveforms is lower than the minimum autocorrelation of any waveform,

$$\max_{m,j\neq i}\left(R_{x_i,x_j}(m)\right) < \min_i \max_m \left(R_{x_i,x_i}(m)\right) \tag{6.3}$$

If these two conditions are satisfied, then there exists an ϵ so that signal samples not intended to be estimated are not selected, and the target constraint can be dropped. This adds back a DOF and results in the capability to suppress an additional interferer. Equivalently, this ϵ can be chosen as

$$0 \leq \epsilon \leq \min_i \max_m \left(R_{x_i,x_i}(m)\right) - \max_{m,j\neq i}\left(R_{x_i,x_j}(m)\right). \tag{6.4}$$

However, in practice, these are not guaranteed assumptions since waveforms may still overlap with high cross-correlation.

M-SLC Benefits

Certain implementation benefits of M-SLC are best realized by comparison to an alternate method. Consider the method proposed in [30] which involves iteratively matched filtering the replica of each interference pulse with the output CPI to identify all samples of interference for direct removal. One drawback of this method is the required knowledge of expected amplitude levels in the matched filtered output to derive a decision threshold. Each interference may not be present within the CPI which makes identifying a decision threshold difficult. Secondly, when using the direct removal method, all interference samples within the CPI must be identified to prevent interference artifacts within the resulting RDM.

Alternatively, the M-SLC does not require knowledge of absolute amplitude levels within the CPI, as the CNN identifies the presence of interference by analyzing the structure of the spectrogram. Additionally, interference suppression via SLC does not require identification of every interference sample, but only a set of samples to estimate the spatial interference statistics.

Additionally, M-SLC can also provide an estimate of the interference PRI $\hat{T}_I$ and pulse count $\hat{M}_I$. When $\boldsymbol{p}$ from step 3d is unique and sequential in time,

$$\hat{T}_I = \text{mode}(\boldsymbol{d}), \text{ where } d_i = \boldsymbol{p}[i+1] - \boldsymbol{p}[i] \text{ for } i = 0, \ldots, N_p - 1 \tag{6.5}$$

and

$$\hat{M}_I = \frac{\boldsymbol{p}[N_p - 1] - \boldsymbol{p}[0]}{\hat{T}_I}. \tag{6.6}$$

This provides the users of the primary radar system additional information of the interference waveform parameters.

6.3.2 M-SLC Application Example

Consider the scenario in Figure 4.2 where interference from a co-located radar is in a sidelobe of the primary radar's main array pattern. The target SNR is -10 dB and the interference INR is 50 dB. However, now the set of all interference waveform pulses is known, and interference type 1 from Table 6.1 is the modeled interference waveform.

Performing M-SLC begins with computing the spectrogram for each PRI of the post-MTI output for a single auxiliary element. The spectrogram parameters match those used to train the CNN model. An example of the output CPI is shown in Figure 6.6.

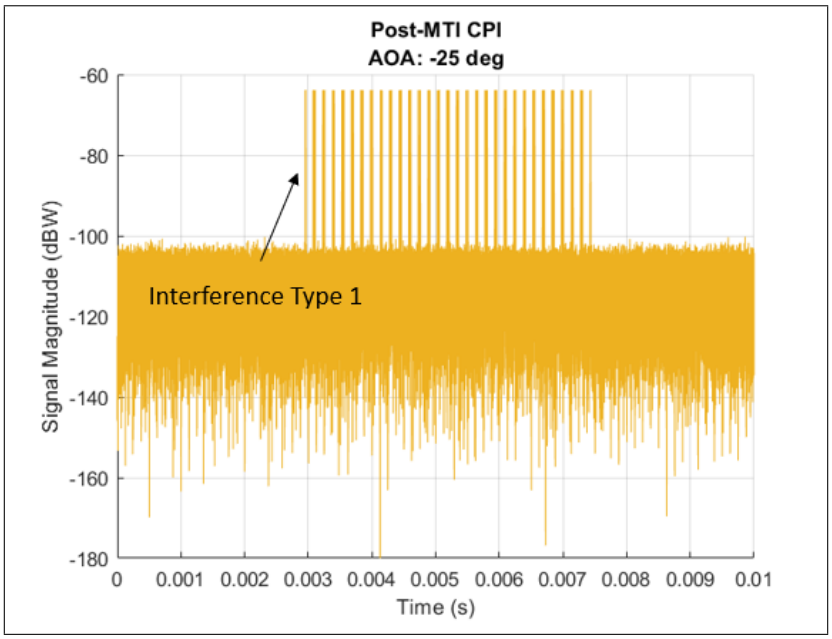

Figure 6.6: Post-MTI output CPI for a single auxiliary element is shown. Interference type 1 from Table 6.1 is present.

As observed in Figure 6.6, the dominant component within each PRI is either noise or interference. The spectrograms for example PRIs containing primarily noise or interference is shown in Figure 6.7.

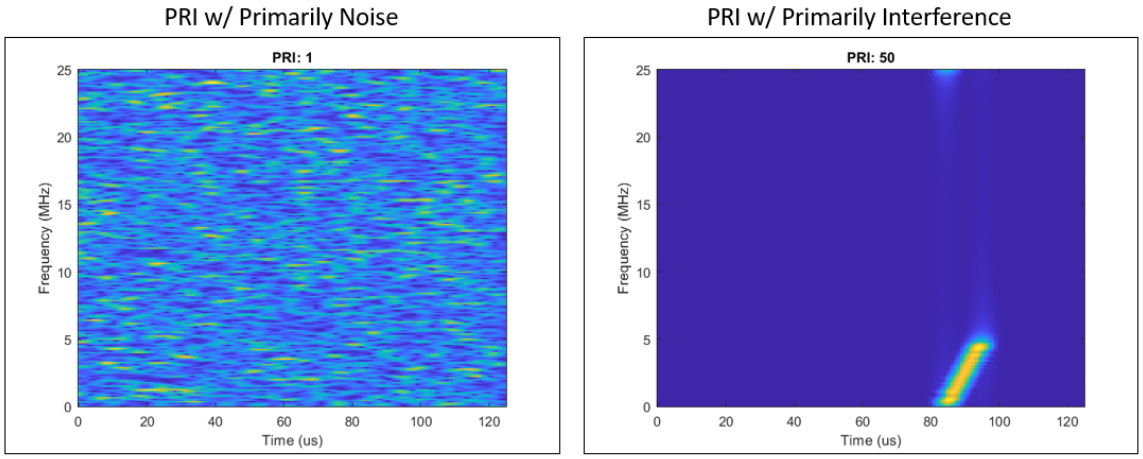

Figure 6.7: Example spectrograms of PRIs containing primarily noise (left) or interference type 1 (right) is shown.

In this example, the number of PRIs is $M = 80$. Each of the 80 spectrograms are fed into the trained CNN model and 80 predictions are obtained. The percentage of each waveform type predicted over all PRIs is shown in Table 6.2.

Table 6.2: The predicted percentages for each waveform type over all $M = 80$ PRIs is shown.

Interference 1	Interference 2	Interference 3	Interference 4	Interference 5	Noise	Primary
45%	0%	0%	0%	0%	55%	0%

These percentages match what is visually observed in Figure 6.6 where approximately 45% of the CPI contains interference and the remainder of the CPI is dominated by noise. In this example, only interference type 1 is present so a replica of this waveform pulse is generated and match filtered with the output CPI. The resulting match filtered output is shown in Figure 6.8.

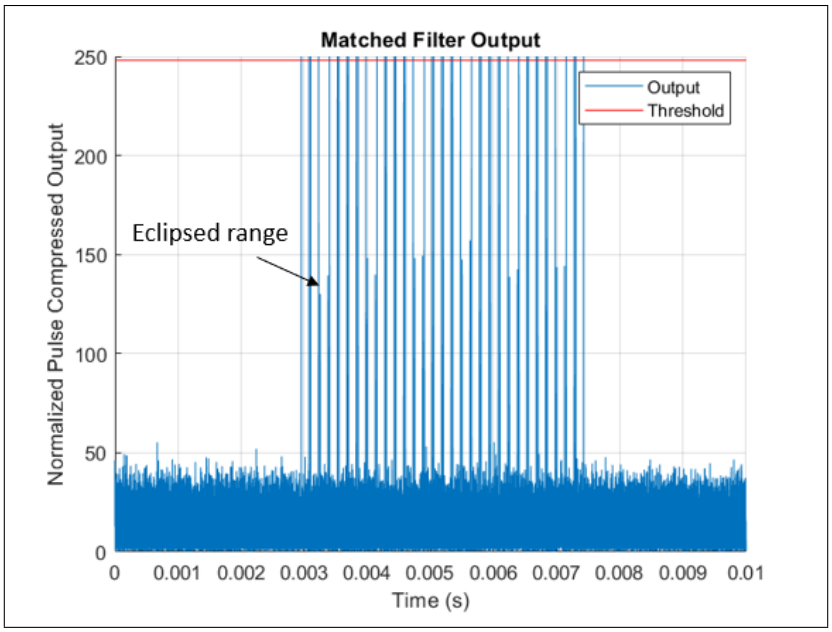

Figure 6.8: Match filtered output for machine learning example is shown. Interference type 1 is identified and replica is match filtered with output CPI.

In this example, the output CPI is amplitude normalized and $\epsilon = 2$. Comparing Figure 6.8 to Figure 6.6, it is observed that time indices exceeding the threshold in the matched filter output correspond to the leading edge of the interference pulse within the CPI. Along with the a-priori knowledge of the interference pulse width, the exact samples of interference pulses are identified. Note that reduced matched filter gain occurs when the interference pulse is partially within the eclipsed range. $L = 60$ samples are randomly selected from the identified samples, and these samples are shown overlaid on the output CPI in Figure 6.9.

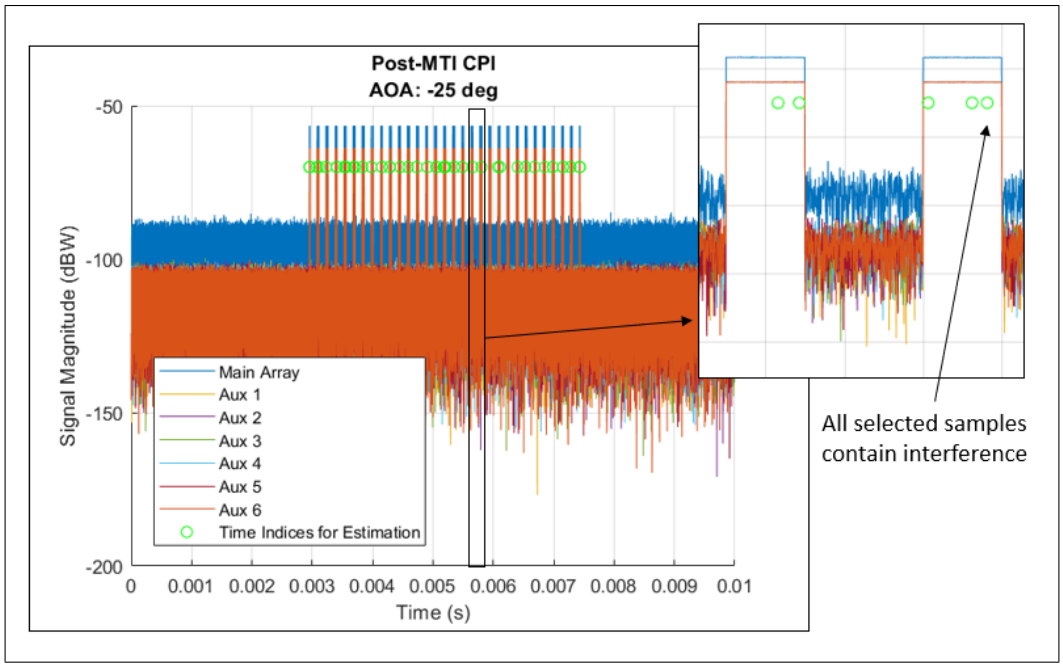

Figure 6.9: The output CPI is shown for the main array and each auxiliary element. Interference type 1 is observable, and the samples selected via M-SLC are indicated by green circles.

As observed in Figure 6.9, all $L = 60$ selected samples contain interference, and these samples are used to perform SLC as detailed in section 3.4. The resulting effective antenna pattern is shown in Figure 6.10.

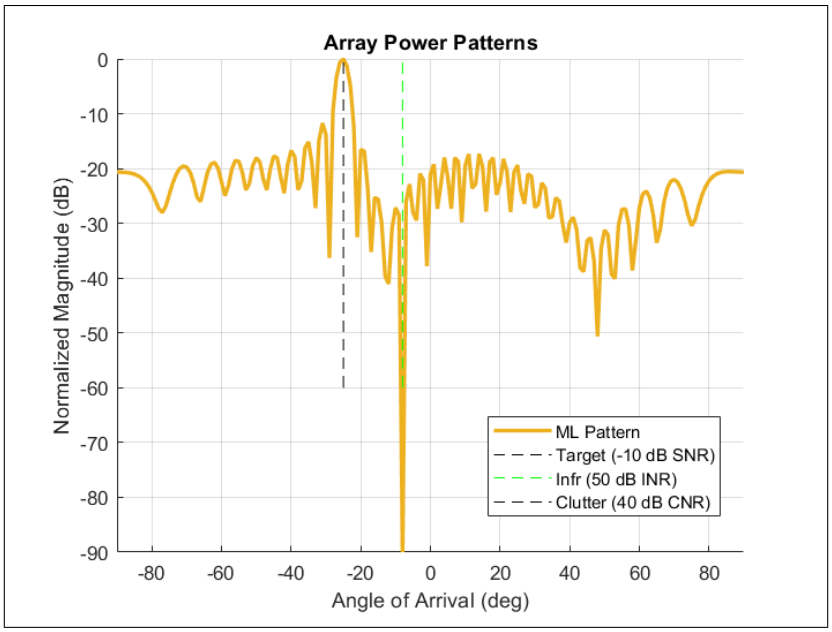

Figure 6.10: Post M-SLC antenna pattern is shown. A notch is formed in the direction of the interference.

As observed in Figure 6.10, a notch is formed in the direction of the interference. The resulting RDM is shown in Figure 6.11.

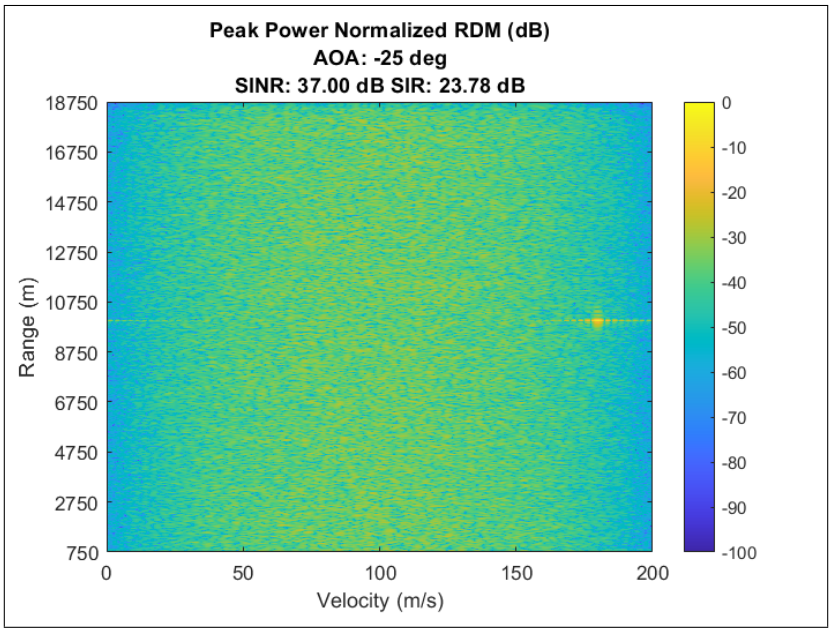

Figure 6.11: Post M-SLC RDM is shown. The SINR is recovered and the target is clearly observable.

The resulting SINR is recovered when compared to Figure 4.7 and the target is clearly observable. Comparison of the machine learning method to methods discussed earlier in this thesis is shown in Table 6.3.

Table 6.3: The performance and computation costs are compared for the machine learning method. Performance is measured over 30 simulations.

Method	Mean SINR (dB)	Min SINR (dB)	Var SINR (dB)	FLOP
Random Selection (L=60)	36.17	10.28	41.44	5 k
Entire CPI	37.19	37.11	0.00	21 M
C-SLC (L=60)	36.89	36.68	0.02	2.5 M
M-SLC (L=60)	36.92	36.72	0.01	22 G

The machine learning method only achieves marginally better performance than the correlation method but with much higher computation costs. The primary cost of the machine learning method is the prediction for a single spectrogram (approximately 280 MFLOP) which must be performed for each PRI. However, as the number of samples used to estimate interference, L, decreases, then the improvement of the machine learning method over the correlation method increases. The machine learning method is able to concentrate a greater percentage of allotted samples on interference. This is depicted in Figure 6.12.

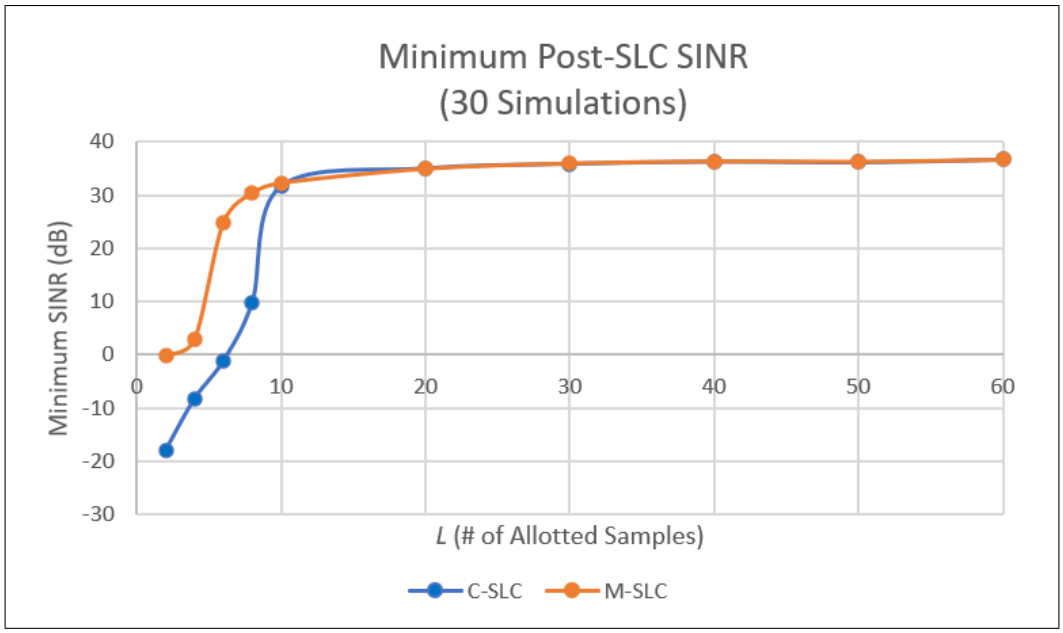

Figure 6.12: The performance of M-SLC and C-SLC are plotted versus number of samples allotted to estimate interference.

This thesis has proposed two methods, C-SLC and M-SLC, to improve robustness of the interference estimation for SLC suppression of a single co-located radar. In the next chapter, an iterative method is proposed to suppress a combination of multiple white noise jammers and co-located radar interference.

CHAPTER 7

ITERATIVE SIDELOBE CANCELLATION

The scenarios evaluated thus far have only included the existence of either a single non-stationary or stationary time interference source. When multiple interference sources are present within the primary radar environment, effective suppression to recover the target SINR becomes more difficult. This chapter proposes an iterative SLC algorithm utilizing the correlation and machine learning estimation methods detailed in Chapter 5 and Chapter 6.

7.1 Multiple Interference Effects

Consider the scenario shown in Figure 1.1 and Figure 7.1 where multiple interference sources are present within the primary radar environment. The location and power of the interference sources are indicated on the main array's antenna pattern.

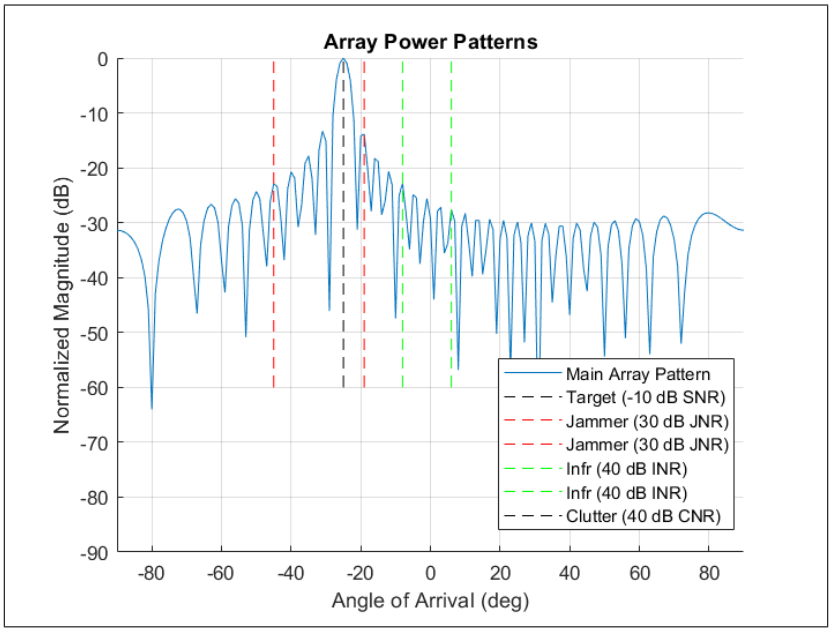

Figure 7.1: The location and power of multiple interference sources are indicated on the main array's antenna pattern.

As discussed throughout this thesis, suppression of interference requires an estimate of its spatial statistics. This requires that samples containing each interference are identified. C-SLC and M-SLC application examples are given in Chapter 5 and 6 for adaptively identifying interference samples in a single interference environment. However, interference estimation becomes more difficult when multiple interference sources are present. White noise jammers can mask the presence of other interference, such as co-located radars. The output CPIs for two auxiliary elements for the scenario depicted in Figure 7.1 is shown in Figure 7.2.

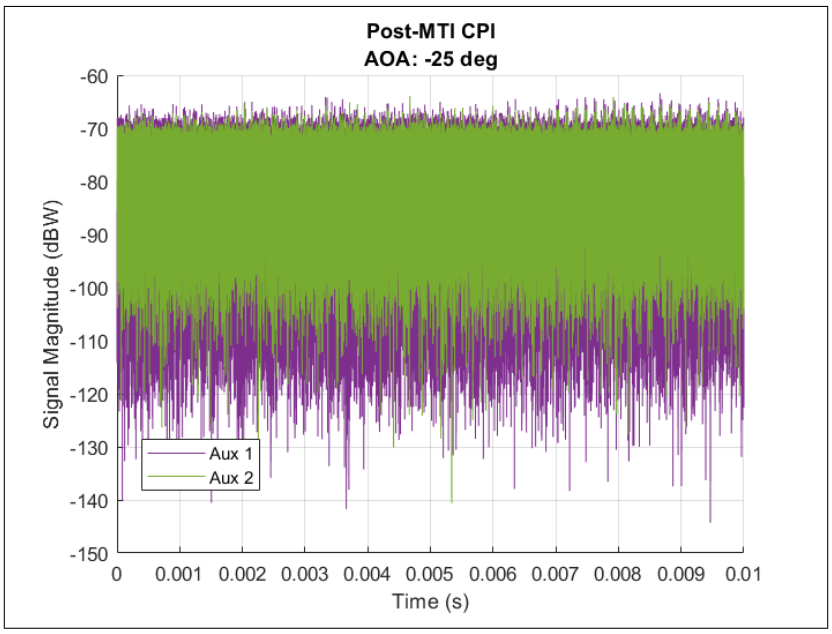

Figure 7.2: Post-MTI output CPIs for two auxiliary element is shown for the scenario in Figure 7.1. Multiple interference sources are modeled.

As observed, spatially correlated white noise jammers are the dominant signal throughout the entire CPI. If using C-SLC to identify interference samples, then all samples with the CPI correspond to high correlation as shown in Figure 7.3, and selecting a set of samples which contain both the white noise jammer and pulsed interference from co-located radars is random chance.

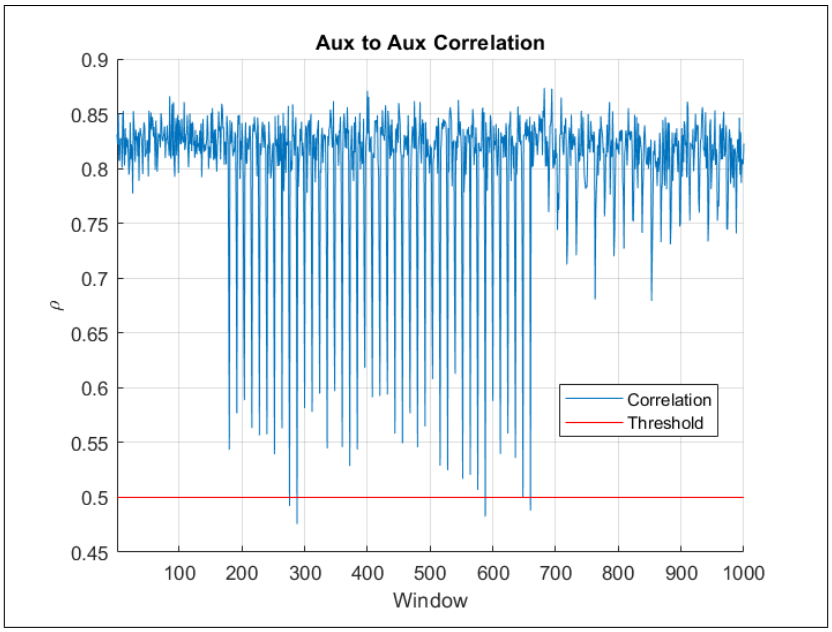

Figure 7.3: The computed correlation across the CPI between two auxiliary elements is shown for the multiple interference scenario in Figure 7.2.

Using the C-SLC algorithm results in poor performance as indicated by an SINR variance of 30.48 dB over 30 simulations, detailed in Table 7.2. The output CPI after C-SLC processing is shown in Figure 7.4. It is observed that the white noise jammer is suppressed but the co-located radar interference remains.

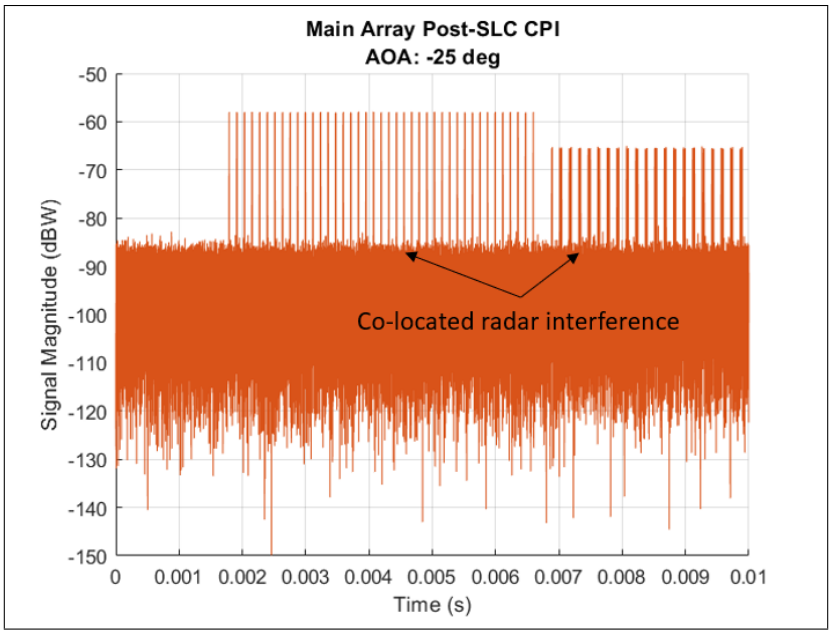

Figure 7.4: Post C-SLC output CPI is shown for the scenario with multiple interference sources. The white noise jammer is suppressed, but the co-located radar interference remains.

Additionally, if the M-SLC algorithm is used, the white noise jammer dominates the spectrograms resulting in corrupted predictions. Noise is often the only predicted waveform type in this scenario, so SLC is not attempted. Therefore, more robust methods are required which are discussed in the following sections.

7.2 Iterative Solution

An iterative solution is proposed to identify samples containing both stationary and non-stationary interference. A detailed approach and example is given in the following subsections.

7.2.1 IC-SLC Application Steps

As in Chapter 3, let $\boldsymbol{A}$ be the $N_S \times N_{Aux}$ matrix containing the sampled output CPI for each auxiliary element. Represent the sampled output CPI of a single auxiliary element as $\boldsymbol{a}_1 = \boldsymbol{A}[:, 1]$ and the sample output CPI of the remaining auxiliary elements as

$\boldsymbol{A}_r = \boldsymbol{A}[:, 2 : N_{Aux}]$. The proposed steps to perform iterative correlation with sidelobe cancellation (IC-SLC) are as follows:

1. Split the post-MTI output CPI for two auxiliary elements into smaller windows of time

2. Compute correlation between the two auxiliary elements for each window per Equation 5.2

3. Randomly select L samples from windows that exceed a specified correlation threshold, ρ_{thresh}

    - If no correlation exceeds ρ_{thresh}, then perform no SLC

4. Perform the first pass of SLC as detailed in section 3.4 with $N_{Aux} - 1$ auxiliary elements evaluated at a proportion of the L samples, $L_1 < L$. Do this for both the main array output, $\boldsymbol{y}$, and a single auxiliary element output, $\boldsymbol{a}_1$,

    - $\hat{\boldsymbol{y}}_1 = \boldsymbol{y} - \boldsymbol{A}_r\hat{\boldsymbol{w}}_y$, $\hat{\boldsymbol{w}}_y = \text{argmin}_{\boldsymbol{w}_y}\|\boldsymbol{y} - \boldsymbol{A}_r\boldsymbol{w}_y\|_2^2$ s.t. $\boldsymbol{C}\boldsymbol{w}_y = \boldsymbol{0}$
    - $\hat{\boldsymbol{a}}_1 = \boldsymbol{a}_1 - \boldsymbol{A}_r\hat{\boldsymbol{w}}_a$, $\hat{\boldsymbol{w}}_a = \text{argmin}_{\boldsymbol{w}_a}\|\boldsymbol{a}_1 - \boldsymbol{A}_r\boldsymbol{w}_a\|_2^2$ s.t. $\boldsymbol{C}\boldsymbol{w}_a = \boldsymbol{0}$

5. Repeat steps 1-3, except between $\hat{\boldsymbol{y}}_1$ and $\hat{\boldsymbol{a}}_1$, to identify $L_2 = L - L_1$ samples whose correlation exceed ρ_{thresh}

    - If max correlation is greater than ρ_{thresh}, then perform the second pass of SLC as detailed in section 3.4 on $\boldsymbol{y}$ evaluated at L samples consisting of the same L_1 and L_2 samples identified in steps 2 and 3

        – Reuse of the L_1 samples is necessary. If the L_1 samples contain non-stationary interference, then it is suppressed and not identified during step 4

- If no correlation exceeds ρ_{thresh}, then perform the second pass of SLC as detailed in section 3.4 on $\boldsymbol{y}$ evaluated at the same L samples identified in step 3

7.2.2 IM-SLC Application Steps

The application of iterative machine learning with sidelobe cancellation (IM-SLC) follows similar steps and incorporates the concepts introduced in C-SLC and M-SLC:

1. Split the post-MTI output CPI for two auxiliary elements into smaller windows of time

2. Compute correlation between the two auxiliary elements for each window per Equation 5.2

3. Randomly select L samples from windows that exceed a specified correlation threshold, ρ_{thresh}

    - If no correlation exceeds ρ_{thresh}, then perform no SLC

4. Perform the first pass of SLC as detailed in section 3.4 with $N_{Aux} - 1$ auxiliary elements evaluated at a proportion of the L samples, $L_1 < L$. Do this for only a single auxiliary element output, $\boldsymbol{a}_1$,

    - $\hat{\boldsymbol{a}}_1 = \boldsymbol{a}_1 - \boldsymbol{A}_r \hat{\boldsymbol{w}}_a$, $\hat{\boldsymbol{w}}_a = \text{argmin}_{\boldsymbol{w}_a} \|\boldsymbol{a}_1 - \boldsymbol{A}_r \boldsymbol{w}_a\|_2^2$ s.t. $\boldsymbol{C}\boldsymbol{w}_a = \boldsymbol{0}$

5. Perform M-SLC detailed in subsection 6.3.1 on $\hat{\boldsymbol{a}}_1$ to identify $L_2 = L - L_1$ samples containing interference

    - If interference samples exist, then perform the second pass of SLC as detailed in section 3.4 on $\boldsymbol{y}$ with L samples consisting of the same L_1 and L_2 samples identified in steps 2 and 3

- Reuse of the L_1 samples is necessary. If the L_1 samples contain non-stationary interference, then it is suppressed and not identified during step 4

- If no interference samples exist, then perform the second pass of SLC as detailed in section 3.4 on $\boldsymbol{y}$ evaluated at the same L samples identified in step 3

7.2.3 IC-SLC Application Example

Consider the scenario in Figure 7.1. The target SNR is -10 dB, and white noise jammers (30 dB JNR) and co-located radar interference (40 dB INR) is located in the main array's antenna pattern sidelobes.

Performing IC-SLC begins by computing the correlation between two auxiliary elements to identify $L_1 = 20$ samples from windows whose correlation exceed $\rho_{thresh} = 0.5$. The first pass of SLC is performed on the output of the main array, $\boldsymbol{y}$, and a single auxiliary element, $\boldsymbol{a}_1$, using $N_{Aux} - 1$ auxiliary elements and evaluated at the $L_1 = 20$ samples. The output CPIs after the first pass of SLC for the main array and the single auxiliary element, $\hat{\boldsymbol{y}}_1$ and $\hat{\boldsymbol{a}}_1$, is shown in Figure 7.5.

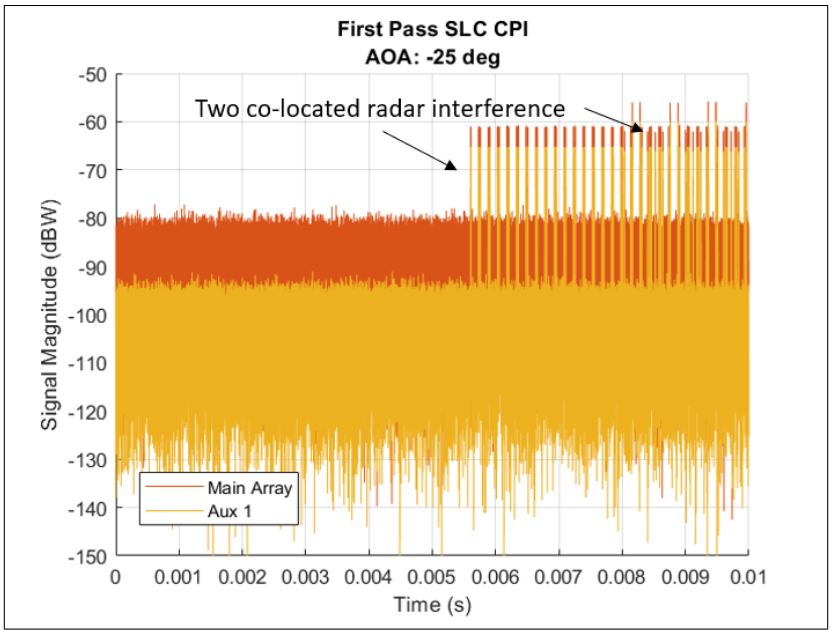

Figure 7.5: The resulting output CPIs for the main array and single auxiliary element after the first pass of IC-SLC.

As observed in Figure 7.5, the white noise jammer is suppressed leaving behind interference from two co-located radars. Next, the correlation is computed between between $\hat{\boldsymbol{y}}_1$ and $\hat{\boldsymbol{a}}_1$ to identify $L_2 = 40$ samples from windows whose correlation exceed $\rho_{thresh} = 0.5$. The second pass of SLC is then performed on $\boldsymbol{y}$ evaluated at the same L_1 and L_2 samples already identified. The resulting output CPI for the main array after the second pass of SLC is shown in Figure 7.6 overlaid with the output CPIs after just MTI processing and first pass SLC.

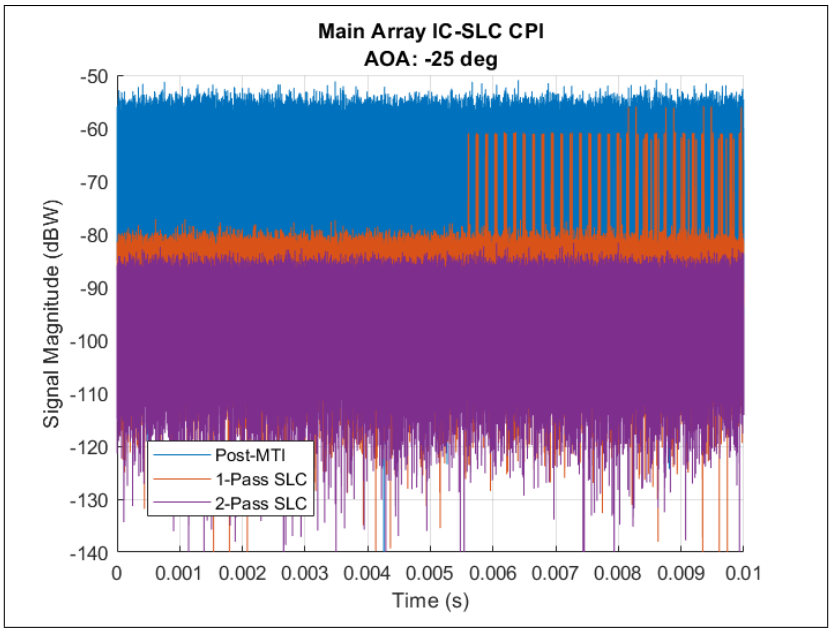

Figure 7.6: The resulting output CPI for the main array after the second pass of IC-SLC. The output CPIs after MTI processing and first pass SLC are also shown to show progression in suppression.

The progression in suppression of the interference is observable in Figure 7.6. The resulting effective antenna pattern is shown in Figure 7.7.

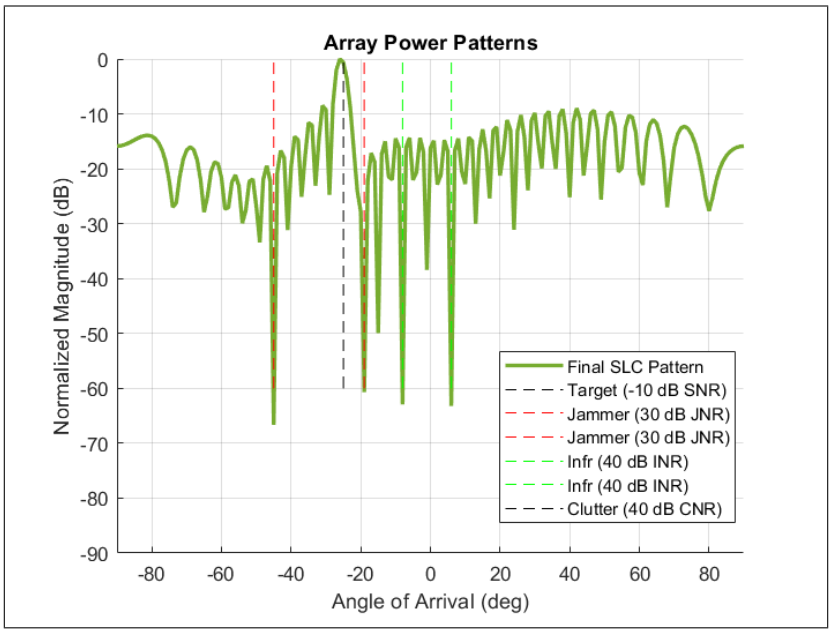

Figure 7.7: Post IC-SLC is shown. Notches are formed in the directions of interference.

As observed in Figure 7.7, notches are formed in the directions of interference. The resulting RDM is shown in Figure 7.8.

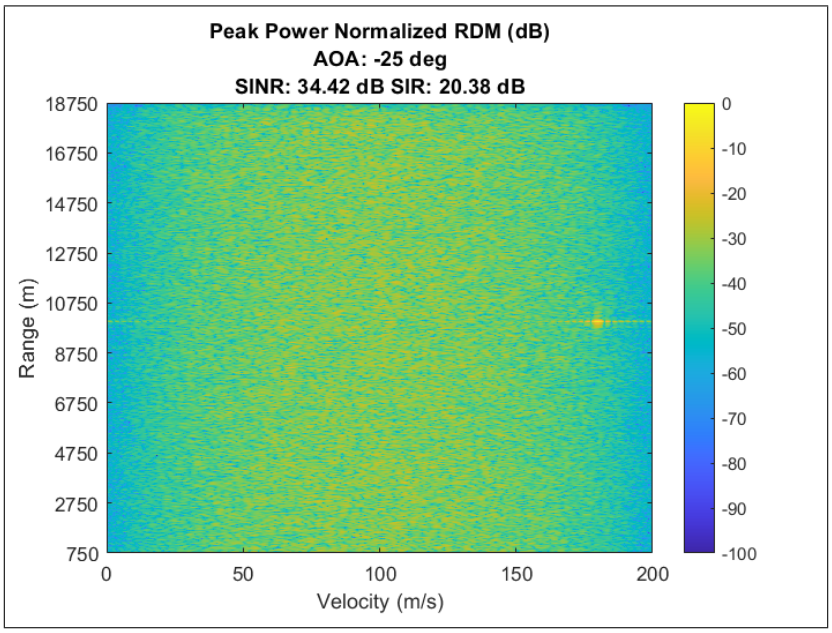

Figure 7.8: Post IC-SLC RDM is shown. The SINR is recovered and the target is clearly observable.

The resulting SINR is recovered and the target is clearly observable.

7.2.4 IM-SLC Example

Consider the same scenario as in Figure 7.1. Performing IM-SLC begins by computing the correlation between two auxiliary elements to identify $L_1 = 20$ samples from windows whose correlation exceed $\rho_{thresh} = 0.5$. The first pass of SLC is performed on the output of a single auxiliary element, $\boldsymbol{a}_1$, using $N_{Aux} - 1$ auxiliary elements and evaluated at the $L_1 = 20$ samples. The output CPI after the first pass of SLC for the single auxiliary element, $\hat{\boldsymbol{a}}_1$, is shown in Figure 7.9.

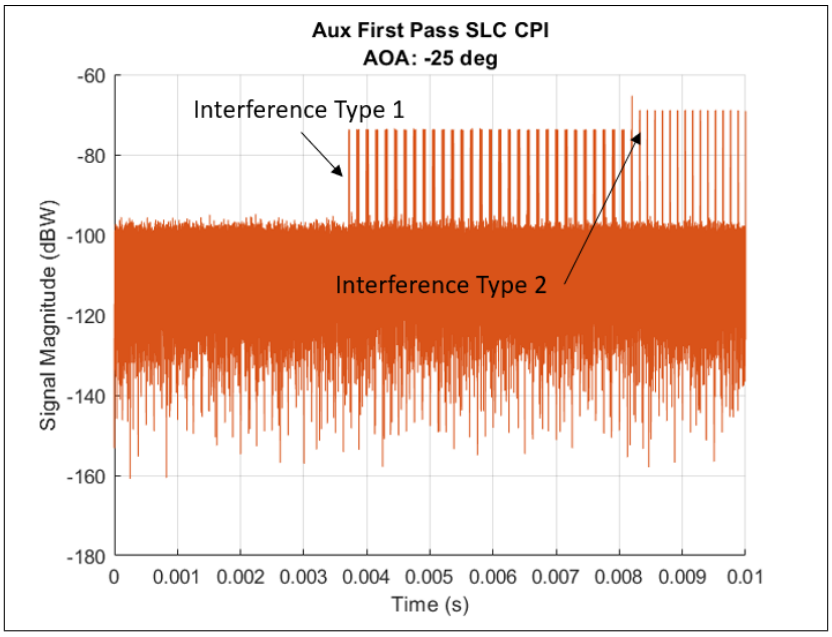

Figure 7.9: The resulting output CPI for a single auxiliary element after the first pass of IM-SLC.

The M-SLC algorithm detailed in subsection 6.3.1 is applied to the output CPI, $\hat{\boldsymbol{a}}_1$, in Figure 7.9. The resulting predictions are shown in Table 7.1.

Table 7.1: The predicted percentages for each waveform type over all $M = 80$ PRIs is shown for the IM-SLC example.

Interference 1	Interference 2	Interference 3	Interference 4	Interference 5	Noise	Primary
45.0%	17.5%	0%	0%	0%	37.5%	0%

As shown in Table 7.1, only interference type 1 and interference type 2 are predicted to occur within the CPI which aligns with what is observed in Figure 7.9. Continuing ML-SLC detailed in subsection 6.3.1, a set of $L_2 = 40$ samples are identified which contains both interference type 1 and interference type 2. The second pass of SLC is then performed on $\boldsymbol{y}$ using the same L_1 and L_2 samples already identified. The resulting effective antenna pattern is shown in Figure 7.10.

Figure 7.10: Post IM-SLC antenna pattern is shown. Notches are formed in the directions of interference.

As observed in Figure 7.7, notches are formed in the directions of interference. The resulting RDM is shown in Figure 7.11.

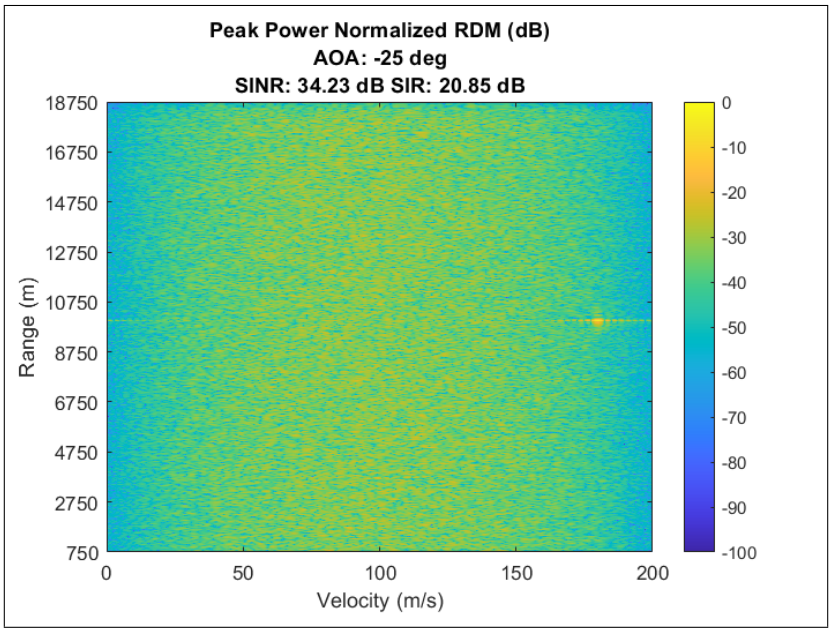

Figure 7.11: Post IM-SLC RDM is shown. The SINR is recovered and the target is clearly observable.

The resulting SINR is recovered and the target is clearly observable.

7.3 Algorithm Comparison

Comparison of IC-SLC and IM-SLC to algorithms discussed earlier in this thesis is shown in Table 7.2 for the scenario in Figure 7.1.

Table 7.2: The performance and computation cost comparison of algorithms presented in this thesis are detailed for the multiple interference scenario in Figure 7.1. Performance is measured over 30 simulations.

Method	Mean SINR (dB)	Min SINR (dB)	Var SINR (dB)	FLOP
Entire CPI	34.65	34.51	0.00	21 M
C-SLC (L=60)	33.04	12.19	30.48	2.5 M
M-SLC (L=60)	32.14	4.68	133	22 G
IC-SLC (L=60)	34.23	33.29	0.08	5 M
IM-SLC (L=60)	34.08	32.79	0.17	22 G

As expected, the performance of the iterative algorithms exceed that of C-SLC and M-SLC. The performance of M-SLC is noticeably lower due to corrupted predictions of noisy spectrograms. C-SLC only consistently identify samples containing white noise jamming, and only by chance does it also identify samples containing co-located radar interference. The iterative algorithms consistently identify a set of samples containing all interference within the primary radar CPI.

Both iterative algorithms achieve similar performance, IC-SLC requires less computation than IM-SLC or using the entire CPI. However, a weakness of both IC-SLC and IM-SLC occurs when a degraded estimate of co-located radar interference is made during the first pass of SLC that does not suppress the interference below the noise floor. This occurs by chance when the first L_1 samples contain a limited estimation of the co-located radar interference. As a result, the interference INR may be low enough during the second pass to cause low correlation between aux elements or poor prediction by M-SLC, but still high enough to cause artifacts within the resulting RDM. IC-SLC and IM-SLC performance improves when the L_1 samples do not contain co-located radar interference so that

their presence is more easily identified during the second pass.

In contrast, using the entire CPI ensures that all available samples of interference are used for its estimate. This is reflected in the performance of using the entire CPI which exceeds that of IC-SLC and IM-SLC. If the radar architecture allows for updating the estimated interference covariance matrices incrementally, then the cost using the entire CPI can be paid incrementally. This is reviewed in the next section.

7.4 Incremental Covariance Estimate

As detailed in section 3.2, the radar architecture addressed in this thesis operates by CPI block processing. The primary radar first collects an entire CPI, and then uses the data within this CPI to generate adaptive auxiliary element weights. These weights are used to suppress interference only within that specific CPI, and this process is repeated for each CPI so that each CPI generates new adaptive weights.

As shown in Table 7.2, using the entire CPI of data achieves better suppression performance than using a limited set of samples. However, the drawback is higher computation costs. The differentiating cost comes from computing the auxiliary covariance matrix which requires $2N_S N_{Aux}$ FLOP. Given the output CPIs of each auxiliary element represented by the $N_S \times N_{Aux}$ matrix $\boldsymbol{A}$, recall that the estimated interference covariance matrix using all samples is computed as follows,

$$\hat{\boldsymbol{R}}_I = \frac{1}{N_S}\boldsymbol{A}^H\boldsymbol{A} = \frac{1}{N_S}\sum_{i=1}^{N_S}\boldsymbol{A}[i,:]^H\boldsymbol{A}[i,:]. \tag{7.1}$$

If the radar system allows for time sample-by-sample updating of the estimated covariance matrix, then only incremental computations of $2N_{Aux}^2$ FLOP are required to form the interference covariance matrix using the entire CPI. However, any target signals are guaranteed to be included in the interference estimation, so a target constraint is still required to prevent suppression of high SNR targets. This reduces the number of interference sources that

can be suppressed as discussed in subsection 3.4.3.

CHAPTER 8
CONCLUSION AND FUTURE WORK

8.1 Conclusion

This thesis reviews and proposes constrained SLC algorithms for suppression of stationary and non-stationary time interference sources. SLC is an algorithm employed by subarray architectures to spatially suppress interference using an estimate of the interference covariance matrices across array sensors. Non-stationary time sources make estimating its statistics more challenging, and co-located radar systems operating by pulse-burst LFM waveforms appear as non-stationary interference to the primary radar.

In this thesis, several algorithms are proposed to adaptively identify interference samples to improve robustness of the interference estimation. C-SLC applies the concepts proposed in [5] to identify interference samples by measuring the correlation between sensors. This thesis expands on this method by providing analysis of the expected correlation between individual auxiliary elements for various target SINR scenarios. The analysis shows that computing the correlation between auxiliary elements instead of a main array reduces sensitivity to target SNR, which helps to prevent including target samples in the interference estimate. IC-SLC is proposed to iteratively apply the methods in C-SLC to suppress interference in an environment containing multiple white noise jammers and co-located radars. Additionally, both C-SLC and IC-SLC have the potential to provide computational savings versus using the entire CPI to estimate the interference statistics.

This thesis also introduces the M-SLC algorithm which is shown to improve performance in certain scenarios by concentrating a larger number of allotted estimation samples on interference. M-SLC requires that the set of interference waveform pulses is known, and M-SLC incorporates the concepts proposed in [6] to classify interference by use of

TFIs and CNNs. IM-SLC is proposed to iteratively apply the methods in C-SLC and M-SLC to suppress interference in an environment containing multiple white noise jammers and co-located radars. M-SLC and IM-SLC can also provide knowledge of the interfering waveforms by estimating the PRI and pulse count. However, these algorithms are more computationally costly than using the entire CPI.

8.2 Future Work

There is further opportunity to investigate the effects of waveform correlation on the performance of algorithms proposed in this thesis. When there is low correlation between the primary radar waveform and interference waveforms, it may be possible to drop the target constraint when applying the C-SLC and M-SLC method. This frees a DOF and provides the capability to suppress an additional interference source. This may improve the performance of C-SLC and M-SLC beyond that of using the entire CPI.

Further investigation is possible to characterize how decreasing the INR and increasing the number of waveform classes can effect the performance of M-SLC. Research in [40] and [35] shows that decreasing a waveform's SNR reduces the accuracy of its prediction by a CNN model. Within this thesis, M-SLC is evaluated for INR scenarios of approximately 30 dB or greater.

The proposed iterative algorithms, IC-SLC and IM-SLC, can also be improved by addressing their weakness when non-stationary time interference is only partially suppressed during the first pass. Further performance characterization when varying the number of first pass versus second pass samples may provide insight into opportunities for improvement.

Appendices

APPENDIX A

POST-DOPPLER SLC

Throughout this thesis, the estimation of interference is performed in the time domain prior to Doppler processing by selecting samples within the output CPI. Certain systems may be constrained to interference estimation after Doppler processing, and both the random sampling and correlation estimation methods can be implemented post-Doppler. An example of performing random estimation and C-SLC post-Doppler for a single non-stationary interference source scenario is detailed.

Consider the scenario shown in Figure 4.2 where a single co-located radar is in the sidelobe of the main array's antenna pattern. The simulated post-MTI CPI for a single auxiliary elements is shown in Figure A.1. The CPI is reshaped to form a matrix so that each column corresponds to a single PRI.

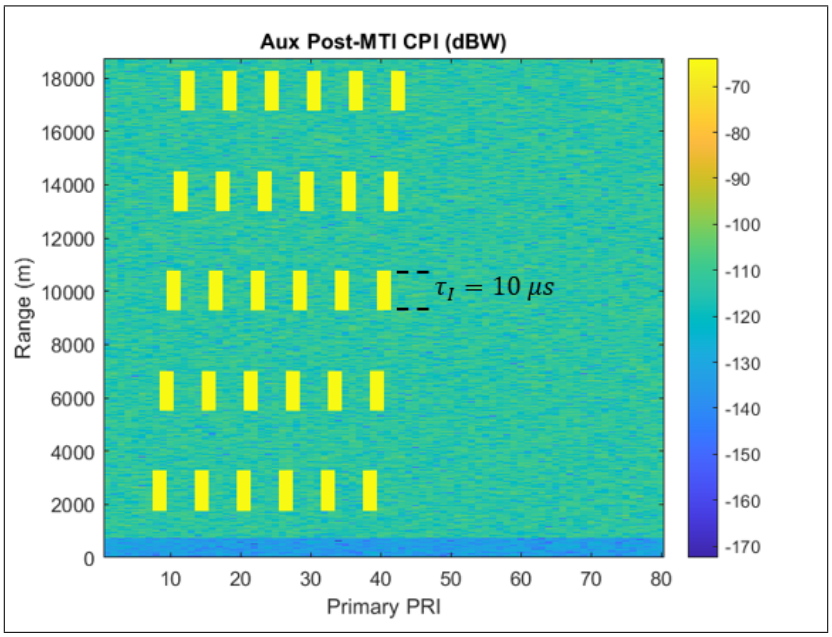

Figure A.1: Post-MTI output CPI for a single auxiliary element is shown. The effects of a single co-located radar interference source is observed.

Doppler processing is performed as detailed in subsection 2.3.2, and the resulting data matrix are shown in Figure A.2.

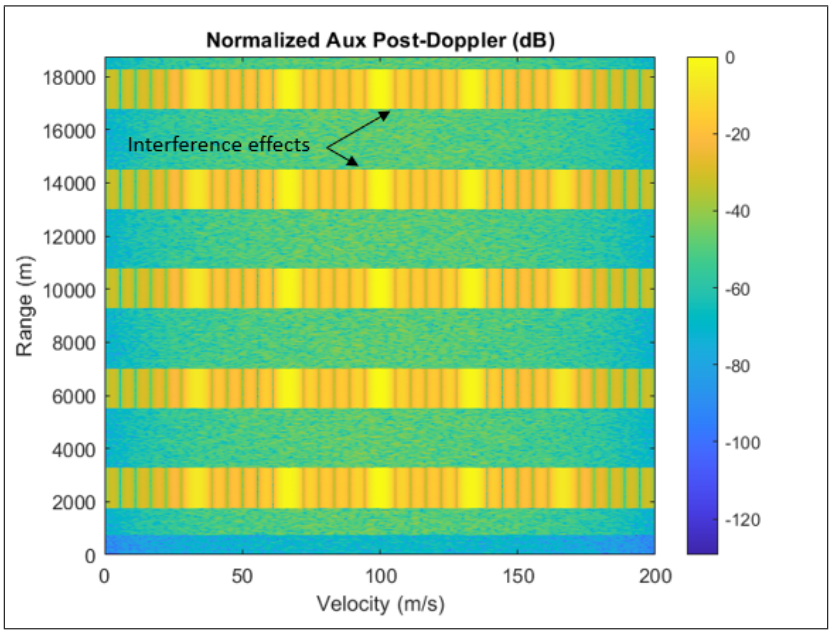

Figure A.2: The post-Doppler data matrix for a single auxiliary element is shown. The effects of a single co-located radar interference source is observed.

The structure of interference within the data matrices is reviewed in section 4.1. Estimation of the interference can be performed by selecting L samples from the post-Doppler data matrix. Example of samples selected by random sampling is shown in Figure A.3.

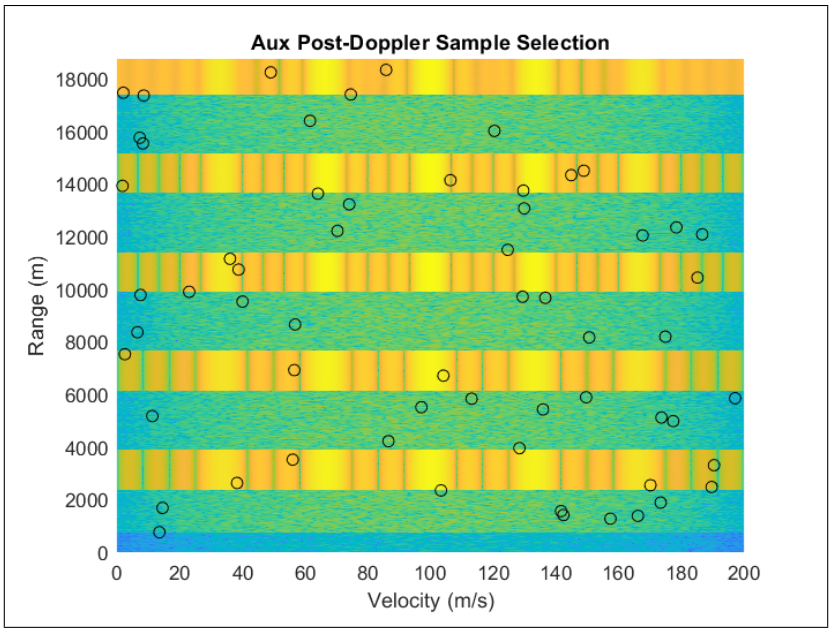

Figure A.3: The samples selected by random sampling are indicated by the black circles. Interference is not captured in all samples used.

The adaptive auxiliary weights can be computed by evaluating the least square SLC formulation detailed in Equation 3.13 at the identified post-Doppler samples. As observed in Figure A.3, interference is not captured in all samples used. Therefore, interference suppression and the post-SLC SINR is degraded. Results are shown in Table A.1.

Samples can also be selected by evaluating the Pearson correlation coefficient, per Equation 5.2, across the Doppler or range bins between two auxiliary elements. The resulting correlation between the Doppler bins, or velocities, of two auxiliary elements is shown in Figure A.4. The samples selected by this method are also shown in Figure A.4.

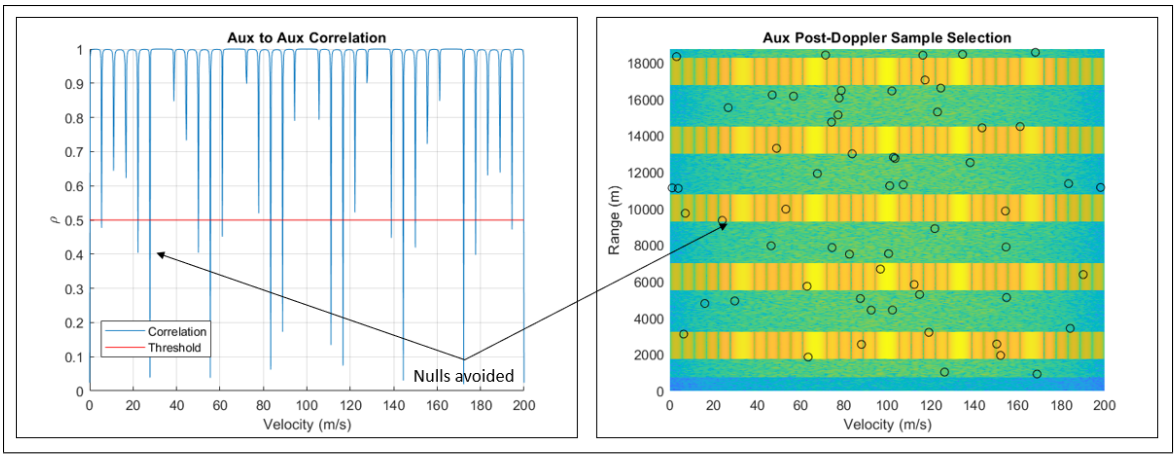

Figure A.4: The resulting correlation across Doppler bins, or velocity, between two auxiliary element is shown (left). The samples selected by Doppler correlation are indicated by the black circles (right).

Selected samples avoid the Doppler nulls below the specified correlation threshold, but interference is still not captured in all samples since there is no discrimination in range and the interference is constrained to specific bands in range. Instead, the resulting correlation between range bins of two auxiliary elements is shown in Figure A.5. The samples selected by this method are also shown in Figure A.5.

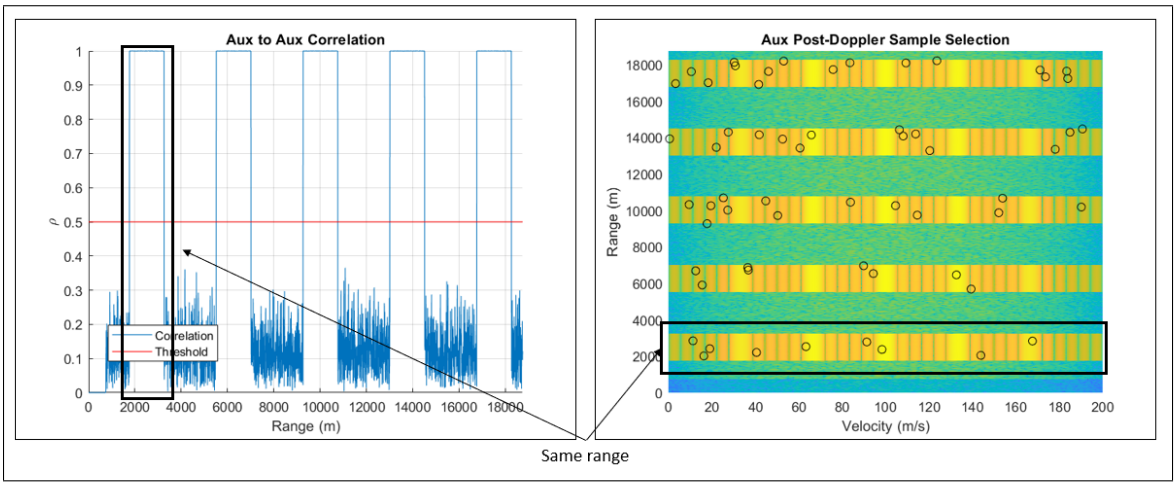

Figure A.5: The resulting correlation across range bins between two auxiliary element is shown (left). The samples selected by range correlation are indicated by the black circles (right).

Selected samples are now constrained to the range bands that the interference occupies.

However, interference is still not captured in all samples since the Doppler nulls are not avoided. Therefore, samples can also be selected by simultaneously evaluating the correlation across Doppler and range bins. Example of samples selected by both Doppler and range correlation estimation is shown in Figure A.6.

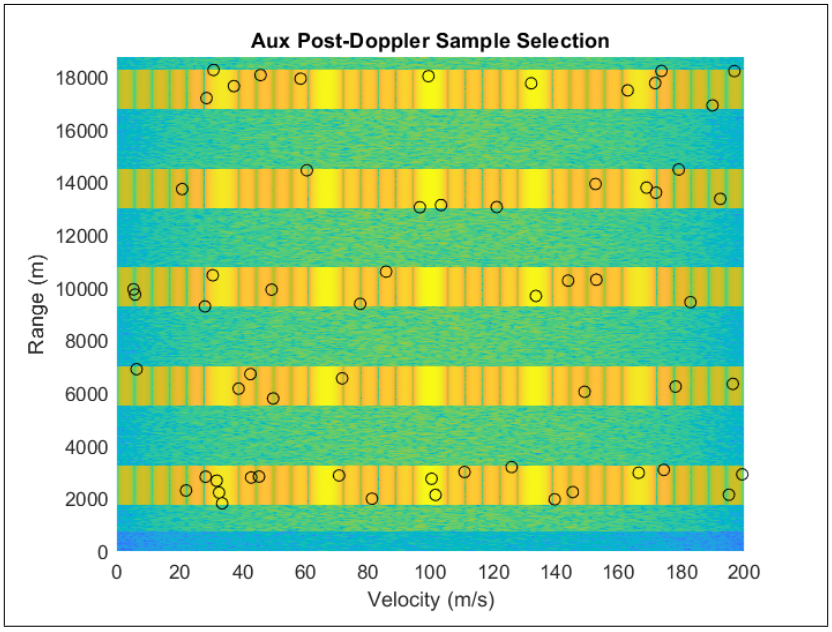

Figure A.6: The samples selected by range-Doppler correlation are indicated by the black circles.

These methods are compared to the time domain C-SLC in Table A.1. For all methods, $\rho_{thresh} = 0.5$ and $L = 60$.

Table A.1: The performance and computation costs are compared for the post-Doppler estimation methods. In all cases, $L = 60$.

Method	Mean SINR (dB)	Min SINR (dB)	Var SINR (dB)	FLOP
Time C-SLC	36.89	36.68	0.02	2.5 M
Random Post-Doppler	36.28	34.76	0.38	5 k
Doppler C-SLC	36.44	34.82	0.28	25 M
Range C-SLC	36.56	35.57	0.15	25 M
Range-Doppler C-SLC	36.63	36.10	0.06	50 M

As expected and indicated by the SINR variance, Doppler correlation estimation underperforms when compared to range and range-Doppler estimation since a smaller proportion

of the $L = 60$ samples contain interference as shown in Figure A.4. Range-Doppler estimation achieve similar performance to that of time domain estimation. In this scenario, the cost of computing the correlation after Doppler processing is higher than the cost of computing the correlation in the time domain. This is because the number of Doppler bins, 800, is greater than the number of pulses, $M = 80$. Possible techniques to reduce the cost include computing the correlation over a subsample of range or Doppler bins, but this is not discussed in this thesis.

REFERENCES

[1] M. Skolnik, *Introduction to Radar Systems*, 3rd ed. McGraw-Hill, 2001, ISBN: 9780072881387.

[2] ——, *Radar Handbook*, 2nd ed. McGraw-Hill, 1990.

[3] T. Milligan, *Modern Antenna Design*, 2nd ed. Wiley-IEEE Press, 2005.

[4] S. Applebaum, "Adaptive arrays," *IEEE Transactions on Antennas and Propagation*, vol. 24, no. 5, pp. 585–598, 1976.

[5] X. Wei, W. Yuan, and X. Zhu, "Research on suppression of slicing jamming with digital array radar," in *2016 IEEE 13th International Conference on Signal Processing (ICSP)*, 2016, pp. 1580–1584.

[6] H. Lee, Y. Largman, and A. Ng, "Unsupervised feature learning for audio classification using convolutional deep belief networks," *Advances in Neural Information Processing Systems*, vol. 22, pp. 1096–1104, 2009.

[7] R. Games, W. Eastman, and M. Sousa, "Fast algorithm and architecture for constrained adaptive side-lobe cancellation," *IEEE Transactions on Antennas and Propagation*, vol. 41, no. 5, pp. 683–686, 1993.

[8] C. A. Balanis, *Antenna Theory: Analysis and Design*, 3rd ed. Wiley-Interscience, 2005, ISBN: 0471714623.

[9] D. M. Pozar, *Microwave and Rf Design of Wireless Systems*, 1st. Wiley Publishing, 2000, ISBN: 0471322822.

[10] R. J. Mailloux, *Phased Array Antenna Handbook*, 2nd ed. Artech House, 2005, ISBN: 1580536891.

[11] D. H. Johnson and D. E. Dudgeon, *Array Signal Processing: Concepts and Techniques*. USA: Simon and Schuster, Inc., 1992, ISBN: 0130485136.

[12] C. Shannon, "Communication in the presence of noise," *Proceedings of the IRE*, vol. 37, no. 1, pp. 10–21, 1949.

[13] R. Fante, "Systems study of overlapped subarrayed scanning antennas," *IEEE Transactions on Antennas and Propagation*, vol. 28, no. 5, pp. 668–679, 1980.

[14] U. Nickel, "Subarray configurations for digital beamforming with low sidelobes and adaptive interference suppression," in *Proceedings International Radar Conference*, 1995, pp. 714–719.

[15] M. Richards, *Fundamentals of Radar Signal Processing*. McGraw-Hill, 2014, ISBN: 9780071798327.

[16] M. Cai, K. Gao, D. Nie, B. Hochwald, J. N. Laneman, H. Huang, and K. Liu, "Effect of wideband beam squint on codebook design in phased-array wireless systems," in *2016 IEEE Global Communications Conference (GLOBECOM)*, 2016, pp. 1–6.

[17] R. McAulay, "The effect of staggered prf's on mti signal detection," *IEEE Transactions on Aerospace and Electronic Systems*, vol. AES-9, no. 4, pp. 615–618, 1973.

[18] S. Haykin, *Adaptive Filter Theory*. USA: Prentice-Hall, Inc., 1986, ISBN: 0130040525.

[19] N. R. Goodman, "Statistical analysis based on a certain multivariate complex gaussian distribution (an introduction)," *The Annals of Mathematical Statistics*, vol. 34, no. 1, pp. 152–177, 1963.

[20] I. Reed, J. Mallett, and L. Brennan, "Rapid convergence rate in adaptive arrays," *IEEE Transactions on Aerospace and Electronic Systems*, vol. AES-10, no. 6, pp. 853–863, 1974.

[21] J. Ward, "Space-time adaptive processing for airborne radar," in *1995 International Conference on Acoustics, Speech, and Signal Processing*, vol. 5, 1995, 2809–2812 vol.5.

[22] A. Fenn, "Interference sources and degrees of freedom in adaptive nulling antennas," Lincoln Laboratory, Tech. Rep., 1982.

[23] X. Yang, P. Yin, T. Zeng, and T. K. Sarkar, "Applying auxiliary array to suppress mainlobe interference for ground-based radar," *IEEE Antennas and Wireless Propagation Letters*, vol. 12, pp. 433–436, 2013.

[24] L. Griffiths and C. Jim, "An alternative approach to linearly constrained adaptive beamforming," *IEEE Transactions on Antennas and Propagation*, vol. 30, no. 1, pp. 27–34, 1982.

[25] G. M. Brooker, "Mutual interference of millimeter-wave radar systems," *IEEE Transactions on Electromagnetic Compatibility*, vol. 49, no. 1, pp. 170–181, 2007.

[26] H. Deng and B. Himed, "Interference mitigation processing for spectrum-sharing between radar and wireless communications systems," *IEEE Transactions on Aerospace and Electronic Systems*, vol. 49, no. 3, pp. 1911–1919, 2013.

[27] Z. Xu and Q. Shi, "Interference mitigation for automotive radar using orthogonal noise waveforms," *IEEE Geoscience and Remote Sensing Letters*, vol. 15, no. 1, pp. 137–141, 2018.

[28] S. Blunt and K. Gerlach, "Multistatic adaptive pulse compression," *IEEE Transactions on Aerospace and Electronic Systems*, vol. 42, no. 3, pp. 891–903, 2006.

[29] S. D. Blunt and K. Gerlach, "Joint adaptive pulse compression to enable multistatic radar," in *2004 International Waveform Diversity Design Conference*, 2004, pp. 1–5.

[30] W.-Q. Wang and H. Shao, "Radar-to-radar interference suppression for distributed radar sensor networks," *Remote Sensing*, vol. 6, no. 1, pp. 740–755, 2014.

[31] J. Bechter and C. Waldschmidt, "Automotive radar interference mitigation by reconstruction and cancellation of interference component," in *2015 IEEE MTT-S International Conference on Microwaves for Intelligent Mobility (ICMIM)*, 2015, pp. 1–4.

[32] J. Mun, H. Kim, and J. Lee, "A deep learning approach for automotive radar interference mitigation," in *2018 IEEE 88th Vehicular Technology Conference (VTC-Fall)*, 2018, pp. 1–5.

[33] P. J. Kajenski, "Phase only antenna pattern notching via a semidefinite programming relaxation," *IEEE Transactions on Antennas and Propagation*, vol. 60, no. 5, pp. 2562–2565, 2012.

[34] J. Brynolfsson and M. Sandsten, "Classification of one-dimensional non-stationary signals using the wigner-ville distribution in convolutional neural networks," in *2017 25th European Signal Processing Conference (EUSIPCO)*, 2017, pp. 326–330.

[35] G. Shao, Y. Chen, and Y. Wei, "Convolutional neural network-based radar jamming signal classification with sufficient and limited samples," *IEEE Access*, vol. 8, pp. 80 588–80 598, 2020.

[36] C. Wang, J. Wang, and X. Zhang, "Automatic radar waveform recognition based on time-frequency analysis and convolutional neural network," in *2017 IEEE International Conference on Acoustics, Speech and Signal Processing (ICASSP)*, 2017, pp. 2437–2441.

[37] V. DeBrunner, M. Ozaydin, and T. Przebinda, "Resolution in time-frequency," *IEEE Transactions on Signal Processing*, vol. 47, no. 3, pp. 783–788, 1999.

[38] S. Albawi, T. A. Mohammed, and S. Al-Zawi, "Understanding of a convolutional neural network," in *2017 International Conference on Engineering and Technology (ICET)*, 2017, pp. 1–6.

[39] F. N. Iandola, S. Han, M. W. Moskewicz, K. Ashraf, W. J. Dally, and K. Keutzer, *Squeezenet: Alexnet-level accuracy with 50x fewer parameters and ¡0.5mb model size*, cite arxiv:1602.07360Comment: In ICLR Format, 2016.

[40] X. Lan, T. Wan, K. Jiang, Y. Xiong, and B. Tang, "Intelligent recognition of chirp radar deceptive jamming based on multi-pulse information fusion," *Sensors*, vol. 21, no. 8, 2021.